Numerical Simulation of Nitrous Oxide Catalytic Decomposition

Advisor: | Prof. Filippo Maggi
Co-Advisors: | Prof. Oskar J. Haidn
| Ing. Chiara Boffa

Thesis:
Locatelli Matteo
836585

October 3, 2017
A. Y. 2016 - 2017

Abstract

The thesis presents a model for the simulation of nitrous oxide (N_2O) catalytic decomposition, translating in a numerical environment some of the most important experimental outcomes about this process. N_2O has gained popularity in the space field during last decade thanks to its promising potential as hydrazine substitute.

Hydrazine (N_2H_4) is currently the most used monopropellant for attitude thrusters. Its dominance over other propellant solutions has been guaranteed by the creation and commercialization of the Shell S405 catalyst which is able to activate hydrazine decomposition reaction so as to maximize its propulsive performances. Hydrazine is anyway affected by some drawbacks: it has a very high toxicity and it needs a pressurization device in the storage system.

During last decade, management and transportation costs have increased steadily, together with the price of the bulk material due to its large request. Therefore, engineers have started looking around for possible alternatives.

Nitrous oxide is considered a good alternative to hydrazine: characterized by an exothermic decomposition, its very low level of toxicity and self-pressurization properties may help in reducing management costs for the propellant, with an additional simplification of the storage system connected with the lack of pressurization system needed.

Increasing effort has been spent to study and understand the decomposition phenomenon itself and to survey possible catalytic materials able to activate the reaction: goal for the near future is to discover an efficient, long-lasting and reusable catalyst. Only such an achievement can justify a widespread adoption of N_2O as monopropellant, similarly to what happened for hydrazine with the S405.

Inside this framework of active experimental studies about N_2O decomposition, the thesis presents a numerical study on the catalytic decomposition process of nitrous oxide. The simulator can help in understanding how different catalytic active phases affect the decomposition and their impact on propulsive performances.

In the present work, catalyst simulator is coupled with tank outflow and nozzle expansion simulators to present a complete blowdown process with no mass flow control.

Goal of the work is to simulate how catalyst perform with time-varying inlet conditions, to spot possible technological problems connected to N_2O usage and to give a preliminary sizing of the main components for an on-ground bench to test a catalytic decomposition.

Keywords: Nitrous oxide, catalytic decomposition, monopropellant thruster.

Sommario

La tesi presenta un modello utile a simulare il processo di decomposizione catalitica per ossido di diazoto (N_2O), traducendo in un ambiente numerico alcuni dei più importanti risultati sperimentali riguardanti tale processo. N_2O ha acquistato popolarità nell'ultimo decennio all'interno dell'industria spaziale grazie al suo riconosciuto potenziale come possibile sostituto dell'idrazina.

L'idrazina (N_2H_4) è attualmente il più usato monopropellente per sistemi di controllo d'assetto a razzo. Il suo attuale incontrastato dominio è dovuto alla creazione e commercializzazione del catalizzatore Shell S405 il quale è in grado di attivare la reazione di decomposizione dell'N_2H_4 massimizzandone le prestazioni propulsive. L'idrazina presenta tuttavia importanti svantaggi, rappresentati dal suo alto livello di tossicità e dallla necessità di un sistema di pressurizzazione all'interno del serbatoio. Nell'ultimo decennio, i costi di trattamento e trasporto per l'idrazina sono aumentati costantemente, insieme con il prezzo del materiale grezzo, a causa della crescente richiesta dall'industria spaziale. A conseguenza di ciò, gli ingegneri sono attualmente alla ricerca di possibili alternative.

N_2O è considerato una valida soluzione ai problemi dell'idrazina: anch'esso caratterizzato da una decomposizione esotermica, il suo basso livello di tossicità accoppiato con proprietà di auto pressurizzazione aiutano nella riduzione dei costi di trattamento del propellente, con una semplificazione addizionale nello schema del serbatoio.

Un impegno crescente viene speso per studiare e capire i principi fondamentali alla base del fenomeno di decomposizione stesso, investigando possibili materiali catalitici capaci di attivare la reazione: l'obiettivo per l'immediato futuro è di sintetizzare un catalizzatore efficiente, duraturo e riutilizzabile. Solo il raggiungimento di questo traguardo può giustificare l'adozione di N_2O come monopropellente, in maniera del tutto simile a quanto è accaduto all'idrazina con l'S405.

In questo contesto di intensa attività sperimentale riguardante la decomposizione di N_2O, la tesi presenta uno studio numerico sul processo di decomposizione catalitica di N_2O. Il simulatore viene utilizzato per comprendere come diverse fasi attive catalitiche influenzano la decomposizione e il loro impatto sulle prestazioni propulsive. Nel presente lavoro, il simulatore del catalizzatore è accoppiato con simulatori per l'efflusso da serbatoio e per l'espansione in ugello in modo da rappresentare un completo sistema di blowdown senza controllo di flusso di massa.

Obiettivo della tesi è di simulare come il catalizzatore viene influenzato da condizioni iniziali tempo dipendenti, di identificare possibili problematiche nell'applicazione tecnologica dell'N_2O e fornire un dimensionamento preliminare di un banco di prova per testare la decomposizione catalitica.

Contents

List of Figures

List of Tables

Nomenclature

Thermodynamics

a_{exit}	[m/s]	Sound Speed at Tank Exit Section
$c_{p_{N_2O}}$	[J/kgK]	Nitrous Oxide Specific Heat at Constant Pressure
$c_{p_{N_2}}$	[J/kgK]	Nitrogen Specific Heat at Constant Pressure
$c_{p_{O_2}}$	[J/kgK]	Oxygen Specific Heat at Constant Pressure
$c_{p_{N_2O}^{tank}}$	[J/kgK]	Tank Total Nitrous Oxide Specific Heat at Constant Pressure
$\Delta H_r^{N_2O}$	[J/mol]	Nitrous Oxide Enthalpy of Decomposition Reaction
F_{N_2O}	[mol/s]	Nitrous Oxide Molar Flow Rate
F_{N_2}	[mol/s]	Nitrogen Molar Flow Rate
F_{O_2}	[mol/s]	Oxygen Molar Flow Rate
γ_{N_2O}	[−]	Nitrous Oxide Specific Heat Ratio
γ_{N_2}	[−]	Nitrogen Specific Heat Ratio
γ_{O_2}	[−]	Oxygen Specific Heat Ratio
$\dot{m}$	[g/s]	Mass Flow Rate
m_{N_2O}	[g]	Nitrous Oxide Mass inside the Tank
M_{exit}	[−]	Mach Number
μ	[Pas]	Mixture Viscosity
μ_{N_2O}	[Pas]	Nitrous Oxide Mixture Viscosity
μN_2	[Pas]	Nitrogen Mixture Viscosity
μO_2	[Pas]	Oxygen Mixture Viscosity
p_{tank}	[bar]	Tank Total Nitrous Oxide Pressure
p_{exit}	[bar]	Nitrous Oxide Pressure at Tank Exit Section
p_{inj}	[bar]	Nitrous Oxide Pressure after Injector
p	[bar]	Pressure of Mixture in Catalyst
p_0	[bar]	Nitrous Oxide Inlet Pressure in Catalyst
p_{end}	[bar]	Pressure of Mixture at End of Catalyst

p_d	[bar]	Discharge Pressure at Nozzle Exit Section
p_s	[bar]	Nitrous Oxide Pressure value at Constant Entropy
p_u	[bar]	Nitrous Oxide Pressure value at Constant Internal Energy
p_h	[bar]	Nitrous Oxide Pressure value at Constant Enthalpy
ρ	[kg/m^3]	Mixture Density
$\rho_{N_2O}^{tank}$	[kg/m^3]	Nitrous Oxide Density inside the tank
ρ_{N_2O}	[kg/m^3]	Nitrous Oxide Density
ρ_{N_2}	[kg/m^3]	Nitrogen Density
ρ_{O_2}	[kg/m^3]	Oxygen Density
T_{tank}	[K]	Tank Total Nitrous Oxide Temperature
T_{exit}	[K]	Nitrous Oxide Temperature at Tank Exit Section
T_{inj}	[K]	Nitrous Oxide Temperature after Injector
T	[K]	Temperature of Mixture in Catalyst
T_0	[K]	Nitrous Oxide Inlet Temperature in Catalyst
T_{end}	[K]	Temperature of Mixture at End of Catalyst
T_d	[K]	Discharge Temperature at Nozzle Exit Section
T_s	[K]	Nitrous Oxide Temperature value at Constant Entropy
T_u	[K]	Nitrous Oxide Temperature value at Constant Internal Energy
T_h	[K]	Nitrous Oxide Temperature value at Constant Enthalpy
V_{tank}	[m^3]	Tank Volume
v_d	[m/s]	Discharge Velocity at Tank Exit Section
Y	[$-$]	Injector Compressibility Factor
y_{N_2O}	[$-$]	Nitrous Oxide Molar Fraction
y_{N_2}	[$-$]	Nitrogen Molar Fraction
y_{O_2}	[$-$]	Oxygen Molar Fraction
w_s	[m/s]	Superficial Velocity

Geometry & Materials

A_{inj}	[m^2]	Total Injection Area
A_{bed}	[m^2]	Catalyst Bed Cross Section
C_d	[$-$]	Injector Discharge Coefficient
D_{ratio}	[$-$]	Injector Diameter Ratio
d_{hole}	[m]	Injector Hole Diameter
d_{bed}	[m]	Catalyst Bed Diameter
d_p	[m]	Pellet Diameter
d_r	[$-$]	Catalyst to Pellet Diameter Ratio

ϵ	[−]	Void Fraction
p_{design}^{tank}	[bar]	Tank Pressure for Tank Sizing
p_{design}^{cat}	[bar]	Catalyst Pressure for Catalyst Sizing
σ_h	[MPa]	Hoop Stress
σ_l	[MPa]	Longitudinal Stress
σ_y^{Al}	[MPa]	Aluminum Yielding Stress
σ_y^{hx}	[MPa]	Hastelloy X Yielding Stress
r_{tank}	[m]	Tank radius
th_{tank}	[m]	Tank thickness
th_{hx}	[m]	Hastelloy X layer thickness

Chemistry & Heat Transfer

A_c	[mol/Pa$_{N_2O}$cm^{3}s]	Catalytic Pre-Exponential Constant
A_t	[1/s]	Thermal Pre-Exponential Constant
E_{a_c}	[J/mol]	Catalytic Activation Energy
E_{a_t}	[J/mol]	Thermal Activation Energy
r	[mol/cm^{3}s]	Overall Reaction Rate
r_c	[mol/cm^{3}s]	Catalytic Reaction Rate
r_t	[mol/cm^{3}s]	Thermal Reaction Rate
U	[W/m^{2}K]	Overall Heat Transfer Coefficient

A Mamma e Papà

Chapter 1

Introduction to the Thesis

Space propulsion system for a satellite shall answer two precise demands: provide space access capability to the spacecraft by injecting it into the desired orbit and control its attitude during the mission.
While bi-propellant rockets, solid rocket motors and hybrid propulsive units answer the first demand, on-orbit control of the spacecraft is provided by cold gas, monopropellant or electric thrusters.

1.1 Monopropellant Thruster

The thesis focuses on a specific category of thruster for attitude control, namely **monopropellant thrusters**: conjugating a moderate specific impulse ($\approx 200\ s$) with compactness, reusability and durability, a monopropellant thruster is a valid alternative to the poor-performing cold gas thrusters (specific impulse in around $50\ s$) and to the low-thrust power consuming electric thrusters.
Depending on the thruster class selected ranging from 0.1 to $400\,\mathrm{N}$ thrust, monopropellant thrusters can perform trajectory adjustment maneuver (out of reach for a typical electric thruster with thrusts in the order of μN - mN) as well as fine and repeated attitude control maneuver. [1]
A monopropellant system exploits an exothermic decomposition of a particular compound to produce high-pressure enthalpy-sensitive mixture expanded in a nozzle, generating a thrust.
Generally such a decomposition is characterized by a high activation energy, which is the reason why the compound do not decompose in ambient condition (atmospheric pressure and 25°C): a catalyst is therefore employed to lower this threshold energy

level and accelerate the reaction.

Monopropellant Thruster Scheme

A general purpose scheme of a monopropellant rocket foresees a propellant blowdown through a series of components: [1]

– Tank.
   Monopropellant is here stored, commonly in liquid state. If its vapor pressure is not high enough, an external pressurization system is employed to drive propellant out of the tank.
   A pressurized fluid (typically N_2) can be employed to push the propellant out of the tank. The same task can be accomplished by a mechanical system, basically consisting in a compressed spring.
   Turbo-pumps are used only on larger systems and provides a mechanical pressurization of the propellant exiting the tank, reducing stresses on the tank structure which shall no more contain a pressurized fluid.

– Main valve.
   A main valve regulates the propellant flow during the blowdown. An on/off device is used on systems for which a constant thrust for defined time span is required to achieve specific goals (i.e attitude control with small thrusters), while a proportional-aperture device is used for precise maneuver, in which both firing time and thrust magnitude are important to meet specific requirements (i.e. precise orbit correction maneuver).

– Injector.
   Injector shall distribute uniformly the propellant all over the catalytic bed and, specifically for a liquid propellant, shall guarantee its atomization and subsequent evaporation and mixing for an efficient decomposition.

– Catalyst.
   Catalyst is the most important part of the assembly. It consists typically in a hollow cylinder, made with high-temperature resistant materials, filled with pellets of different shapes (spheres, cylinder, more complex geometries) or with a monolithic metallic foam.
   Pellets and foam build the support for the so called "active phase", typically a precious metal among Pd, Pt, Rh, Ru, Ir, Au or Ag, dispersed on it.
   It is important that the support has a large surface area in order to maximize

number of active reactive spots.

Supports are chosen according to their surface area (external surface per cubic meter of material): the higher, the more active spots are present and, as a consequence, the more reactive the catalyst is.

Propellant decomposition is catalyzed thanks to the active phase particle, which actually gives an alternative (catalytic) decomposition path accessible with a lower activation energy.

Catalyst is usually the most expensive component inside a monopropellant, mainly due to the rarity of metals used as active phase, their deposition procedure onto the support and high-temperature materials used for the case.

Catalyst can be either found on the market or built by the user. In research activities, if a catalyst with precise specification shall be tested, it is very likely to be built by the user. On the other hand, a commercial monopropellant thruster purchased and installed directly on the spacecraft has its own catalyst integrated within the assembly.

This is typical for hydrazine monopropellant adopting the Shell S405 catalyst, as explained in the following.

– <u>Nozzle</u>.
Convergent-divergent nozzle discharges the mixture coming out from the catalyst in order to develop a thrust.

1.1.1 Hydrazine N_2H_4

Space industry relies entirely on hydrazine as monopropellant for attitude thruster applications.

AIRBUS, Defense and Space, has developed a complete family of hydrazine monopropellant thruster, ranging from $0.5\,N$ up to $400\,N$. They are used for attitude, trajectory and orbit control for different classes of space vehicles: small and mid-size satellites ($0.5\,N$), launchers (Ariane V attitude control relies on a $400\,N$ version of the thruster) or on the ESA Atmospheric Re-Entry Demonstrator (ARD). [2]

Moog-ISP has its own brand of hydrazine monopropellant, with thrust ranging from $1\,N$ to $445\,N$, suited for spacecraft attitude control applications. [3]

Aerojet RocketDyne has pushed itself into the flying monopropellant rocket market with a 40-year-long research and development work aimed at the design of a very large class of thruster able to develop up to $3.1\,kN$. [4]

On the other hand, Northrop Grumman focused on a restricted class of thruster for satellite attitude and velocity control. [5]

Attitude and orbit control demands precise performances for the thruster: large cycles number, burn duration and possibility of cold restarts.

Table 1.1 reports the most important characteristics of hydrazine thrusters available on the market.

Thruster Class	1 N	10 N	40 N
Estimated Cycles Life	300000	90000	4000
Single Burn Duration	12 h	10.5 h	450 s
Number of Cold Restarts	50	36	20
Catalyst Pressure	23 bar	15 bar	15 bar
Mass Flow Rate	0.45 g/s	12 g/s	23 g/s

Table 1.1: Hydrazine Monopropellant Characteristics

Properties

Hydrazine is a clear colorless fluid, liquid at ambient temperature and pressure (25°C, 1 bar), intrinsically unstable towards decomposition. A summary of the most important properties of hydrazine is reported in Table 1.2.

Some comments can be made about those properties.

Freezing temperature is high for space flight application, hydrazine tanks shall be insulated to prevent freezing of liquid hydrazine stored.

On the other hand, vapor pressure is pretty low. Typically, hydrazine monopropellant thrusters employ pressurization mechanisms (pressurizing gas separated with a diaphragm from the propellant or a mechanic systems are employed [1]).

Decomposition

Hydrazine decomposition is globally exothermic and its thermal dissociation can be triggered at a consistent rate upon heating up to a temperature of 260 °C.

Its decomposition occurs with a two-step process: [6, 7]

– <u>Step 1</u>.

$$3\,N_2H_4 \longrightarrow 4\,NH_3 + N_2 \qquad \Delta H_r = -152\,\frac{\text{kJ}}{\text{mol}} \tag{1.1}$$

Molecular Weight	32.05 g/mol
Density	$1.01\,\mathrm{g/m^3}$
Vapor Pressure at 30°C	1.3 kPa
Freezing Temperature	2 °C
Boiling Temperature	114 °C
Specific Heat at Constant Pressure	3.1 kJ/kgK

Table 1.2: Hydrazine Properties

This is the basic hydrazine decomposition reaction.
Usually it is initiated over a catalytic surface, without pre-heating to 260 °C, and completed thermally downstream the catalyst, with an overlapping ammonia catalytic decomposition downstream the catalyst. [8]

– Step 2.

$$4\,NH_3 \longrightarrow 2\,N_2 + 6\,H_2 \qquad \Delta H_r = 83\,\frac{\mathrm{kJ}}{\mathrm{mol}} \tag{1.2}$$

Ammonia dissociation, the second step of the reaction, is slower than the first one. It is endothermic and not always completed: amount of ammonia exiting the catalyst can be controlled by varying the catalyst length and will greatly affects the performance of the overall thruster.
Decomposition of ammonia actually absorbs useful enthalpy from the mixture: temperature profile therefore has a maximum along the catalyst. [6]
Defining the H_2 selectivity of the catalyst as:

$$X = \frac{2H_2}{2H_2 + 3NH_3} \cdot 100 \tag{1.3}$$

the extent of ammonia decomposition can be evaluated and the decomposition reaction rewritten as: [9]

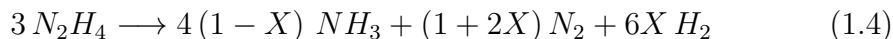$$3\,N_2H_4 \longrightarrow 4\,(1-X)\,NH_3 + (1+2X)\,N_2 + 6X\,H_2 \tag{1.4}$$

Table 1.3 shows how ammonia decomposition affects the temperature reached by the mixture at the end of the catalyst.

From NASA CEA simulation, adiabatic decomposition temperature for liquid N_2H_4 is 866 K, consistent with the situation for which N_2H_4 and NH_3 are completely decomposed. This is testified also by the computation performed in [10] whose results are reported in Table 1.3: for $X = 1$ decomposition temperature is 863 K.

X [−]	0	0.2	0.4	0.6	0.8	1
T_{ad} [K]	1659	1500	1343	1182	1023	863

Table 1.3: N_2H_4 Decomposition Temperature vs. Fraction of Dissociated NH_3

Catalyst plays a fundamental role from the point of view of propulsive performances for a hydrazine monopropellant: catalytic bed shall be sized accordingly to stop NH_3 consumption, thus preventing a temperature decrement which would be detrimental for propulsive efficiency.

Computing specific impulse for a hydrazine thruster with specification similar to the real thruster found on the market (and reported in Table 1.4), a value of 230 s is obtained which is completely in accordance with the performance available for those rockets: this results corresponds to a degree of NH_3 consumption equal to $X = 0.5$, with a decomposition temperature of about 1200 K, according with evidence from [10].

Indeed, if a pure mixture of nitrogen and hydrogen (with ammonia completely dissociated, $X = 1$) is expanded with the adiabatic decomposition temperature of 866 K found, the specific impulse value shrinks to 185 s.

Another important effect shall be taken into account: evaporation of liquid hydrazine prior decomposition.

If decomposition temperature for liquid hydrazine is 863 K, gaseous hydrazine shows an increase up to 1339 K (from NASA CEA simulation).

The counter-balancing trend between NH_3 dissociation and specific impulse can be mitigated with the usage of a very performant injector: if liquid N_2H_4 is atomized prior entering the catalyst (favoring evaporation), enthalpy removed from the mixture during evaporation is greatly reduced.

This translates in the possibility to employ a longer catalyst with an atomizer: despite the larger ammonia consumption, the reduced evaporation enthalpy prevents temperature decrements and favors propulsive performances.

$T = 40\,\mathrm{N}$, $P_{cc} = 15\,\mathrm{bar}$, $\epsilon = 60$, $c_T = 1.5$	
Adiabatic Decomposition Temperature T_{ad}	1200 K
Fraction of Decomposed Ammonia X	0.5
Specific Impulse I_{sp}	230 s

Table 1.4: Propulsive Properties Prediction for Hydrazine

Catalyst for Decomposition: Shell S405

Early developments in catalytic decomposition of hydrazine produced only catalyst active at relatively high temperature.
Beginning from 1962, Shell Development Company, sponsored by NASA, started the development of a new brand of catalysts. [11]
The outcome of their work was the Shell S405 which paved the way for a widespread usage of hydrazine as the most convenient monopropellant.
S405 could meet performance and reusability requirements never achieved before by the technology of the time: built to be capable of at least 10 starts with 180 seconds duration, the S405 exceeded expectations being reusable thousands of times for hours, at favorable performances. [11]

Differently from conventional catalyst, with an active metal loading of about $0.5 \div 5\,\mathrm{wt\%}$, mostly employed for reaction temperature reduction at $700\,°C$, S405 had been designed to work at the uppermost working temperature, with an extremely high metal loading: $31 \div 33\,\mathrm{wt\%}$ iridium is loaded on the support.
With this particular set of characteristics, the S405 is really active for hydrazine decomposition, with a reaction time in the order of milliseconds at bed temperature as low as $0\,°C$. [12]

Main Problematics with Hydrazine

Hydrazine has a very high level of toxicity, the highest among other hypergolic mono- or cold gas propellants [13], with the highest quantity-distance requirements and the most stringent accidental release measures: as a result, on-ground treatment is nowadays the real hydrazine shortcoming, both in terms of treatment time and operational cost. [13]

Over the last 30 years, hydrazine, despite showing one of the most favorable properties set among other hypergolic propellants in terms of storability and propulsive performance, has seen its handling and usage costs increasing steadily. [14]
Even cost for bulk hydrazine, due to its widespread use, is increased during the last decade. [15]

For what concerns storage and transportation, hydrazine is not shock sensitive but a mixture of air and hydrazine vapor could be extremely flammable, so a hydrazine tank should be carefully isolated from air.
Moreover, as previously explained, hydrazine has a quite high freezing point, around $2\,°C$. Even if for most applications this threshold is acceptable, some military applications would requires an additional safety margin. [6]
Lastly a hydrazine monopropellant cannot avoid the complication, and additional weights, of a tank pressurization system, since its vapor pressure is really low.

1.1.2   Hydrogen Peroxide H_2O_2

Hydrogen peroxide H_2O_2 has always been an attractive monopropellant candidate.
In 1930 German V-2 rocket employed for the first time hydrogen peroxide as monopropellant, with a packed bed catalyst.
In post-war actitivities, US X-1 and X-15 space planes, together with the early Mercury and Gemini manned spacecrafts, used hydrogen peroxide-based attitude control systems.
A significant amount of work has been carried out in the 1960s at NASA laboratories on hydrogen peroxide decomposition and its application to monopropellant rockets, but the idea of hydrogen peroxide was abandoned with the commercialization of very effective hydrazine catalysts.
Hydrogen peroxide have been extensively used in the Soyuz launch vehicles to drive the gas generator turbine pump and in the descent phase thruster control systems. [16]
In 1997 Whitehead managed to built a $25\,\mathrm{kg}$ H_2O_2 monopropellant rocket that successfully flew discharging $3.5\,\mathrm{kg}$ of hydrogen peroxide. [17]
Two years later, Werminont and Mullens presented a class of thruster, from 3 to $25\,\mathrm{lb_f}$ of thrust, on behalf of General Kinetics. [18]
Recently, following the trend of green engineering, the Italian Alta S.p.A and the english DELTACAT Ltd. are cooperating, in the framework of LET-SME ESA-founded project, on the development of a new class of H_2O_2 thruster implementing a brand new catalyst technology. [16]

Properties and Decomposition

Hydrogen peroxide is a colorless liquid, slightly more viscous than water.
From home-related products up to the rocketry application, H_2O_2 is mixed with water: a H_2O_2 monopropellant typically presents hydrogen peroxide concentration higher than 80 %. Table 1.5 reports some of the most important properties of pure

Molecular Weight	34.01 g/mol
Density	1.45 g/m^3
Vapor Pressure at 30°C	0.6 kPa
Freezing Temperature	0 °C
Boiling Temperature	150 °C
Specific Heat at Constant Pressure	2.6 kJ/kgK

Table 1.5: Hydrogen Peroxide Properties

H_2O_2. As for hydrazine, a high freezing temperature, around $-0.4\,°C$, poses some treats from the storage point of view while a high evaporation temperature do not represent a concern for H_2O_2 applications.
Very low vapor pressure translates in the need of an external pressurization system, while high density for the liquid phase is a very interesting property from the storage point of view.

Decomposition reaction for hydrogen peroxide is exothermic and can be represented with:
$$2H_2O_{2(l)} \longrightarrow 2H_2O_{(g)} + O_{2(g)} \quad \Delta H_r = -187.8\,\frac{\text{kJ}}{\text{mol}} \tag{1.5}$$

CEA simulations define an adiabatic decomposition temperature for liquid H_2O_2 equal to 1274 K. Using a test thruster with the same specification (reported in Table 1.6) previously used for the hydrazine performance prediction, a specific impulse value of 163 s is obtained.

Main Problematics with Hydrogen Peroxide

Despite not having the carcinogen effects of its hydrazine counterpart, hydrogen peroxide should anyway treated carefully: a H_2O_2 water solution at 30% concentration

$T = 40\,\mathrm{N}$, $P_{cc} = 15\,\mathrm{bar}$, $\epsilon = 60$, $c_T = 1.5$	
Adiabatic Decomposition Temperature T_{ad}	$1274\,\mathrm{K}$
Specific Impulse I_{sp}	$163\,\mathrm{s}$

Table 1.6: Propulsive Properties Prediction for Hydrogen Peroxide

can burn human skin, and its vapors can damage lungs if inhaled. Despite all, protective clothes are needed only in case of repeated exposure or for in-tank activity. [19]
Hydrogen peroxide is thermodynamically unstable: an excessive prolonged heating results in decomposition of the peroxide, leading to further heating of the liquid and a cascade effect. Especially at higher concentrations this can lead to runaway reactions. But even in this case, detonations do not occur in the liquid phase, while they may occur in vapor phase.
Directly connected with its instability, storability may be problematic since even a low level of contamination would result in gradual, unstoppable decomposition: hydrogen peroxide concentration will inexorably decrease over time, making it unsuitable for long space missions.
H_2O_2 seems also to lack of hypergolicity when matched with other fuels/oxidizer: no other substance can oxidize or can be oxidized by hydrogen peroxide, limiting its windows of application in the space domain. [20]

The real drawback with H_2O_2 is the lack of a reliable and reusable catalyst for its decomposition, preventing it from being extensively used. [16] A catalyst for H_2O_2 decomposition hardly reach more than 58000 s of duty time. [20]
The state of the art catalyst for hydrogen peroxide decomposition is made of metallic silver, permanganates of alkali metals and manganese oxides like MnO_2 or Mn_2O_3. Anyway, a pre-heating for the incoming H_2O_2 is required to activate decomposition at a sustainable rate. [16]

1.1.3 Nitrous Oxide

Nitrous oxide discovery as a potential monopropellant is quite recent: self-sustaining catalytic decomposition was firstly reported by Timothy J. Lawrence in 1998. [21]
From the first self-sustained decomposition, research has pushed towards the improvement of catalyst technology for the decomposition of N_2O.

Later in 1998 a Mark-III resisto-jet exploited a self-sustained nitrous oxide decomposition for more than 18 hours during a vacuum test at the US Air Force Research Lab at EDWARDS Air Force Base, CA.

The highest recorded specific impulse from that experiment was 148 s. In 1999 the first nitrous oxide resistojet thruster (0.1 N thrust), Mark-IV, has been successfully commissioned on board the UoSAT-12 mini-satellite. [21]

Important experiments have been carried out at University of Surrey in 2001, England, along with Tsinghua University, between 2004 and 2008 shedding lights on catalytic decomposition of nitrous oxide. Deeper knowledge has been acquired about how the process is influenced by the N_2O inlet mass flow rate and how it can be accelerated increasing the preheating energy supply. [21]

Later in 2009, at Stanford University, researches focused on how the performance of a thruster could be influenced by the design of the catalyst, surveying as well the possibility of initiating the reaction via mixing with methane CH_4. [22]

In 2011 researchers at Beihang University studied the possibility to optimize the design of the catalyst avoiding any heat dispersion and, as a result, maximizing the performance of the overall thruster. [23]

Properties

Nitrous oxide N_2O is a linear asymmetric triatomic molecule firstly discovered and prepared in 1793, by the english Joseph Priestley. Priestley achieved nitrous oxide synthesis by heating ammonium nitrate crystals to produce a macroscopically colorless, non-flammable, non-toxic gas at ambient condition with a relatively sweet taste and odor.

Table 1.7 presents meaningful properties for nitrous oxide, which presents a peculiar properties spectrum if compared with hydrazine and hydrogen peroxide.

At ambient pressure (1 bar), freezing and boiling temperature are practically the same: nitrous oxide is a gas even at very low temperature.

At ambient temperature (25°C), saturation pressure is reached at 56.5 bar: in this conditions liquid N_2O is produced with a density of 0.74 g/cm³, lower than hydrazine and hydrogen peroxide. But at lower temperature, saturation limit lowers and liquid density increases, as shown in Table 1.7.

Such a high vapor pressure lead to a very important consequence: no external pressurization system is needed to drive liquid N_2O out of the tank, N_2O vapor at such high pressure fulfill this task.

Molecular Weight	44.01 g/mol
Liquid Density at 298.15K	0.74 g/m^3
Liquid Density at 273.15K	0.91 g/m^3
Vapor Pressure at 25°C	5650 kPa
Freezing Temperature	-91.1 °C
Boiling Temperature	-88.5 °C
Specific Heat at Constant Pressure	3.91 kJ/kgK

Table 1.7: Nitrous Oxide Properties

Decomposition

Being quite stable and non-reactive at ambient temperature and pressure, N_2O can decompose exothermically at an appreciable rate only above 800 °C following the reaction:

$$N_2O \longrightarrow N_2 + \frac{1}{2}O_2 \tag{1.6}$$

N_2O thermal decomposition is almost impossible to achieve without a catalyst: pre-heating temperature is reduced and reaction is accelerated.

Catalytic decomposition is achievable through different type of catalysts, including oxides, mixed oxides and zeolites. The latter in particular have been proven to guarantee high reactivity in nitrous oxide catalysis. [24]

N_2O has been also employed as oxidizer in hybrid rocket engines [25], thanks to its exothermic decomposition producing large amount of oxygen, suitable to lead a fuel to combustion.

A complete review of both catalytic and thermal decomposition for nitrous oxide will be given in Chapter 2.

Table 1.8 reports predicted theoretical performances with NASA CEA code.

Main Problematics with Nitrous Oxide

The main problem with nitrous oxide, as for hydrogen peroxide, is the development of a long-lasting and reliable catalyst.

Moreover, its elevated decomposition temperature, around 1900 K, poses real treats from the point of view of the material employed in the system.

$T = 40\,\text{N},\ P_{cc} = 15\,\text{bar},\ \epsilon = 60,\ c_T = 1.5$	
Adiabatic Decomposition Temperature T_{ad}	1907 K
Specific Impulse I_{sp}	170 s

Table 1.8: Propulsive Properties Prediction for Nitrous Oxide

Nitrous oxide has a really low level of toxicity. Short term exposure can lead to dizziness or headache, no special equipment is required working at its direct contact. Neurotoxic effects occur only with exposure to high concentration (around 200000 ppm), while loss of consciousness may occur at concentration in around 800000 ppm. [19]

Even if is not dangerous when inhaled, nitrous oxide can be problematic due to asphyxiation hazard for possible gathering at lower levels, since it is 1.5 times heavier than air.

Nowadays, nitrous oxide is not on the list of ozone depletion substances, quoting the US Environmental Protection Agency. [26]

At about 100 km, N_2O is likely to be ionized rather than remain stable and, therefore, it is very difficult that it can reach stratosphere, at around 40 km, where ozone depletion actually occur.

But it is potentially a big contributor to greenhouse effect, since the impact of 1 kg of nitrous oxide corresponds to 300 time the impact of 1 kg carbon dioxide. [26]

CO_2 remains the biggest contributor to the greenhouse effects: mass of emitted carbon dioxide in atmosphere has been estimated in 34.5 billion tons in 2013. In the same year, atmospheric emission of N_2O has contributed to the greenhouse effect for an equivalent amount of 3.3 billion tons. [27]

1.1.4   Ionic Solids: ADN and HAN

Starting from the beginning of 2000s, the US Department of Defense and the Swedish Corporation cooperate within the ECological Advanced Propulsion Systems (ECAPS), for the development and production of a highly energetic, unstable and potentially explosive brand of salts which, for safety reasons, are diluted in ionic liquid solution of water with strong ion-to-ion interactions and potentially usable as monopropellants. [28]

The two most promising compounds are:

– Ammonium Dinitramide ADN

– Hydroxylamine Nitrate HAN

Basic properties for both are reported in Table 1.9.

	HAN	ADN
Molecular Weight	$96.0\,\text{g/mol}$	$124.0\,\text{g/mol}$
Density	$1.84\,\text{g/m}^3$	$1.81\,\text{g/m}^3$
Freezing Temperature	$48\,^{\circ}\text{C}$	$93\,^{\circ}\text{C}$

Table 1.9: HAN and ADN Properties

ADN - Ammonium Dinitramide

Currently, ADN is manufactured by EURENCO Bofors, Karlskoga, Sweden and Alexandria VA, USA as a liquid blend high-performance propellant, and commercialized under the name of LMP-103S.
It decomposes catalytically and exothermically producing water vapor.
This new propellant have been tested during a year-long in-space test regarding a $1\,N$ thruster, implemented on the Prisma spacecraft platform. [29]
Outcome from this series of experiments are encouraging, with a reported mean in-space specific impulse of about $220\,s$ and an inferior toxicity level with respect to hydrazine, even if is marked as an explosive due to presence of methanol.
Moreover, a test has shown that ADN results compatible with materials usually used for hydrazine. [29]

HAN - Hydroxylamine Nitrate

For what concerns HAN, the Naval Ordinance Station, Indian Head, MD developed a number of HAN-based liquid monopropellants to be used in artillery guns for the US Army.
Aerojet Corporation of Redmond Washington conducted alternative development of HAN monopropellant where the fuel components of one of the HAN formulations developed by the NOS, named LP1846, have been substituted with glycine.
This formulation emphasized compatibility with existing hydrazine catalyst, with a catalytic temperature of $1100\,^{\circ}C$, similarly to hydrazine but with higher molecular mass: specific impulse is therefore lower, around $190\,s$.

1.2 Problem Identification & Thesis Goals

Space industry nowadays relies entirely on hydrazine as monopropellant when dealing with attitude thrusters applications.
As previously explained, Shell S405 catalyst is long-lasting and efficient catalyst for hydrazine decomposition, with a background of successful past missions that has consolidated its dominance over monopropellant market.

Problem Identification

Some problems must be managed if hydrazine is used on-board a spacecraft:

– On-ground activity are really long, complex and dangerous due to hydrazine high level of toxicity [13], which actually translates on a big burden on mission budget.

– Hydrazine is not only harmful for humans but also for the environment [13]. It is important to consider in the mission budget the transportation additional costs and the one related with contingency maneuvers aimed at mitigating launcher failure with consequent dispersion of hydrazine in the environment. [30]

– Hydrazine is liquid at ambient condition but with a very low vapor pressure which makes a pressurization system necessary. [1]

– Not only is hydrazine costly to be managed, the increasing request for hydrazine in space-related applications during last decade has increased costs for bulk hydrazine. [15]

As a consequence, space industry in the last decade has surveyed several monopropellant alternatives to be considered as suitable to replace hydrazine in the near future. They should couple a lower toxicity level (and therefore lower management cost) with reasonable performances.
Since the main characteristic of these alternative monopropellants is to be less harmful than hydrazine, they are named "green propellants".

"Green Propellants"

Hydrogen peroxide is the first real alternative to hydrazine, since its application as monopropellant has been extensively studied from the 50s. Despite showing a

lower toxicity level is not completely harmless, especially at the higher concentration (above 80%) needed for propulsive application [20].

The missed development of a reliable, re-usable and efficient catalyst has downplayed its perspective in the propulsion field. Moreover vapor pressure is comparable to hydrazine one, a pressurization system is anyway required and the predicted propulsive performances are not so remarkable, with respect to hydrazine, as shown in Section 1.1.2.

HAN and ADN are out of the "green propellant" domain. They are not easily accessible and nonetheless easily treatable: they have been discovered in military context and they are known to be extremely unstable, dangerous and toxic. [29] Nitrous oxide instead gives more consistent advantages with respect to hydrogen peroxide:

– It is harmless to humans (very little safety requirements shall be followed, as presented in Section 1.1.3),

– Its predicted propulsive performances are acceptable ($I_{sp} = 170\,\text{s}$), higher than hydrogen peroxide but not comparable with hydrazine.

– Its very high vapor pressure makes N_2O a self pressurizing propellant.

In addition to this, nitrous oxide discovery as a possible "green propellant" is recent, leaving large room for improvements: catalytic decomposition is a new topic of research. Several experimental works have been carried out studying N_2O decomposition in the last decade ([31], [21], [22], [23], [25]). The goal is now to deeply understand the decomposition in order to select the best catalyst among the ones now available (two solutions are presented in Chapter 2).

Ultimately the desire is to design a long-lasting, reliable and efficient catalyst that can pave the way to nitrous oxide adoption in the space propulsion field (as the S405 for hydrazine). Some point of concern with nitrous oxide are still present. The most important two are listed hereafter:

1. Transportation and storage for nitrous oxide shall be handled with care. Merrill, in [32], reports a series of incident in transportation and storage over the recent years (up to 2008). Despite being recognized as non-toxic, safety hazard shall be studied and understood more in details.

2. Large vapor pressure at ambient temperature translates in the fact that nitrous oxide is gaseous in ambient condition.
   Loading a tank with gaseous nitrous oxide up to a sufficiently high pressure level (56.5 bar at 25°C) is the only way to producing liquid N_2O whose density

is anyway smaller than hydrazine one $(0.74\,\mathrm{g/cm^3})$.
Performing the same operation at 0°C leads to a condensed N_2O phase with density to comparable to hydrazine one, as reported in Section 1.1.3.

3. Predicted theoretical decomposition temperature is beyond the resistance limit of the state-of-the-art high-temperature metallic alloy.
   Particular care has to be undertaken in facing this problem.

Thesis Localization in the Literature

In this scenario of active experimental research on N_2O decomposition, the thesis analyze the catalytic decomposition phenomenon from a numerical point of view: indeed core of the work is the numerical simulation of N_2O catalytic decomposition event.
Simulating in a numeric environment the process of catalytic decomposition can answer several needs:

– Newly discovered materials, active in N_2O decomposition, can be tested right-away in a numerical simulator. Their impact on the decomposition event can be assessed numerically prior than experimentally.

– Several possible catalyst structures and geometries may be investigated at once, defining which is the impact on the decomposition.

– Criticalities in the design may be spotted avoiding costly failure in the experimental activity. Zakirov in [31] reports cases of experiments aborted due to structural failure of the catalyst case induced by the high decomposition temperature, which he motivates with lack of theoretical knowledge about N_2O decomposition event.

The selected model of the catalyst, presented in Chapter 3, has been employ by Makled et al. in [8] to simulate numerically hydrazine decomposition inside a catalyst, obtaining good agreement with experimental results.
In the framework of this thesis, only **gaseous nitrous oxide** is considered.
This is explicable with two important considerations:

– N_2O catalytic decomposition is to be fully understood yet, therefore simulating or testing a two-phase phenomenon increases greatly its complexity. (Koopmans in [20] acknowledge the two-phase nature of H_2O_2 decomposition as one of the biggest drawback in the simulation of the phenomenon)

– Due to its high saturation pressure, the pressure loss induced by the injection in the catalyst leads nitrous oxide to complete evaporation. (Newlands gives experimental evidence of N_2O complete evaporation upon injection in [33])

Goal of the Work

Main goal of the thesis is to simulate the N_2O catalytic decomposition event with a reactor model known for its high fidelity [34] and adherence to experimental results (Makled in [8]), which is presented in Chapter 3. Results of the simulations are critically analyzed with respect to the theoretical notions presented in Chapter 1, 2, 3 and with the experimental evidences collected from literature.

Open points are identified from the aforementioned post-process analysis of the results and demanded to further experimental activities. Indeed, this steady-state simulator can be validated with long-lasting steady-state experiments, typically performed to test catalyst durability and repeatability. Examples of such tests for nitrous oxide are given in [31], where a highly equipped experimental apparatus is employed to provide continuously propellant.

In the framework of this thesis, another branch of experimental activities is considered, dealing with a simpler test bench: an isolated tank loaded with gaseous nitrous oxide discharges, through a simple on/off valve, an injector and a pre-heating device, N_2O inside the catalyst. Additionally, a nozzle can be attached to the catalyst exit section in order to assess propulsive performances of the mixture. A scheme of the experimental apparatus is given in Figure 1.1.
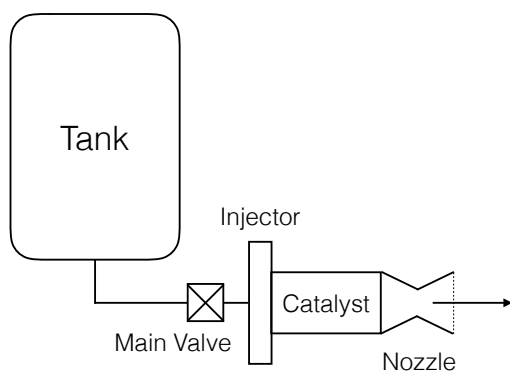

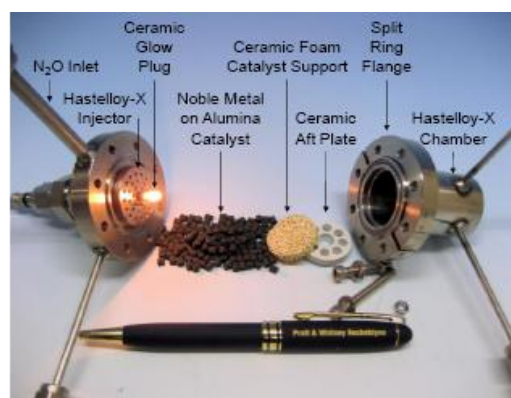
Figure 1.1: Test Bench Scheme

Figure 1.2: Experimental Test Bench

Example of such an experimental apparatus is given in [22] and shown in Figure 1.2 (Courtesy of Scherson et al., [22]).

Therefore, the catalyst simulator has been coupled with simulations of other components:

– Tank outflow dynamics for gaseous nitrous oxide (considered as a real gas expansion process).

– Injector head losses.

– Nozzle expansion for the $N_2 + O_2$ mixture (considered as an ideal gas) exiting the catalyst.

Some components have not been considered in the analysis:

– Main valve.
  Being a simple on-off design, its head loss has been considered negligible.

– Pre-heating device.
  As it will be clear in Chapter 3 and 4, N_2O injected in the catalyst shall be heated up to a low-limit threshold temperature in order to activate decomposition reaction. Thermic simulation fo this kind of component is beyond the scope of the work: there is experimental evidence ([25], [31]) that such kind of device can be built or purchased and its recorded performance are well within the requests of the assembly presented in this thesis.

Several are the objective in simulating an overall behavior of such a test bench:

1. Catalyst, a steady-state model of decomposition, can be coupled with a time-varying outflow simulation of the tank.
   It is therefore possible to see how decomposition profile changes with variation of initial conditions.

2. Results of the numerical simulations are used to highlight some problems in the design and helps in understanding a possible solutions. In this thesis, the design of the tank and selection of the insulation strategy for the catalyst (Chapter 3) are clear example of how numerical results can help understanding engineering problems.

3. Nozzle expansion is helpful in understanding propulsive performance of the decomposing mixture. A comparison with available propulsive performances available from the literature is therefore possible.

1.3 Thesis Structure

The thesis is articulated into six chapters.

This current first chapter deals with a general overview about monopropellant thrusters, hydrazine and possible "green" alternatives. Motivations driving the thesis and its goals are therefore explained.

Chapter 2 presents a treatment of the most important topics of the thesis. This chapter aims at giving a common-base knowledge on peculiar topics recalled during the presentation of the work. A review of the state-of-the-art research activities, regarding both catalyst for N_2O decomposition and homogeneous N_2O decomposition, has been performed to identify chemical kinetic parameters. The process followed to create databases for thermodynamic properties is explained together with some theoretical insight on N_2O decomposition reaction.

In Chapter 3 the models for tank, injector, catalyst and nozzle are presented. Starting from a brief description of the real system, a physical model is derived highlighting the most important assumptions which schematize the reality of the system. A mathematical model based on these assumptions is therefore derived.

Simulations for tank outflow dynamics, catalytic decomposition and nozzle expansions are reported and commented in Chapter 4. Each component of the assembly is tested separately with particular boundary conditions. Simulation of the overall dynamic of the assembly is reported as well and critically analyzed.

Some peculiar aspects, arisen comparing the presented results with the literature reviews, are commented in Chapter 5 in order to have a global overview of the work. Chapter 6 drives to the conclusion of the thesis. Important results achieved with the simulations are remarked together with possible future development of the work.

Chapter 2

State of the Art

In the following Chapter references for chemical kinetics and catalytic decomposition are given to introduce a literature review of the state-of-the-art experimental studies on N_2O decomposition.

Particularly, both thermal and catalytic nitrous oxide reaction steps will be presented, quoting the latest and most important experimental activity regarding them. The most active catalysts found in the literature will be investigated and, for both reactions, Arrhenius kinetic parameters are presented.

The effects of boundary conditions (initial temperature and pressure) on nitrous oxide decomposition temperature are analyzed, through simulations with NASA CEA, and presented.

Finally the data gathering process for N_2O, N_2 and O_2 thermodynamic properties is illustrated.

2.1 References of Chemical Kinetics

Analyzing a generic reaction: [35]

$$A + B \longrightarrow C + D \tag{2.1}$$

for which the backward path can be neglected, its reaction rate depends only on the concentrations of the reactants, such as:

$$r = \frac{d\,[A]}{dt} = k \cdot [A]^n\,[B]^m \tag{2.2}$$

this is called the **differential rate law** expressing variation in time of concentration of the reactant species, characterized by:

- – Rate constant: k

- – Concentrations: $[A]$, $[B]$

- – Reaction order: n, m

Order of a reaction has to be assessed experimentally according to the reaction mechanism involved.

2.1.1 Rate Constant

Reaction rate does not depend solely on reactants concentrations.
From empiric knowledge, it is clear that reaction rate increases with increasing temperature and pressure. Collision model has been developed to account for observed characteristics of reaction rates and it is centered on the basic idea that molecules must collide to react.
Collisions, unfortunately, are not the same effective in triggering a reaction process.

Svante Arrhenius in the 1880s theorized that, in order for a collision to be effective:

- – Energy coming out from the collision should overcome a threshold energy level called **activation energy**.
  When two molecules collide, the kinetic energy they possess is converted into potential energy due to molecules distortion during the collision, breaking bonds and rearranging their atoms into the product molecules.
  A weak collision may not induce bonds rupture, formation of products and so a reaction activation.

- – **Molecular orientation** is also fundamental for reaction activation.
  Even if a collision has the required amount of energy, direction along which molecules collide is also important so as to break up bonds correctly.

These two phenomena can be taken into account with three factors: **collision frequency** z, reflecting how frequently collisions happen, **steric factor** p $(0 < p < 1)$, reflecting the fraction of collisions with effective orientation, and **activation energy** E_a as the least amount of energy a collision has to deploy in order for molecules to

break their bonds.

Since temperature greatly influences this process because of thermal agitation, an exponential trend, $e^{-E_a/R_u T}$, is used to estimate this phenomenon.

The final expression for the rate constant is thus:

$$k = zp \cdot e^{-\frac{E_a}{R_u T}} \tag{2.3}$$

where the first two factors are usually grouped in the pre-exponential constant $A = zp$.

Arrhenius equation is, even nowadays, the best available rate constant estimate: pre-exponential A and activation energy E_a are the experimental constant to be drawn for reaction rate calculation:

$$k = A \cdot e^{-\frac{E_a}{R_u T}} \tag{2.4}$$

2.1.2 Zero Order Reaction

A zero order reaction does not show any dependence from reactant concentration. The rate law is then equal to the rate constant:

$$r = k \cdot [A]^0 = k \tag{2.5}$$

Integrating the rate law:

$$[A] = -kt + [A]_0 \tag{2.6}$$

reactant concentration is now linearly dependent on time and its plot is a straight line with slope $-k$. The **half-life** of a zero order reaction is:

$$\frac{[A]_0}{2} = -kt_{1/2} + [A]_0 \tag{2.7}$$

$$t_{1/2} = \frac{[A]_0}{2k} \tag{2.8}$$

2.1.3 First Order Reaction

Reaction rate depends linearly from reactant concentration, having an expression of the type:

$$r = k \cdot [A] \tag{2.9}$$

By integrating the first order rate law, some important consideration can be made:

$$\log [A] = -kt + \log [A]_0 \tag{2.10}$$

- Since concentration of A is time dependent, knowing k and the initial concentration $[A]_0$, concentration of A at any time can be computed.

- The integral first order rate law is linear in the variable $\log[A]$. Since reaction order has to be assessed experimentally, reaction can be easily recognized as a first order if plot of $\log[A]$ in time is a straight line.

- Expressing the integrated rate law as:

$$\log\left(\frac{[A]_0}{[A]}\right) = kt \tag{2.11}$$

the time needed for the reaction to halve reactant concentration, named half-life of the reaction $t_{1/2}$ is:

$$[A] = \frac{[A]_0}{2} \tag{2.12}$$

$$\log\left(\frac{[A]_0}{[A]_0/2}\right) = kt_{1/2} \tag{2.13}$$

and so:

$$\log 2 = kt_{1/2} \tag{2.14}$$

$$t_{1/2} = \frac{0.693}{k} \tag{2.15}$$

2.1.4 Second Order Reaction

For a second order reaction, the rate law is:

$$r = k \cdot [A]^2 \tag{2.16}$$

The integrated second order rate law is then:

$$\frac{1}{[A]} = kt + \frac{1}{[A]_0} \tag{2.17}$$

other important consideration can be made:

- A plot of the inverse of the reactant concentration in time produces a straight line, with slope equal to k.

- As for a first order reaction, knowing t and $[A]_0$, concentration at any time can be computed.

– Similarly as before, the half-life of the second order $t_{1/2}$ is:

$$\frac{1}{\frac{[A]_0}{2}} = kt + \frac{1}{[A]_0} \tag{2.18}$$

$$\frac{2}{\frac{[A]_0}{2}} - \frac{1}{[A]_0} = kt_{1/2} \tag{2.19}$$

and so:

$$t_{1/2} = \frac{1}{k\,[A]_0} \tag{2.20}$$

2.2 References of Catalytic Reactions

The path a reaction follows can be modified by the action of a so called catalyst.
A catalyst provides a modification of the actual sequence of elementary steps, setting off the reaction onto a different path: the lower the activation energy for the catalytic reaction, the higher is the catalyst efficiency and the faster the catalytic reaction will be with respect to the standard one. [36]

Catalyst of interest in this work are heterogeneous ones, with the catalytic reaction onsetting onto a solid surface.
A typical catalyst of this type, for monopropellant decomposition purposes, consists in pellets contained inside a cylindric case.
Pellets are mainly made up by two parts:

– Bulk material consist of high temperature resistant material with high surface area $(\approx 200\ \frac{m^2}{g})$ and with a geometry able to maximize their external exposed surface.
  This is called the catalyst **support**, and it is the actual massive element.

– An **active phase**, typically a metal dispersed on the support surface, which will be the catalytic reaction active site providing a low energy path. [36]

An entirely metallic pellet would be useless since just the metal or metal oxide layer present on its surface will be active.
Joining bulk inactive material with an active phase dispersed on its surface maximize catalyst effectiveness and minimize costs. [36]

2.2.1   Elementary Steps

Chemical reactions being catalyzed by an active phase on a solid surface foresee some important elementary steps: [36]

1. Reactant molecule has to be activated by **adsorption** on catalyst surface.
   This activation actually consist in the creation of a chemical bond between the active phase particle and the reactant molecule: the process involve just the surface site occupied by the metal particle.
   Two different kind of adsorption can occur:

   – Chemisorption: a strong chemical bond between reactant molecule and metal is formed and it is required for a proper activation: it is fundamental that activation energy for this reaction is lower than activation energy for the standard thermal chemical reaction, only in this way catalytic path can be undertaken.
   A big enthalpy change is required to form a strong connection with the catalyst surface which is said to be "specific", meaning that only one-to-one connection are possible and so a monolayer of activated reactant molecule can cover the surface of the catalyst.

   – Physisorption: weak interaction between reactant molecule and metal occurs, mainly due to Van der Waals forces. Since no strong molecular bond is formed, a multilayer configuration is feasible.
   Even though physisorbed molecules are not activated for catalysis, they may be precursors for chemisorption.

2. Adsorbed reactant molecules are now ready to follow an alternative catalytic path to complete its chemical reaction through a **surface reaction**.
   This step is different for each type of catalytic process: there can be an interaction between two identical activated adjacent sites for the formation of a particular product, the activated molecule can react with another non-activated reactant or two different activated reactants can form a particular product.

3. Final step consists in **desorption** of the product formed after the surface reaction.
   In such a way the catalytic process is completed and the active site is left free for another reactant molecule to be activated.

2.2.2 Factor Affecting Catalytic Performance

A heterogeneous catalytic reaction can be controlled and affected by different processes: [37]

– Velocity of N_2O adsorption on the catalyst, which is the speed of combination of an active phase molecule with N_2O on an active site.
This is a chemical kinetics limitation.

– Nitrous oxide has to pass into and out microscopic pores of the catalyst where the reaction occur.
Reaction can be limited by diffusion through pellet pores.

– A convective exchange takes place in the diffusive boundary layer around each pellet catalyst.
Reaction can be limited by convection, which is not able to carry products and reactants to the surface.

2.3 N_2O Decomposition State of the Art

2.3.1 N_2O Thermal Decomposition

Kalback, in his PhD thesis, differentiates thermal from catalytic N_2O decomposition reaction in a very clear way. [38]

Thermal decomposition is therefore presented in its elementary steps:

1. $N_2O + N_2O \longleftrightarrow N_2O^* + N_2O$: nitrous oxide molecule is activated by collision with another molecule, but it can be likewise deactivated.

2a. $N_2O^* \longrightarrow N_2 + O$

2b. $N_2O^* \longrightarrow NO + O$: early evidence showed that NO could have been just a transient intermediate product. Recent studies have confirmed that nitrogen monoxide can be among the product of the reaction.

Thus, the second elementary step foresees two different paths: it can either produce nitrogen and oxygen as products or the highly pollutant nitrogen monoxide NO.

3. $O + O \longrightarrow O_2$: aggregation of radical oxygen to form molecular oxygen is the conclusive step of the reaction.

Thermal Decomposition Reaction Rate

Atkins and Jones treated N_2O homogeneous decomposition as a first order reaction over the all pressure range, with kinetic parameters at standard conditions equals to: [39]

– Pre-exponential factor: $A = 7.94 \cdot 10^{11} \dfrac{1}{s}$

– Activation energy: $E_a = 250.00 \dfrac{kJ}{mol}$

Baulch et al proposed a more detailed kinetic study for the decomposition of nitrous oxide. [40, 25]
High pressure reaction rate (above 40 bar) have been found out not to be affected by the concentration of collision partner, reaction is thus of first order.
Moreover, collision efficiencies with different molecules are not to be considered, removing possible ambiguities in kinetics calculation.
At high pressure, formation of activated complexes by molecular collision occurs quickly and the step regulating the reaction rate is:

$$N_2O^* \longrightarrow N_2 + O \tag{2.21}$$

the form of the reaction rate, being a first order reaction, is:

$$k^\infty = A \cdot e^{-\frac{E_a}{R_u T}} \cdot [N_2O] \tag{2.22}$$

directly dependent on nitrous oxide concentration $[N_2O]$ and for which, inside the recommended temperature range $900 - 2100\,K$, kinetics parameters are:

– Pre-exponential factor: $A = 1.3 \cdot 10^{11} \dfrac{1}{s}$

– Activation energy: $E_a = 249.42 \dfrac{kJ}{mol}$

Low pressure decomposition kinetics (below 40 bar) is highly affected by the collision frequency and thus by concentration of colliding partner: reaction is second order.
Relative efficiencies for different partner collision have to be taken in consideration.

Reaction rate, being the reaction a second order thermal decomposition, is of the form:

$$k^0 = A \cdot e^{-\frac{E_a}{R_u T}} \cdot [N_2O]^2 \tag{2.23}$$

The only estimate for rate parameters, in the narrow temperature range $900-1050\,K$, is: [25]

– Pre-exponential factor: $A = 2.7 \cdot 10^{15}\,\dfrac{cm^3}{mol\,s}$

– Activation energy: $E_a = 247.81\,\dfrac{kJ}{mol}$

At intermediate pressure level, around 40 bar, the fall-off curve predict the rate constant:

$$k = \frac{k^\infty k^0 \, [N_2O]}{k^\infty + k^0 \, [N_2O]} \tag{2.24}$$

2.3.2 N_2O Catalytic Decomposition

As Kalback reports in his work, catalytic decomposition is a heterogenous reaction and the decomposition process can be schematized in a series of step in which a metal atom or a metal oxide activate a N_2O molecule. [38]

1. First step in the process consist in **adsorption** of a nitrous oxide molecule on an available active site on the catalyst surface: [41]

$$N_2O + {}^* \longrightarrow N_2O^* \tag{2.25}$$

2. Being nitrous oxide thus activated, catalytic active center reacts with a charge donation to N_2O activated molecule: metal atom chosen as active phase, or one of its oxides, should have local charge donation properties in order to destabilize $N - O$ bond.
   The result is the **surface reaction**: [41]

$$N_2O^* \longrightarrow N_2 + O^* \tag{2.26}$$

Catalyzing N_2O decomposition by means of a proper active phase avoids the formation in the product of nitrogen monoxide, thanks to the adsorption/desorption process which influences the reaction.

3. Final step in the catalytic process is the **desorption** reaction of atomic radical oxygen: [41]

$$2O^* \longrightarrow O_2 + 2^* \tag{2.27}$$

aimed at recombination of molecular oxygen out from the surface, freeing a couple of active sites.

Example of Catalytic Reaction Mechanism

Ruthenium oxidation process is proposed in the work of Pinna et al., who studied nitrous oxide decomposition on Ru/ZrO_2 catalysts.
The sequence of reactions showed hereafter can give a clear glimpse of how the process of activation of N_2O works. [42]
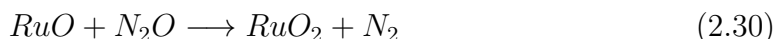Adsorption of radical oxygen leads to ruthenium oxidation, which consists in the surface reaction:

$$Ru + N_2O \longrightarrow RuO + N_2 \tag{2.28}$$
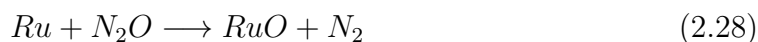
Oxidized active site can now interact together for the desorption of oxygen:

$$2O^* \longrightarrow O_2 \tag{2.29}$$

or there could be subsequent oxidation of the surface with a new N_2O molecule, according to:

$$RuO + N_2O \longrightarrow RuO_2 + N_2 \tag{2.30}$$

there is also evidence that, on reduced or partially oxidized catalyst, even $N-N$ bond can break down, leading to NO formation:

$$RuO + N_2O \longrightarrow (NO)RuO + \frac{1}{2}N_2 \tag{2.31}$$
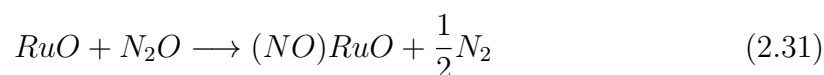
or, on highly reactive and unsaturated ruthenium site, it probably occurs:

$$RuO_2 + N_2O \longrightarrow RuO_3 + N_2 \tag{2.32}$$
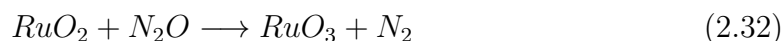
2.3.3 Catalysts for N_2O Decomposition

Several different catalyst have been studied and tested.
Kapteijn et al in their work [41] classify in an organized fashion the most relevant ones:

– Supported and unsupported metals

  – Pure and mixed oxides

  – Zeolitic systems

Supported metal is the most widely adopted solution in the field of monopropellant catalysts.

Typical supports consist of thermal stable materials: alumina, silica or zirconia. Alumina is the most widely adopted support, palladium or platinum with oxides of copper, cobalt, manganese or rhodium are among the best active phases. Zirconia usage is following an increasing trend combined with rhodium, copper.

Even metal oxides (correspondent to the metallic atom presented before) are, to a lesser extent, active as catalysts. The valency of an element, and so its oxidation state, is relevant to assess the activity of a metal oxide.

For example, activity order for Manganese subsequent oxidation states is: $MnO < MnO_2 < Mn_3O_4 < Mn_2O_3$.

Mixed oxidic systems, such as solid solutions, spinel and perovskites have been largely studied not only for N_2O decomposition but also for a deeper understanding of the catalytic process in general.

Solid solutions consist of transition metal ion dispersed in an inert oxide matrix.

Perovskites can be represented by the formula ABO_3: A is generally the larger atom catalytically inactive, mostly lanthanum, and B a metallic element like copper, chromium, iron, cobalt, nickel.

Characterized by structural and thermal stability, due high temperature preparation, Perovskites have very low surface areas, below $10 \text{ m}^2/\text{g}$, but they are very active. Varying the transition metal element in the compound $LaMO_3$, very low activation energy have been recorded. $(35 - 130 \text{ kJ/mol})$

Zeolitic systems are mostly based on transition metal ion, such as (Fe, Co, Cu, Mn, Ru, Rh, Pd) exchanged with a suited zeolite: ZSM - 5, ZSM - 11, USY, Ferrierite. Combination between metal ion and zeolite type determines the activity for N_2O decomposition.

The most studied zeolite is ZSM - 5 and activity order or metal ion is: Ru > Pd > Cu > Co > Fe > Pt > Ni > Mn. Decomposition can be modeled as a first order reaction, directly dependent on N_2O partial pressure p_{N_2O}, with an activation energy between 75 and 170 kJ/mol.

Very poor informations can be openly find in literature regarding rate parameter estimation for catalytic decomposition of nitrous oxide.

Hereafter are presented two of the catalyst solutions found in literature for which a kinetic study has been carried out and presented.

ZSM-5

ZSM-5, Patended by Mobil Oil Corporation in 1972, is quite simple to be synthesized and, having a very large surface area (400 m^2/g), is the most studied catalyst support in a huge variety of fields. [43]
ZSM-5 have been tested by Wood et al. in combination with iron an aluminum. [44] In the paper, the construction process of the Fe-ZSM-5 catalyst is described: the catalyst studied is prepared by thermal pretreatement of Fe/Al-MFI (Si/Al = 84 and Fe/Al = 0.38).
According to the data proposed in the paper, decomposition of N_2O starts above $623\,K$, without appreciable formation of NO.
Using plug flow reactor assumption, it has been estimated:

- <u>Pre-exponential factor</u>: $9.9 \cdot 10^8\ \dfrac{mol_{N_2O}}{mol_{Fe}Pa_{N_2O}s}$
  Based on the total amount of iron in the sample.

- <u>Activation energy</u>: $44.2\ \dfrac{kcal}{mol}$
  For steady-state decomposition rate.

Hexa-Aluminate

As reported above, alumina Al_2O_3 is one among the most used support for active phase metals. The real problem with alumina is related with its composition at high temperature.
At ambient temperature, alumina is in the form of γ-alumina and has a high surface surface area (200 m^2/g), correlated with a low surface energy. This is one of the most desirable properties for a catalyst support to have, since the exposed surface can be maximized, at equal weights. [45]
Unfortunately, at $700 - 800\,°C$ γ-alumina undergoes a phase transition, passing into θ-phase, with a reduction of surface area. As a consequence, part of the active phase laying on the surface is then absorbed and buried in the core: the catalyst loses part of its reactivity.
Situation even worsen with an additional temperature increase. Around $1050\,°C$ θ-alumina becomes α-alumina, which is recognized as a perfect fit for high temperature application, due to its high temperature resistance, but this type of alumina has very

low surface area (5 m^2/g), reducing even more catalyst activity. [46]

Lots of experimental work has been spent targeting the issue of alumina surface area loss at high temperature. Hexa-aluminate is a new material developed to tackle this problem.
It consists of alumina in which a heteroatom M, such as barium, lanthanum, manganese, replaces an aluminum atom in Al$_2$O$_3$ lattice: the chemical formula for the new compound is MAl$_{11}$O$_{18}$.
Presence of the heteroatom in alumina lattice prevents a phase change at high temperature, preserving alumina high surface area. [45]

Wickham et al. presented a study in which a wall-mounted catalyst have been tested for N$_2$O decomposition with different type of hexa-aluminates and different active phases.
For one of these combinations, the one with the highest reported reactivity, kinetic parameters have been extrapolated.
Hexa-aluminate supports are prepared starting from an aqueous solution of nitrate salts for each component, hydroxides of heteroatom are then co-precipitated with slow addition of ammonium hydroxide.
Sample are then dried and calcinated at 1000 $°C$ and hexa-aluminate is recovered as powder. Subsequently the powder coated a cylindrical-shaped section of porous ceramic foam to be used as a catalyst support.
Two different type of support, with different surface areas and active phase, have been manufactured: Hex-1 (56.3 m^2/g, rhodium) and Hex-2 (82.1 m^2/g, ruthenium).

Some final important considerations can be drawn:

– Preparation procedure of the catalyst support foresees a calcination at 1050 $°C$. This process produces also a high fraction of large mesopores, condition that enhance N$_2$O diffusion to the catalyst surface.

– The authors tested thermal stability of the presented supports by heating them up at 1000 $°C$ for 8 hours.
  Materials showed a loss of surface area of about 5 %.

– Kinetic measurements have been carried out on the most active catalyst tested. Data proposed for Hex-1 and Hex-2 are quite promising:

  1. Pre-exponential factor: $A = 7.09 \cdot 10^9 \, \dfrac{\text{g}_{\text{N}_2\text{O}}}{\text{atm} \, \text{g}_{\text{cat}} \, \text{min}}$

2. Activation energy: $E_a = 29.2 \frac{\text{kcal}}{\text{mol}} = 122.17 \frac{\text{kJ}}{\text{mol}}$

2.4 T_{ad} Prediction with NASA CEA

The NASA CEA (Chemical Equilibrium with Applications) is a Fortran-based program used to predict compositions and properties of complex mixtures at chemical equilibrium, without informations about the kinetics of the phenomenon.
The program is used in the framework of this thesis to preliminarily predict adiabatic decomposition temperature for N_2O with set of different initial pressures $p_{in} = 1$, 10, 20 bar and temperatures $T_{in} = 298.15$, 400, 550, 800 K.

$p_{in} = 1$ bar			
T_{in} [K]	298.15	400	550	800
T_{ad} [K]	1906	1977	2090	2287
$p_{in} = 10$ bar			
T_{in} [K]	298.15	400	550	800
T_{ad} [K]	1907	1978	2093	2298
$p_{in} = 20$ bar			
T_{in} [K]	298.15	400	550	800
T_{ad} [K]	1907	1979	2094	2300

Table 2.1: NASA CEA Results

The results, shown in Table 2.1, will be used in the following to:

– Evaluate the impact of uncertainties on the gathered thermodynamic dataset for N_2O, N_2 and O_2, as report in the following Section 2.5.

– Critically analyze the outcome of the catalyst simulator, which will be tested in (Chapter 4) with a variety of boundary conditions: initial temperature T_{in} shall be larger than 500 K to activate reaction and an initial pressure p_{in} exceeding 10 bar is needed to reduce pressure loss along the catalytic bed.

As it is clear from Table 2.1, final decomposition temperature is greatly varying with initial temperature, in particular it grows with increasing temperature, but it has poor dependence with respect to initial pressure.

2.5 Data Gathering for N_2O, N_2, O_2

A crucial part of the presented work consists in the construction of a reliable thermodynamic database for N_2O, N_2, O_2.

The only thermodynamic database freely accessible is the NIST-JANAF one: it gives, for all the three substances, a complete outlook of thermodynamic properties needed, which are:

- Specific heat at constant pressure c_p and at constant volume c_v

- Specific heat ratio γ

- Density ρ

- Sound speed a

Only for nitrous oxide:

- Entropy s

- Enthalpy h

- Internal energy u

- enthalpy of decomposition $\Delta H_r^{N_2O}$

NIST database can map variations of these quantities from 1 bar up to pressure in the order of tenths of MPa, far beyond what is requested in this thesis.

Different is the situation for a temperature mapping of these properties: saturation is a lower bond for the temperature in the dataset (this is applicable only to N_2O since it is studied in gas state, N_2 and O_2 do not condense at the temperature of interest) and, on the other hand, decomposition of the compound limits the temperature at which the latter can be studied. As a consequence, NIST database gives data for N_2O are available up to 525 K, for O_2 up to 1000 K and for N_2 up to 2000 K. Those temperature will be addressed as "limit temperature" for each compound in the following.

Only c_p values are available at higher temperature $(298 - 6000\,\text{K})$ for $1\,\text{bar}$ thanks to the polynomial Shomate equations, whose coefficients are reported as well in the NIST database.

Additionally, viscosity μ and thermal conductivity λ, useful in the framework of the catalyst simulation, Section 4.2, are obtained from direct interpolation of experimental results shown respectively in [47] and [48].
The spectrum of thermodynamic datas is completed with N_2O enthalpy of decomposition variation in temperature.
Using the NASA CEA program, enthalpy of N_2O decomposition reaction $\Delta H_r^{N_2O}$ is extracted at increasing temperature, up to 2500 K, and therefore employed in a ready-to-use interpolation function.

2.5.1 Data Extrapolation

From what is possible to observe in Table 2.1, with initial temperature T_{in} exceeding $550\,K$, decomposition temperature T_{ad} goes beyond $2000\,K$: NIST database of thermodynamic properties $(c_p,\ c_v,\ \gamma,\ \rho,\ a)$ for N_2O, N_2, O_2 shall be expanded up to $2500\,K$.
Databases expansion is actually a pure numerical task, relying on some physical assumptions (i.e. ideal gas), which consists in some steps:

1. For all three compounds, c_p values for pressure larger than $1\,\text{bar}$ are obtained through an extrapolation process.

2. From the obtained c_p values and relying on ideal gas assumption, database of the other properties is extended up to $2500\,\text{K}$, even for pressure larger than $1\,\text{bar}$.

Once database for $(c_p,\ c_v,\ \gamma,\ \rho,\ a)$ has been created, MATLAB interpolation functions will interpolate for a specific input (p,T) couple over the created dataset.
Therefore, once pressure and temperature are known, all relevant thermodynamic properties can be computed.

Data for s, h, u available from NIST for N_2O, up to $525\,\text{K}$, are not subjected to the extrapolation process, since their values at high temperature are out of interest for the scope of the thesis. They are used in simulating tank outflow dynamics (Chapter 3), a process occurring at temperature far below than $525\,\text{K}$.
To this regard, three MATLAB interpolation functions are created to give as output a set of (p, T) values at constant s, h or u.

Step 1: c_p Values Extrapolation

Figure 2.1 helps in understanding the extrapolation process carried out for N_2O, N_2, O_2. Subsequent steps in the procedure are highlighted only for what concerns $c_{p_{N_2O}}$ values. What is now discussed for N_2O is the process followed also for N_2, O_2 with their respective limit temperatures.

Starting point for the extrapolation are c_p values directly extracted from the NIST database. First plot of Figure 2.1 shows $c_{p_{N_2O}}$ values, up to the limit temperature of 525 K.
Second plot of Figure 2.1 shows the c_p curve from the Shomate equation (blu line), at 1 bar and up to 2500 K. This is addressed as "Shomate curve" in the following.

c_p curve at higher pressures (up to 50 bar for N_2O and to 30 bar for N_2, O_2) are reconstructed numerically:

- Gradient of the Shomate curve is computed in the high temperature region (from limit temperature up to 2500 K).

- This gradient is approximated to be the same for all the c_p curves of the envelope (from 1 to 50 bar in the case of N_2O)

- High pressure c_p curves (beyond 1 bar) are extended in the high temperature region, with the same shape of the Shomate curve.
  Starting from the value at 525 K, c_p values are computed, according to the previously computed gradient, for increasing temperature steps.
  Result of this process is presented in the third plot of Figure 2.1.

The outcome is a dataset of c_p values for N_2O, N_2, O_2 whose temperature and pressure limit are summarized in Table 2.2.
This is a procedure defined only in the frame of this thesis, for the specific goals the thesis aims at. No literature has been considered in this regard.

It is acknowledged that forcing the same gradient to all the curve in the pressure envelope is an approximation, and being so it introduces some errors.
Those errors will be larger for N_2O, for which extrapolation is carried out starting from 525 K.
In the following Section 2.5.2, those c_p values are used to estimate theoretically the decomposition temperature for N_2O: error in the estimation of decomposition temperature are critically evaluated and motivated.
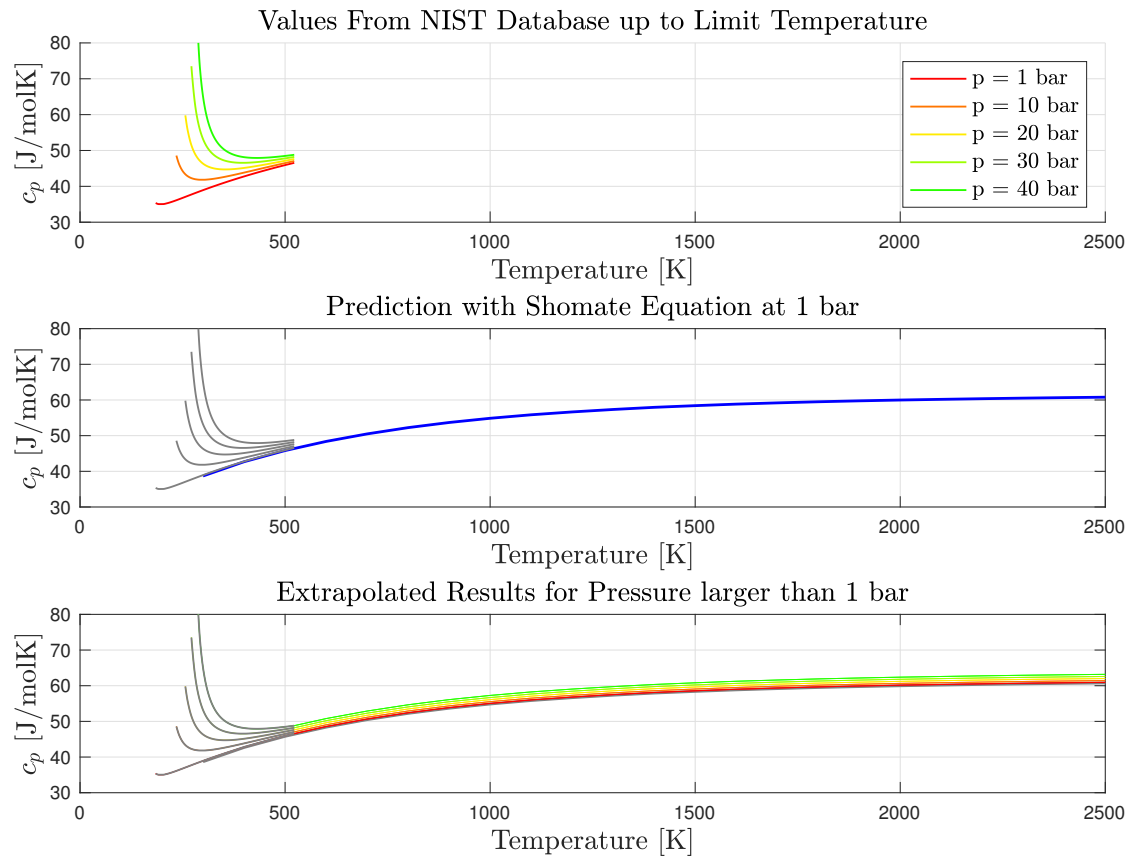
Values From NIST Database up to Limit Temperature

Prediction with Shomate Equation at 1 bar

Extrapolated Results for Pressure larger than 1 bar

Figure 2.1: Illustration for Extrapolation Procedure

	Temperature [K]		Pressure [bar]	
	Min	Max	Min	Max
N_2O	T_{sat}	2500	1	50
N_2	200	2500	1	30
O_2	200	2500	1	30

Table 2.2: Pressure and Temperature Limits for Databases

Step 2: Database Extension with Ideal Gas Assumptions

In the high temperature domain, ideal gas model is actually a good estimate for gas thermodynamic properties.

From Figure 2.2, in which compressibility factor Z is plotted for N_2O, N_2, O_2, it is clear that ideal gas assumptions can be reasonably adopted beyond their respective limit temperatures, being Z almost unitary for all three substances.

It is important to note that plots for N_2 and O_2 have a much smaller scale than the N_2O one. Moreover, comparing with the color scale and looking at the oscillating contour lines, Z values experience some pretty small spurious numerical oscillation.

Database for c_v, γ, a are extended on the basis of the c_p dataset: $c_v = c_p - R$ is used to estimated specific heat at constant volume (R is the gas constant), specific heat ratio is computed as $\gamma = c_p/c_v$ and finally sound speed is $a = \sqrt{\gamma R T}$.
Density is computed as $\rho = p/RT$, according to ideal gas law.

2.5.2 T_{ad} Theoretical Computation

Recovering notions of chemical reactions, it is possible to equate the enthalpy of reaction of a compound, in standard condition (lefthand side term in Equation 2.33), to the amount of heat requested to bring the products from standard temperature up to the adiabatic flame temperature.
This is a reliable approximation of the exact thermodynamic path of a chemical reaction on the $(h - T)$ plane.

$$\Delta H_r^{N_2O}(T) = \Delta H_f^{N_2} + \Delta H_f^{O_2} - \Delta H_f^{N_2O} \tag{2.33}$$

Knowing that enthalpy of reaction of a compound consists in the summation of the enthalpy of formation (at $T_{std} = 298.15\text{K}$) of the products minus the summation of the enthalpy of formation of the reactants, for N_2O this translates in:

$$\Delta H_r^{N_2O}(T) = -\Delta H_f^{N_2O} \tag{2.34}$$

being products of the decomposition pure substances, with zero heat of formation.
Knowing enthalpy of reaction for N_2O and specific heat c_p variation in temperatures for both O_2 and N_2, T_{ad} can be numerically calculated from:

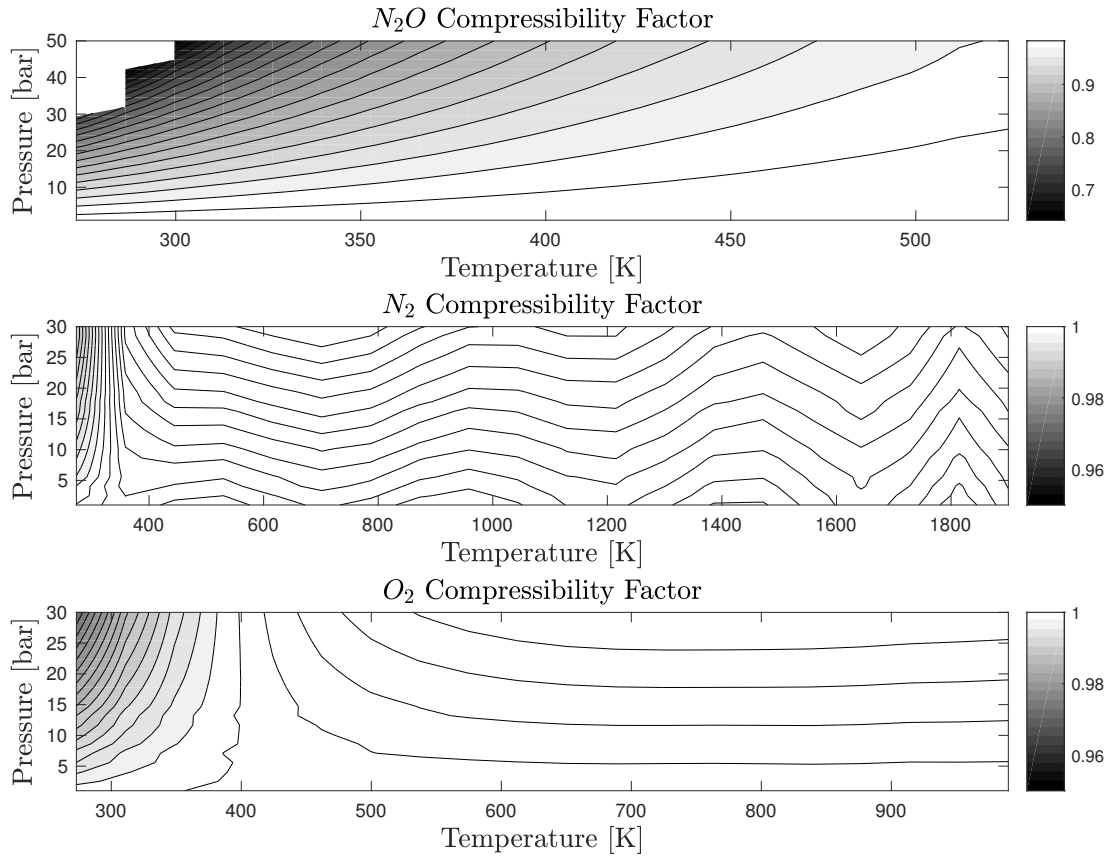$$\Delta H_r^{N_2O}(T) = \int_{T_0}^{T_{ad}} c_{p_{N_2}}(T) + \frac{1}{2}c_{p_{O_2}}(T) \, dT \tag{2.35}$$

Figure 2.2: Compressibility Factor up to Limit Temperature

	$T_{in} = 298.15\ K$	$T_{in} = 400\ K$	$T_{in} = 550\ K$	$T_{in} = 800\ K$
$P_{in} = 1\ bar$	0.9 %	1.2 %	3.5 %	12.4 %
$P_{in} = 10\ bar$	0.8 %	1.0 %	3.2 %	12.1 %
$P_{in} = 20\ bar$	0.6 %	0.8 %	3.1 %	11.9 %

Table 2.3: Error in T_{ad} estimation between NASA CEA and Equation 2.35

Results obtained with the theoretical formulation are compared with T_{ad} estimation using NASA CEA on an envelope of initial pressure and temperatures.

Outcome of the comparison is reported in Table 2.3. The general trend is that the larger the starting temperature, the bigger the error committed in the estimation of

T_{ad}.

Main reason for this increasing error is not to be searched in the extrapolation procedure performed. On the contrary, this is a prediction error ascribable to the Shomate equation.

Looking more carefully to the results, errors in the estimation of T_{ad} at higher pressure are pretty close to the error committed estimating T_{ad} at 1 bar, with c_p from Shomate equation.

As a consequence, as long as initial temperature increases, estimating T_{ad} with c_p values computed from the Shomate equation leads to a larger error. This actually reflects into an error on the extrapolated values at higher pressure.

It is also worth pointing out that, for the computation performed with Equation 2.35, only c_p values for N_2 and O_2 are used: they are the most precise data available, with respect to N_2O for which experimental results are available up to a lower temperature.

The error is relatively small at $T_{in} = 298.15$ K, but starts growing beyond 600 K (i.e. error is 12% at $T_{in} = 800$ K).

The expectation is that, if $c_{p_{N_2O}}$ data had been somehow employed (as will happen in the framework of a plug flow reactor model, presented in Chapter 3) the error would have been larger.

This represents a crucial point that will be analyzed more in detail during Chapter 4, where catalytic decomposition results will be presented and discussed.

Chapter 3

Modeling of the System

Recalling what has been presented in Chapter 1, the system to be modeled is an assembly of components:

– Tank

– Injector

– Catalyst

– Nozzle

This chapter deals with the process employed to model each part of the assembly. In particular, this process is articulated into three steps:

1. Real system identification. Each part of the assembly is macroscopically described to define their main operating principles.

2. Physical model. Real components are schematized according to some simplifying physical assumptions in a physical model, whose operational principles are much easier to be simulated.

3. Mathematical model. Operational principles for the physical model are converted into equations to be solved to simulate system behavior.

3.1 Real System Identification

As reported in Chapter 1, a monopropellant thruster is an assembly of several components, connected in series.
The assembly considered for the simulation is made by:

- Tank

- Injector

- Catalyst

- Nozzle

3.1.1   Tank

The tank, together with the main valve (which is not simulated in this thesis), represents the propellant storage unit.
The materials used to build the tank shall withstand two basic requirements:

- High mechanical strength in a wide range of temperatures and internal pressure.

- No chemical activity with the fluid stored inside, so as to avoid corrosion problems as well as structural weakening.

Fluid is usually stored in liquid phase to maximize the compactness of the overall unit. In case the selected propellant has a low vapor pressure in liquid phase, a pressurization system, working with an inert gas such as nitrogen N_2, is required to push the propellant through the injector and inside the catalyst.
As previously reported, since N_2O has a large vapor pressure, no pressurization system is needed in this situation.

3.1.2   Injector

The injector is a fundamental part of the assembly. Basically, an injector is made up by a metal block, flanged to the rocket structure, with an inlet single hole directly connected to the main valve and a properly designed hole pattern on the opposite side.

The design of the hole pattern of an injector is aimed at different purposes:

- Distribute the propellant from the tank over the catalyst cross-section, assuring a proper velocity and residence time for the fluid reacting in the catalyst.

- Granting a correct pressure jump from the tank exit to the catalyst inlet, in order to avoid back-flow events.

- Atomization of propellant, if liquid, to ease its decomposition inside the catalyst.

3.1.3   Catalyst

Catalyst is the core of every monopropellant thruster. It usually consists of a cylindric case inside which pellets of various geometry are contained in a so called " packed bed configuration". These pellets, built with a high-temperature resistant material, are covered on their surface with the active phase responsible of the catalytic reaction.
Geometry of the pellets greatly influences the exposed surface area to the fluid: the higher is the packed bed superficial area per unit volume, the more is the number of possible active site able to trigger the decomposition process. On the other hand, a too stressed increase of the superficial area would be detrimental by the point of view of momentum losses.

Pellets containment inside the catalyst is another issue to be tackled. Since a packed bed reactor consists in a pile of pellets facing a flow of propellant, grids shall be put on both end of the case to stuck pellets inside the catalyst.
Moreover, a gap between the injector plate and the inlet grid is gained to facilitate recirculation and mixing of the fluid right after injection.

External case

Since monopropellant exothermic decompositions are characterized by very high decomposition temperature, catalyst case should be properly designed in order to account for high thermal stresses.
Usually a metallic material with high temperature resistance is used and, if not sufficient, an insulation strategy is adopted.
As shown previously, N_2O decomposition implies temperatures that can exceed $2000\,K$ and so remarkable thermal loads weigh on the external case. This is why Hastelloy X alloy has been selected for the case of the catalyst.

Hastelloy X is a brand new nichel-chromium-iron-molybdenum alloy high-temperature and oxidation resistant able to keep good ductility even at temperature in excess of $1000\,K$ for a large amount of hours: thus it is exceptionally resistant to stress-corrosion cracking in petrochemical applications.
Easy fabrication makes Hastelloy X a material easy to use and maintain: it has an excellent forming and welding properties, can be welded with a large variety of techniques (shielded metal arc, gas tungsten arc, gas metal arc).
Hastelloy X is mainly used in gas turbine engine exposed to combustion and in in-

dustrial furnace application, due to its very peculiar oxidation resistance. [49]
From properties data sheet, this alloy shows a remarkable 97 MPa ultimate tensile
strength and 43 MPa yield strength (at 0.2 % offset) at a temperature of 1093 °C.
However it is not sufficient to withstand alone thermal stress implied in N_2O decomposition.

Internal insulation

An insulation strategy is adopted for the internal surface of the case.
N_2O decomposition temperature is far higher than Hastelloy X melting point, observed at $1260 \div 1355\,°C$.
An insulation must be used to counteract this issue.
In addition, the adoption of an insulation strategy is beneficial for the overall performance of the thruster: minimum amount of heat is dissipated through the case,
mixture can reach nozzle inlet with the highest possible reaction temperature, maximizing specific impulse. [23]
Thermal barrier coating (called TBC in the following) will be adopted as insulation
strategy.
TBCs are based on ceramic materials (high melting point and low thermal conductivity). They are widely used in aerospace-related applications, such as gas turbine
engines, since they lower metal surface temperature and thus they protect it from
harsh thermal oxidation.
The real challenge in the usage of ceramic materials is represented by different chemical and physical properties with respect to a metal. Main problem is the difference
in thermal expansion coefficient, which is lower for a ceramic. [50]

TBC is typically made of two layers:

1. <u>Metallic bond coat</u>. A 100 μm layer, made of aluminades of Platinum and
   Nichel [50], which providse substrate oxidation and corrosion protection. [51]
   It increases adhesion between the top ceramic coat and the metallic substrate.
   [50]

2. <u>Ceramic top coat</u>. Zirconia-based ceramics are the most employed in the field
   and in particular Yttria-stabilized Zirconia (YSZ in the following) is the most
   suitable thanks to: [50]

   2a. High melting point ($2600 \div 2700\,°C$).

    2b. Low thermal conductivity $(0.8 \div 2.9 \, \text{W/(mK)})$ due to the large presence of point defects. [50, 51]

    2c. High termal expansion coefficient $(10.1 \cdot 10^{-6} \, \text{K}^{-1}$ at $873 \, ^{\circ}\text{C})$ reducing thermal stresses between the coating and the underlying metal (thermal conductivity $16.4 \cdot 10^{-6} \, \text{K}^{-1}$ at $899 \, ^{\circ}\text{C})$ [49, 50]

3. <u>Fracture resistance</u>. In case YSZ intermolecular bonds are broken, bonds with higher atomic packing factor are naturally formed to fill the crack. [50]

4. <u>Oxygen migration</u>. Zirconia shows high oxygen ion conductivity at high temperature. Since YSZ has an interconnected network of pores, the result is a rapid oxygen migration through the ceramic layer.
   This phenomenon leads to the formation of a thermally grown oxide (TGO in the following) layer onto the metallic bond coat layer and plays an important role in TBC performance: it provides strong bonding between YSZ and underlying metal, but also poses threats due to spallation failures. [50, 51]

Thermal conductivity of YSZ layer depends on the pore morphology within the coating and thus to the deposition technique adopted.
There are at least three methods for TBC deposition:

– <u>Air Plasma Spraying APS</u>. This method produces pores roughly aligned with the underlying surface and fine grain size.
As a result, YSZ has very low thermal conductivity $(0.8 - 1.1 \, \text{W/(mK)})$, but the layer shows low surface smoothness. [51]
APS is a cost-effective technique with high deposition rate, but the need of high operation temperature and a decontaminated environment limits its applications. [50]

– <u>Electro Beam physical Vapor Deposition EB-PVD</u>. It produces collinear elongated single crystal columns, predominantly orientated on the normal to the coated surface, containing a small volume fraction of intercolumnar pores.
This gives the resulting TBC a high strain tolerance and spallation resistance, but higher thermal conductivity $(1.5 - 1.9 \, \text{W/(mK)})$. [51]
This method has high deposition rate and assure strong chemical bonding between YSZ and the substrate, but sets high standards for the deposition systems. [50]

– <u>Chemical Vapor Deposition CVD</u>. With respect to other techniques, more complicated-shaped geometries can be processed with CVD. It has a better

repeatability but a lower deposition rate and less controllability of coatings quality. [50]

CVD is able to grow uniform, dense columnar YSZ thin films.

Among the presented deposition method, CVD is the one selected as most suitable to cover the internal surface of the catalyst case.

Deposition machines are able to deposit thiny films of YSZ, in the order of some tenths of μm. [50]

3.1.4 Nozzle

Inside a converging-diverging nozzle, attached at the exit section of the catalyst, enthalpy of the mixture coming from the catalyst is converted into kinetic energy through an expansion process.

The nozzle, more than other components, must withstand severe working conditions in terms of pressure and temperature, in particular at the inlet section and inside the convergent part, where temperature and pressure are still close to the catalyst values. The most widely adopted material is **graphite**, which has great thermal resistance but suffers from fragility problems.

Internal surface of the nozzle is important to be smooth enough to avoid any reconversion process: anytime flow is decelerated by an obstacle, static temperature increases greatly posing threats to the thermal resistance of the material.

The design process of a nozzle is centered on the selection of the optimum expansion altitude: over- and underexpansion, which are non-optimality expansions, occur when flying below or above this altitude.

Overexpansion is the most critical condition between the two: a shock wave forms in the discharged plenum and can travel back inside the nozzle if altitude is too low with respect to the design condition.

According to the planned mission profile, optimum altitude has to be set in order to have the least negative effect from off-nominal flying conditions.

Since the nozzle, in the framework of this thesis, is used for an on-ground test, without variation in altitude and therefore in ambient pressure, the selection of the design point is trivially the $z = 0\,$m condition.

3.2　Physical Model

3.2.1　Tank

Prior to tackle directly the issues related to tank outflow simulations, N_2O shall be investigated in order to define if it can be considered an ideal or real gas, inside the envelope of working conditions.

First plot of Figure 2.2 shows that inside the envelope of working conditions for the tank, (pressure larger than 10 bar and temperature below 298.15 K) compressibility factor, here used as an indicator for gas ideality, is quite different from 1 (ideality condition).

An error of $20 \div 30\%$ is expected to be committed with the ideality assumptions.

N_2O must be considered a real gas in the simulation of tank outflow dynamic.

In order to compare both ideal and real conditions, tank outgassing is also simulated as an **adiabatic process** under ideal gas assumptions, following the relations presented in [52].

Joined results will be presented in Chapter 4 in order to compare the two simulations.

In order to simulate N_2O outflow from the tank as a real gas expansion, the tank shall be accordingly modeled. A scheme is presented in Figure 3.1

Tank is therefore subdivided into two main parts whose operational conditions are simplified with some assumptions:

– Core. The internal part of the tank is supposed to store **still** gaseous nitrous oxide, which remains at zero velocity through all the outflow process. Internal thermodynamic properties can be spoken about as **global** or **total quantities**. Pointing out the definition of the 1st principle of thermodynamic:

$$du = dq + pdV \tag{3.1}$$

the formulation can be simplified with two fundamental assumptions:

1. Nitrous oxide outflow from the tank is a really fast process. As a result, process can be reasonably assumed as **adiabatic**: $dq = 0$

2. The tank has a fixed shape and thus outflow process occurs at **constant volume**: $dV = 0$

Consequently, a **constant internal volume** process $du = 0$ regulates time variation of total thermodynamic properties inside the tank.
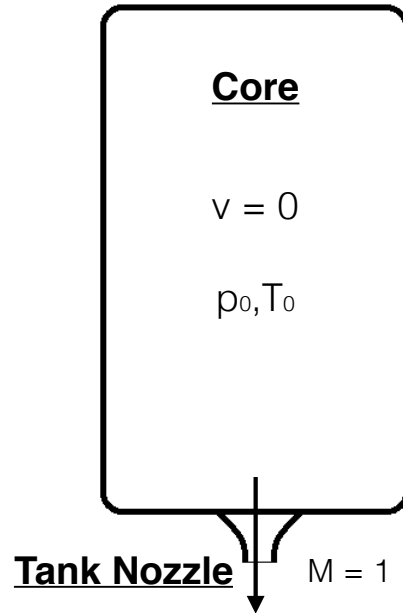
Core

v = 0

p_0, T_0

Tank Nozzle M = 1

Figure 3.1: Tank Physical Model

– <u>Tank Nozzle</u>. A simply convergent nozzle, called "tank nozzle"in the following, is set to discharge nitrous oxide out from the tank and directly through the injector.
Due to process quickness and negligible effect of friction on internal walls, the discharge process inside the tank nozzle is assumed to be **isentropic**: $ds = 0$. Since pressure of the gas inside the tank is much higher than external ambient pressure, the convergent nozzle remains choked for all the duration of the discharge phase: this means **sonic conditions** are present on the outlet section of the tank nozzle.

3.2.2 Injector

Injector is modeled as a **concentrated head loss**, whose pressure jump is computed according to what presented in the international standards for compressible fluid flows in differential pressure devices. [53]
Injector holes pattern has been selected as a compromise between pressure losses and proper distribution of injected flow through the catalyst cross section: holes are located in the center and along two concentric circumferences, equally spaced from

the external case, for a total of 13 holes.
Graphical representation is given in Figure 3.2.
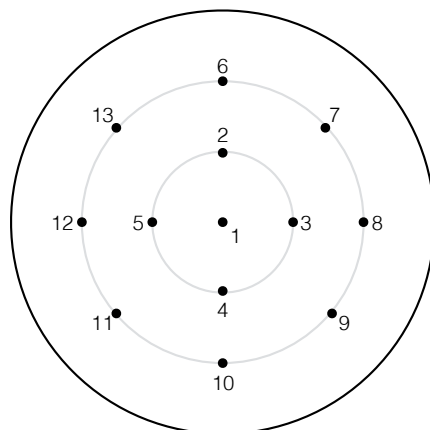
Figure 3.2: Representation of Injector Holes Pattern

For what concerns the estimation of the complete properties pattern of N_2O after injection, temperature is computed on the basis of the estimated pressure loss relying on the assumption of **isoenthalpic flow** (usual when dealing with rapid flow passage through an orifice).

3.2.3 Catalyst

Catalyst is modeled as a plug flow reactor (PFR). A plug flow reactor consists of a constant cross-section hollow cylindrical tube. Even if a plug flow reactor can be completely filled with reacting mixture, in the following a packed bed configuration is chosen: the reactor is filled with spherical pellets and reacting mixture flows through them. [36]
Figure 3.3 (Courtesy of [54]) shows, only as illustrative purpose, a packed bed reactor fill with hollowed cylindrical pellets. Treating the catalyst as a plug flow reactor leads to some important simplifications:

 – Steady state simulation.

 – Properties of the mixture varies along the catalyst axis only.

 – Mixture properties are uniform over cross-section.
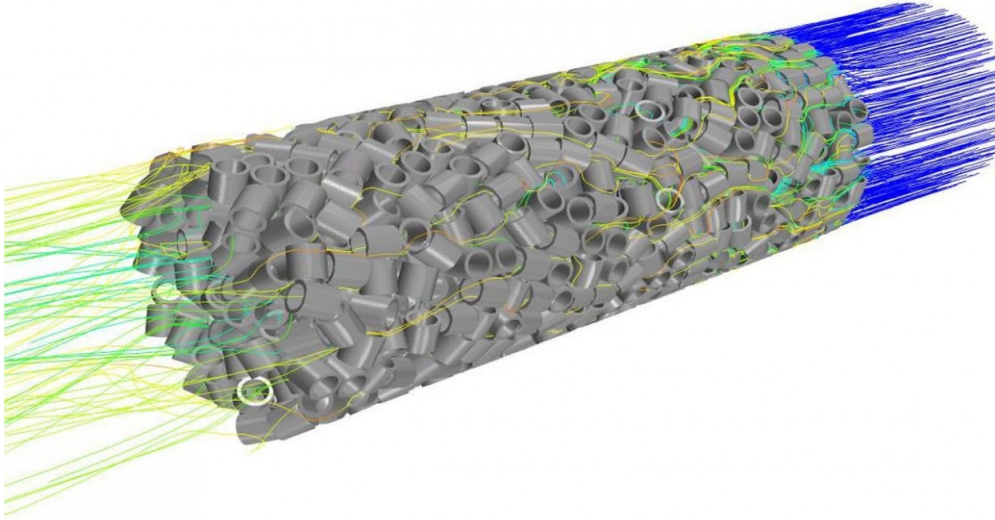
Figure 3.3: Packed Bed Column of Hollowed Cylindrical Pellets

– Complete mixing along radial direction and no mixing along longitudinal direction: no concentration variation over cross-section.

– No back-mixing occurring in the reactor.

– Velocity is uniform over the cross section, it varies only along the axis due to changes in mixture properties and composition.

– Pellets and decomposing mixture do not exchange heat.

Reaction Rates

Reaction rate for the overall decomposition process consists in the superposition of both catalytic and thermal decomposition reaction rates.
Catalytic reaction rate is dominant at lower temperature.
As soon as temperatures increases, catalyst support starts a phase change process (referenced in Chapter 2) and progressively loses its effectiveness.
Once catalyst has lost a large amount of its effectiveness, thermal decomposition (which is now fast enough at such a temperature) is the ruling decomposition phenomenon.
This is actually a switch from catalytic to thermal decomposition, which is in first instance approximated as an abrupt shift occurring at precise temperature $T_{sw} =$

1200 K, at which catalyst is assumed to lose all its effectiveness. This temperature has been selected in accordance with experimental studies on hexa-aluminate, reported in Chapter 2: support can withstand temperature above 1000°C wihtout a phase change.

Further analysis are performed accounting for the switch as a continuos process, in order to assess the impact of this uncertainty on the model. This results are shown in Chapter 4.

For thermal decomposition kinetics, data from Atkins and Jones [39] textbook are recovered:

$$A_t = 7.94 \cdot 10^{11} \, \frac{1}{s} \qquad E_{a_t} = 250.00 \, \frac{kJ}{mol} \tag{3.2}$$

On the side of catalytic decomposition, work by Wickham et al. on hexa-aluminate supports is selected due to its promising performances and innovative selection of materials. Arrhenius law constants for catalytic decomposition are:

$$A_c = 7.09 \cdot 10^9 \, \frac{g_{N_2O}}{atm \, g_{cat} \, min} \qquad E_{a_c} = 122.17 \, \frac{kJ}{mol} \tag{3.3}$$

for a ruthenium active phase. [45]

Catalyst Case and Insulation Layer

Catalyst case consists of a hollow Hastelloy X cylinder covered on its internal surface with an insulating layer of Yttria-stabilzed Zirconia. An illustration is given in Figure 3.4.
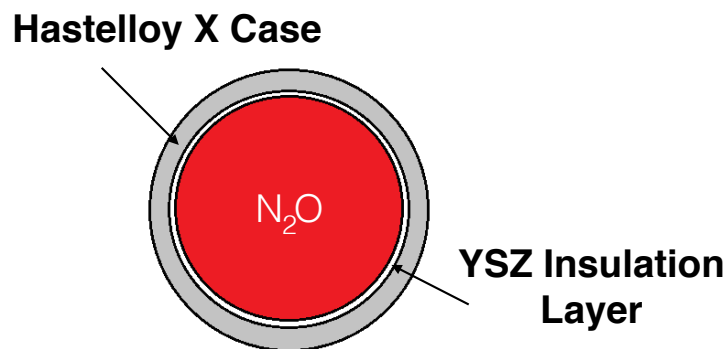
Figure 3.4: Catalyst Case and YSZ Layer

The procedure followed to define both thicknesses is presented: case thickness is computed with a mechanical approach, while thickness for YSZ layer is defined through

a thermal approach.

Both estimations are given in the worst case scenario: the end of the catalytic bed experiences the highest thermo-mechanical loads (T_{ad} is reached at the end of N_2O decomposition, in the following temperate at the end of catalyst is named T_{end}). In this situation, according to the known performances of both Hastelloy X and YSZ (reported in Chapter 2), YSZ shall insulate the case so as to have an interface temperature of 1000 K (perfectly sustainable by Hastelloy X and largely within expected performances for YSZ).

Yield strength for Hastelloy X at 1000 K is $\sigma_y^{hx} = 43$ MPa. Using this value together with catalyst pressure p_{design}^{cat} (accordingly margined) and catalyst bed diameter, thickness t_{hx} is estimated.

A thermal energy balance between decomposing N_2O and YSZ hollow cylindrical layer is used to estimate the thickness the YSZ layer shall have to get an interface temperature of 1000 K.

Thermal Exchanges

Catalyst simulation accounts for energy dissipation but, due to plug flow assumptions, there is no convection exchange between the mixture and pellets: catalyst supports are supposed to be isothermal with surrounding mixture.

The mixture exchanges heat only via conduction through the catalyst wall.

This is a fixed-temperatures conduction problem, to be solved with two boundary conditions:

- – Internal surface temperature, which is equal to the reaction temperature itself due to the plug flow assumption.

- – Ambient temperature.

An overall heat transfer coefficient is therefore computed for a series of three thermal resistances, in a hollow cylindrical geometry:

1. YSZ insulation layer (Conduction)

2. Hastelloy X catalyst case (Conduction)

3. Still air surrounding the catalyst (Natural Convection)

3.2.4 Nozzle

The decomposed mixture, at high temperature and pressure exiting the catalyst, can now be expanded in the nozzle. Reasonably, at this high temperatures, the mixture behavior is approximated as an ideal gas behavior. [1]

In addition, some other assumptions can be used to simplify the real nozzle to an ideal nozzle.

Usually for chemical rocket propulsion, measured real propulsive parameters differ of about 1 to 6% from the ideal calculated ones.

These ideal propulsive parameters are computed with the following set of assumptions:

- Discharged flow is a gaseous mixture of N_2 and O_2 in stoichiometric ratio, treated as an ideal perfect gas.

- Heat transfer across the nozzle wall is negligible along with friction and all boundary layers. Expansion is, as a result, isentropic.

- Gas velocity and all the other thermodynamic quantities are uniform over any cross section.

- Inside the nozzle, chemical equilibrium is established: flow is frozen $(N_2 + \frac{1}{2}O_2)$, with constant composition.

3.3   Mathematical model

In Figure 3.5 is reported a brief scheme to better understand the blowdown sequence and the respective thermodynamic properties calculated.

Tank	Tank Nozzle	Injector		Catalyst	Nozzle	
				p		
p_{tank}	p_{exit}	p_{inj}	p_0	T	p_{end}	p_d
T_{tank}	T_{exit}	T_{inj}	T_0		T_{end}	T_d
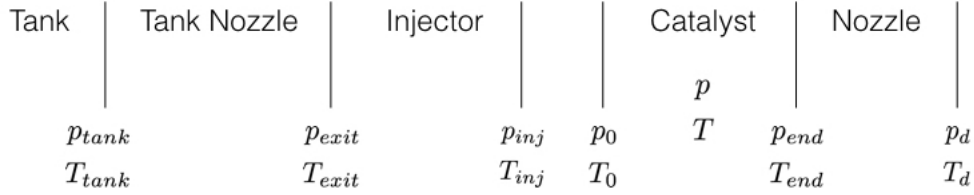
Figure 3.5: Scheme of the Blowdown Sequence

3.3.1   Tank

Simulation of the tank outflow dynamics is performed through a double-nested loop iterative process, schematized in Figure 3.6: total (tank) pressure p_0 and temperature T_0 are recursively updated at each iteration.

The iterative loop runs following a precise order of steps:

1. Since flow through the nozzle is considered to be **isentropic**, entropy during the expansion is conserved and it is equal to the entropy of N_2O inside the tank.
   Identifying the entropy from total conditions (p_{tank}^i, T_{tank}^i), a set of isentropic (p_s, T_s) data can be gathered from the N_2O properties database.
   As a result from the assumption made, the exit nozzle condition would be a couple of points inside this set.

2. In order to identify the correct couple of (p_{exit}, T_{exit}) values at the exit section of the tank nozzle, each couple of data inside the (p_s, T_s) set is checked inside a first inner iterative loop.
   Since for every (p_s, T_s) couple N_2O thermodynamic properties are known, the value of the discharge outside velocity is computed as:

$$v_{exit} = \sqrt{2\left(c_{p_{N_2O}} T_s - c_{p_{N_2O}}^{tank} T_{tank}\right)} \tag{3.4}$$
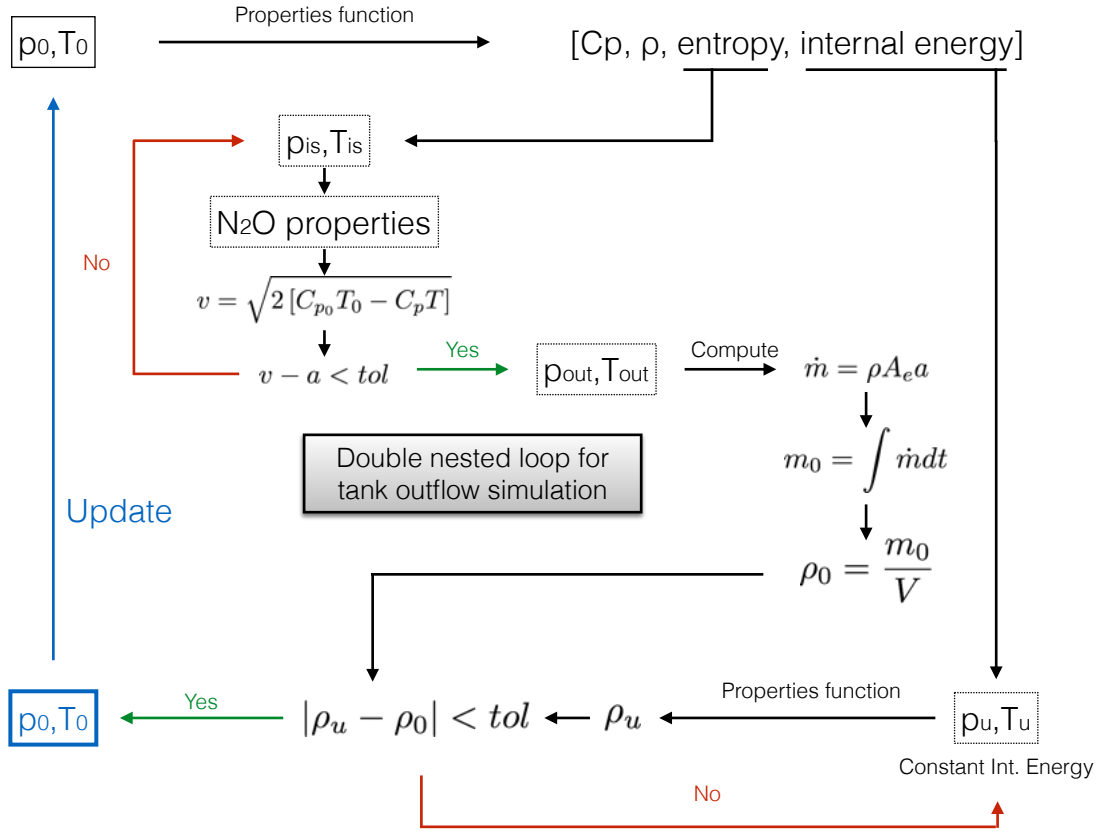
Figure 3.6: Mathematical Model for Tank Outflow

and then compared to the value of sound speed a available from the N_2O properties in that condition: when values are close enough, meaning that Mach number $M_{exit} = 1$, this inner iterative loop stops giving (p_{exit}, T_{exit}), N_2O pressure and temperature at the exit section of the nozzle.

3. Having defined pressure and temperature of the gas after expansion through the tank nozzle, all thermodynamic properties at the exit section can be computed. Consequently, value for the instantaneous mass flow rate discharged by the nozzle can be defined as:

$$\dot{m} = \rho_{exit} A_{exit} a_{exit} \tag{3.5}$$

4. Integration of mass flow rate leads to N_2O mass value of the remaining gas inside the tank:

$$m_{N_2O} = \int \dot{m}\, dt \tag{3.6}$$

and straightforwardly even density value can be computed:

$$\rho_{N_2O}^{tank} = \frac{m_{N_2O}}{V_{tank}} \tag{3.7}$$

5. Iterations inside a second outer iterative loop can define the new total thermo-dynamic condition inside the tank $(p_{tank}^{i+1}, T_{tank}^{i+1})$.
Knowing that tank deflation process is assumed to happen at **constant internal volume**, from the current tank properties $(p_{tank}^{i}, T_{tank}^{i})$ internal energy is computed and a set of (p_u, T_u) values at constant internal energy can be derived from N_2O thermodynamic properties database.
For each (p, T) couple inside (p_u, T_u) set, value of N_2O density can be derived and compared with the density value after integration $\rho_{N_2O}^{tank}$.
When a couple of pressure and temperature corresponds to a density value which match $\rho_{N_2O}^{tank}$, iterations stop giving the updated total thermodynamic characteristics of the tank $(p_{tank}^{i+1}, T_{tank}^{i+1})$.

6. As a consequence, knowing $(p_{tank}^{i+1}, T_{tank}^{i+1})$, all tank properties, at instant $i+1$ are known.
The loop is now completed.

Tank Sizing

In the framework of this work, sizing of the tank consists only in selecting the more appropriate geometry and wall thickness.
As it will be proposed in the following for the catalyst case sizing, for a cylindric geometry there is a clear difference between **hoop** or **circumferential stress** and **longitudinal stress**, being the former twice the latter:

$$\sigma_h = \frac{p_{design}^{tank} r_{tank}}{th_{tank}} \qquad \sigma_l = \frac{p_{design}^{tank} r_{tank}}{2th_{tank}} \tag{3.8}$$

where th_{tank} is the tank wall thickness and r_{tank} the tank internal radius.
Sizing for a cylinder is therefore carried out accounting for the larger hoop stress: if it does not reach the yielding limit in operational conditions, the structure is safe.
For a spherical geometry the only stress corresponds to the longitudinal one, which is the same in all directions.
Shape is selected between a simple sphere and a cylinder covered with two hemispheres at its ends, as it will be pointed out in Section 4.1.3

3.3.2 Injector

Simulation of the N_2O injection properties is computed following a step process:

1. On the basis of the pressure/temperature vs. time trend estimated for the flow exiting from the tank, at each time instant a set of (p_h, T_h) data at constant enthalpy is defined.

2. Proceeding further in the same time instant, injection pressure can be computed according the formula suggested in [53]:

$$p_{inj} = p_{exit} - \frac{1}{2\rho_{exit}} \left[\frac{\dot{m}}{C_d Y A_{inj}} \right]^2 \tag{3.9}$$

with discharge coefficient $C_d = 0.88$ for a 1 mm hole, as reported in [1], injection area $A_{inj} = n_{hole} \pi d_{hole}^2$ and compressibility factor computed as:

$$Y = 1 - \left(0.351 + 0.256 D_{ratio}^4 + 0.93 D_{ratio}^8 \right) \left[1 - \left(\frac{p_{inj}}{p_{exit}} \right)^{\frac{1}{\gamma}} \right] \tag{3.10}$$

where $D_{ratio} = \dfrac{d_{hole}}{d_{bed}}$ is the ratio between hole diameter d_{hole} and catalyst bed d_{bed}.

3. As similarly done within tank simulation, the computed injection pressure p_{inj} is used to eztract from the isoenthalpic (p_h, T_H) curve the correct value of temperature T_{inj}: entering the (p_h, T_H) curve with a known pressure the correspondent temperature is extracted.

3.3.3 Catalyst

The quantities to be mapped during the prediction of N_2O decomposition path are: mixture pressure p, mixture temperature T, molar flow rates F_{N_2O}, F_{N_2}, F_{O_2}.
Respective inlet conditions are: p_0, T_0, $F_{N_2O_0}$, $F_{N_{2_0}}$ and $F_{O_{2_0}}$.
These are the unknowns of a system of three differential equations:

1. Momentum balance equation. It is used for the computation of pressure losses across the packed bed reactor: Ergun equations is employed for this purpose.

2. Molar balance equation. Molar flow rate for each of the species forming or disappearing along the reactor. It is directly coupled with the energy balance equation.

3. <u>Energy balance equation.</u> Output of this equation is the temperature profile along the reactor.

The resulting differential ODE problems is solved numerically with MATLAB ODE45 solver.
Results are reported in Chapter 4.

Momentum Balance Equation

Ergun equation was the correlation derived by chemical engineer S. Ergun in 1952 as an outcome of his experimental work with pressure losses across packed bed reactor. [55]
The equation, which cover the entire range of flow rates, entails both viscous and kinetic losses assumed to be summable:

$$\frac{dp}{dz} = -\left(\frac{150\mu w_s}{d_p^2} \frac{(1-\epsilon^2)}{\epsilon^3} + \frac{1.75\rho w_s^2}{d_p} \frac{1-\epsilon}{\epsilon^3} \right) \tag{3.11}$$

where the symbols used stand for:

- ρ - mixture density $\left[\dfrac{kg}{m^3} \right]$

- μ - mixture viscosity $[Pa\,s]$

- w_s - superficial velocity $\left[\dfrac{m}{s} \right]$

- d_p - single pellet diameter $[m]$

- $\epsilon = \dfrac{V_{void}}{V_{tot}}$ - void fraction $[-]$

The ratio between void volume inside the reactor V_{void} and the total internal volume of the reactor V_{tot} is defined as **void fraction** ϵ.
Depending on the pellets geometry chosen for catalyst support, void volume inside the catalyst change and so void fraction.

Foumeny and Benyahia [56] derived a generalized mean voidage correlation to predict mean voidage in packed bed of spherical particles:

$$\epsilon = 0.383 + 0.254\, d_r^{-0.923} \frac{1}{\sqrt{0.723\, d_r - 1}} \tag{3.12}$$

where d_r is the ratio between reactor internal diameter and pellet diameter:

$$d_r = \frac{d_{bed}}{d_p} \tag{3.13}$$

Radially void fraction can vary, leading to pressure fluctuations along the radius and potential concentration gradient in the same direction, invalidating the assumption of a plug flow reactor.
Chu and Ng studied a computer-based simulation of fluid through a packed bed. [57] They found out absence of radial concentration gradients for:

$$d_r > 8 \tag{3.14}$$

value for which the assumption of plug flow reactor is still reasonable.

It is important to point out that fluid characteristics, **density** ρ and **viscosity** μ, in the equation are the mixture ones, computed from a weighted average on species molar fractions:

$$y_{N_2O} = \frac{F_{N_2O}}{F_{tot}} \tag{3.15}$$

$$y_{N_2} = \frac{F_{N_2}}{F_{tot}} \tag{3.16}$$

$$y_{O_2} = \frac{F_{O_2}}{F_{tot}} \tag{3.17}$$

to get:

$$\rho = \rho_{N_2O} y_{N_2O} + \rho_{N_2} y_{N_2} + \rho_{O_2} y_{O_2} \tag{3.18}$$

$$\mu = \mu_{N_2O} y_{N_2O} + \mu_{N_2} y_{N_2} + \mu_{O_2} y_{O_2} \tag{3.19}$$

Clearly, pressure loss are even indirectly dependent from the decomposition profile along the reactor, since mixture is changing its properties.

Superficial Velocity w_s is a measure of the velocity of the fluid inside the catalyst internal section if the reactor would be empty. Simply defined as:

$$w_s = \frac{\dot{m}}{\rho A_{bed}} \tag{3.20}$$

It is influenced as well by the changing composition of the mixture along the axis.

Molar Balance and Energy Balance Equations

The two aforementioned equations are closely related each other and both are differential equation to be integrated along an infinitesimal volume dV, since they derive from a volumetric balance, illustrated in Figure 3.7 Molar balance equation maps
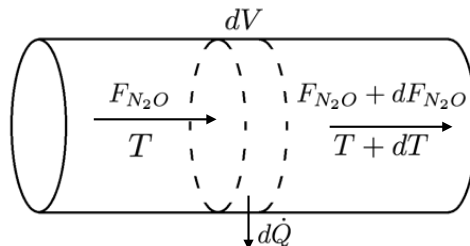
Figure 3.7: Infinitesimal Volume Balance in the Plug Flow Reactor Assumption

the evolution of species molar flow rates along the reactor, for the three species in questions:

$$\frac{dF_{N_2O}}{dV} = r \qquad \frac{dF_{N_2}}{dV} = -r \qquad \frac{dF_{O_2}}{dV} = -\frac{r}{2} \tag{3.21}$$

Molar flow rates are actually correlated with a stoichiometric algebraic equality:

$$F_{N_2O} - F_{N_2O}^0 = F_{N_2} - F_{N_2}^0 = 2\left(F_{O_2} - F_{O_2}^0\right) \tag{3.22}$$

As a result, only the molar balance equation for the consumption of N_2O will be exploited in the system of equations to be solved, since the reaction rate r is expressed as rate of N_2O decomposition.

Energy differential balance equation reads as follow:

$$\frac{dT}{dV} = \frac{-r\Delta H_r^{N_2O} + \frac{4U}{d_{bed}}(T_{ext} - T)}{F_{N_2O}c_{p_{N_2O}} + F_{N_2}c_{p_{N_2}} + F_{O_2}c_{p_{O_2}}} \tag{3.23}$$

where:

- r - overall reaction rate $\left[\dfrac{mol}{cm^3\,s}\right]$

- $\Delta H_r^{N_2O}$ - enthalpy of reaction $\left[\dfrac{J}{mol}\right]$

- U - overall heat transfer coefficient $\left[\dfrac{W}{m^2\,K}\right]$

- F_i - molar flow rate for specie i $\left[\dfrac{mol}{s}\right]$

- c_{p_i} - constant pressure specific heat for specie i $\left[\dfrac{J}{mol\,K}\right]$

- T_{ext} - External case (ambient) temperature $[K]$

Overall Reaction Rate

Catalytic rate constants for the chosen hexa-aluminate support are:

$$E_{a_c} = 122.173\,\frac{kJ}{mol} \qquad A_c = 7.09 \cdot 10^9\,\frac{g_{N_2O}}{atm_{N_2O}\,g_{cat}\,min} \tag{3.24}$$

For computation's sake, unit has to be converted to the SI system:

$$A_c = 7.09 \cdot 10^9 \cdot \frac{1}{60 \cdot 101325}\,\frac{g_{N_2O}}{Pa_{N_2O}\,g_{cat}\,s} \tag{3.25}$$

shifting from grams to moles by dividing for N_2O molecular weight $\left(44.0128\,\dfrac{g}{mol}\right)$:

$$A_c = 1.166 \cdot 10^3 \cdot \frac{1}{44.0128}\,\frac{mol_{N_2O}}{Pa_{N_2O}\,g_{cat}\,s} \tag{3.26}$$

Finally, conversion from catalyst mass to reactor void volume:

$$A_c = 24.492\,\frac{mol_{N_2O}}{Pa_{N_2O}\,g_{cat}\,s} \cdot \rho_{Hex} \cdot \frac{1-\epsilon}{\epsilon} = 1.525 \cdot 10^8\,\frac{mol_{N_2O}}{Pa_{N_2O}\,cm^3\,s} \tag{3.27}$$

As a consequence, reaction rate for catalytic reaction is:

$$r_c = A_c\,e^{-\frac{E_{a_c}}{R_u\,T}} = 1.525 \cdot 10^8\,e^{-\frac{122.173}{R_u\,T}}\,p_{N_2O}\,\left[\frac{mol_{N_2O}}{Pa_{N_2O}\,cm^3\,s}\right] \tag{3.28}$$

since catalytic reaction rate is directly dependent on N_2O partial pressure $p_{N_2O} = p\,y_{N_2O}$ (entailing the concentration value):

$$r_c = 1.525 \cdot 10^8\,e^{-\frac{122.173}{R_u\,T}}\,p_{tot}\,y_{N_2O}\,\left[\frac{mol_{N_2O}}{cm^3\,s}\right] \tag{3.29}$$

Similarly, for thermal decomposition of nitrous oxide, according to Atkins and Jones [39], rate constants are:

$$E_{a_t} = 250.00 \, \frac{kJ}{mol} \qquad A_t = 7.94 \cdot 10^{11} \, \frac{1}{s} \qquad (3.30)$$

The reaction rate for thermal decomposition is then:

$$r_t = A_t \, e^{-\dfrac{E_{a_t}}{R_u \, T}} = 7.94 \cdot 10^{11} \, e^{-\frac{250.00}{R_u \, T}} \, [N_2O] \quad \left[\frac{mol_{N_2O}}{cm^3 \, s} \right] \qquad (3.31)$$

and it is proportional to N_2O molar concentration $[N_2O]$.

As is shown in the work by Wickham et al [45], hexa-aluminate supports can withstand temperature up to $1000 \, °C$ without suffering a phase change.
Therefore, up to a temperature of $1200 \, K$ reaction rate is computed as the direct summation of catalytic and thermal decomposition rate:

$$r = r_c + r_t \qquad (3.32)$$

above that threshold, overall reaction rate is directly the thermal one:

$$r = r_t \qquad (3.33)$$

Case Layers Sizing

Thickness of the Hastelloy X case is sized accounting for an internal temperature of $1000 \, °C$, which is the interface temperature with YSZ insulation.
The latter has to be sized accordingly to have this temperature on its outer surface.
Treating the Hastelloy X case as a thin cylindrical shell, the sizing is performed with respect to the **hoop stress**: [58]

$$\sigma_h = \frac{p_{design}^{cat} d_{bed}}{2 t_{hx}} \qquad (3.34)$$

Reversing the formulation, thickness can be calculated:

$$t_{hx} = \frac{p_{design}^{cat} d_{bed}}{2 \sigma_y^{hx}} \qquad (3.35)$$

where σ_y^{hx} is the yield strength, p_{ch} and d_{ch} chamber pressure and diameter.

To size the insulation layer, a thermal energy balance between decomposing N_2O and YSZ hollow cylindrical layer is set:

$$\rho V_{void} \Delta H_r^{N_2O} = m_{ysz} c_{p_{ysz}} \Delta T \qquad (3.36)$$

where:

- N_2O enthalpy of reaction: $\Delta H_r^{N_2O}$

- YSZ mass: m_{YSZ}

- YSZ specific heat: $c_{p_{YSZ}}$

- Temperature difference: $\Delta T = T_{ad} - T_{ysz}$

- Mixture density at T_{ad}: ρ

Since insulation by means of Yttria-stabilized Zirconia coating is mostly adopted by aeronautic engine industries for turbine blade insulation, studies about YSZ layers are not so promoted. Collecting characteristic for this material could be difficult.
By the way, any uncertainty in the value reported will be addressed by the adoption of a large safety margin in the computation.
Wan et at [59] studied thermal diffusivity and specific heat for particular specimen of YSZ, their outcome was a specific heat of:

$$c_{p_{ysz}} = 630 \ \frac{J}{kgK} \qquad (3.37)$$

value recovered at a temperature of $1300 \, K$, but by the plot proposed in the work this value seems a good estimate even at higher temperature.
Density is even reported for different type of specimens analyzed in the work. The value adopted is:

$$\rho_{ysz} = 6.00 \ \frac{g}{cm^3} \qquad (3.38)$$

The same value can also be found in the CrysTec datasheet for ZrO_2 - YSZ. [60]
The energy balance can be rewritten to obtain a ready to use expression for the external radius of YSZ layer:

$$\rho \, \frac{\pi d_{bed}^2}{4} l_{bed} \, \Delta H_r^{N_2O} = \rho_{ysz} \, \pi \left(r_{ysz}^2 - \frac{d_{bed}^2}{4} \right) l_{bed} \, c_{p_{ysz}} \Delta T \qquad (3.39)$$

where d_{bed} is the inner catalyst diamater and r_{YSZ} is the outer radius of the YSZ layer.

The expression for the outer radius calculation is then:

$$r_{ysz} = \frac{d_{bed}}{2}\sqrt{1 + \frac{\rho}{\rho_{ysz}}\frac{\Delta H_r^{N_2O}}{c_{p_{ysz}}\Delta T}} \tag{3.40}$$

Thickness of the YSZ layer is easily computed as: $t_{ysz} = r_{ysz} - \dfrac{d_{bed}}{2}$.

Overall Heat Transfer Coefficient

Estimation of heat losses out of the catalyst is carried out by means of the overall heat transfer coefficient computation.

Heat has to flow out from the reactor passing across three layers, assumed as a series of three thermal resistances:

- Internal insulation YSZ layer.

  Thickness: t_{ysz}. Thermal conductivity: $\lambda_{ysz} = 1.5$ W/mK [60]

- Catalyst Hastelloy X case.

  Thickness: t_{hx}. Thermal conductivity: $\lambda_{hx} = 28$ W/mK [49]

- Still Atmospheric Air. Natural convection coefficient: $h_{air} = 2.26$ W/m²K. h_{air} has been computed from Nusselt correlations available in [61], defined specifically for natural convection of an horizontal cylinder.

The expression for the overall heat transfer coefficient, referred to the internal surface of the catalyst, is:

$$U = \frac{1}{\dfrac{d_{cc}}{2\lambda_{ysz}}\log\dfrac{d_{cc} + 2t_{ysz}}{d_{cc}} + \dfrac{d_{cc}}{2\lambda_{ysz}}\log\dfrac{d_{cc} + 2(t_{ysz} + t_{hx})}{d_{cc} + t_{ysz}} + \dfrac{1}{h_{air}}\dfrac{d_{cc} + 2(t_{ysz} + t_{hx})}{d_{cc}}} \tag{3.41}$$

3.3.4   Nozzle

Mathematical model of the converging-diverging nozzle consists in sizing the nozzle and assess its resulting main propulsive parameters.

All thermodynamic properties of the mixture (ρ, c_p, γ) are known from the catalyst simulation and mass flow rate $\dot{m}$ is computed from the tank discharge routine.

Nozzle discharges in optimal condition, so external pressure is the ambient one. Exit Mach number can be thus computed:

$$M_d = \sqrt{\frac{2}{\gamma - 1} \left[\left(\frac{p_{end}}{p_d} \right)^{\frac{\gamma-1}{\gamma}} - 1 \right]} \tag{3.42}$$

where specific heat ratio γ is the average, weighted on molar fractions, of the resulting mixture after decomposition $(y_{N_2} = 0.66)$, $(y_{O_2} = 0.33)$:

$$\gamma = y_{N_2} \gamma_{N_2} + y_{O_2} \gamma_{O_2} \tag{3.43}$$

Since the expansion is approximated as an isentropic one along the nozzle, temperature T_d and density ρ_d at the exit section of the nozzle can be computed, assuming still flow at the exit of the catalyst:

$$T_d = \frac{T_{end}}{1 + \frac{\gamma - 1}{2} M_d^2} \tag{3.44}$$

$$\rho_d = \frac{\rho_{end}}{\left[1 + \frac{\gamma - 1}{2} M_d^2 \right]^{\frac{1}{\gamma-1}}} \tag{3.45}$$

Two key propulsive parameters, characteristic velocity and thrust coefficient, can be calculated as follows:

$$c^* = \sqrt{\frac{RT_d}{\gamma} \left(\frac{\gamma + 1}{2} \right)^{\frac{\gamma+1}{\gamma-1}}} \tag{3.46}$$

$$C_T = \sqrt{\frac{2\gamma^2}{\gamma - 1} \left(\frac{2}{\gamma + 1} \right)^{\frac{\gamma+1}{\gamma-1}} \left[1 - \left(\frac{p_{end}}{p_d} \right)^{\frac{\gamma-1}{\gamma}} \right]} \tag{3.47}$$

where mixture constant R is the weighted average of specific constants of each gas in the mixture:

$$R = y_{N_2} R_{N_2} + y_{O_2} R_{O_2} \tag{3.48}$$

Finally, exit velocity v_{ex} and expansion ratio ϵ, computable as follows:

$$v_d = \sqrt{\frac{2\gamma}{\gamma - 1} RT_{end} \left[1 - \left(\frac{p_d}{p_{end}} \right)^{\frac{\gamma-1}{\gamma}} \right]} \qquad (3.49)$$

$$\epsilon_{ratio} = \frac{A_e}{A_t} = \frac{1}{M_d} \sqrt{\left[\frac{2}{\gamma + 1} \left(1 + \frac{\gamma - 1}{2} M_d^2 \right) \right]^{\frac{\gamma+1}{\gamma-1}}} \qquad (3.50)$$

As a result, specific impulse I_s and thrust T can be computed, since v_{ex} is equal to the effective discharge velocity:

$$I_s = \frac{v_d}{g_0} \qquad T = \dot{m} v_d \qquad (3.51)$$

Chapter 4

Analysis of the Results

4.1 Tank

Tank outflow simulation is presented in the following. Considering a 6 L tank, with exit nozzle diameter of 1.5 mm a single run of the code is used to compare results of the simulations performed with real or ideal gas assumptions, starting from the same global conditions: $P_{tank_0} = 30\ bar$ and $T_{tank_0} = 298.15\ K$.
It is important to note that simulation is prevented to go on whenever tank pressure falls below 5 bar. This is due to:

– Lack of physical meaning in testing catalytic decomposition at such low pressure.

– Prevention of possible back flow along the line, as suggested by [33], when discharging at atmospheric pressure (a large margin of safety is therefore applied).

– Numerical issues connected with interpolation function exploited for N_2O properties computation, as pointed out in Section 2.5

In Figure 4.1, 4.2 and 4.3 trends in time for pressure, temperature and mass flow rate are presented respectively.

Since the ideal adiabatic expansion is quite close to the real expansion at constant internal energy, the only pressure trend seems to be approximatively the same, but the estimations for temperature and mass flow rate are a clear indicator that ideality assumption is too far from reality conditions: in particular the temperature decrement is unreasonable looking at the experimental results of [33].
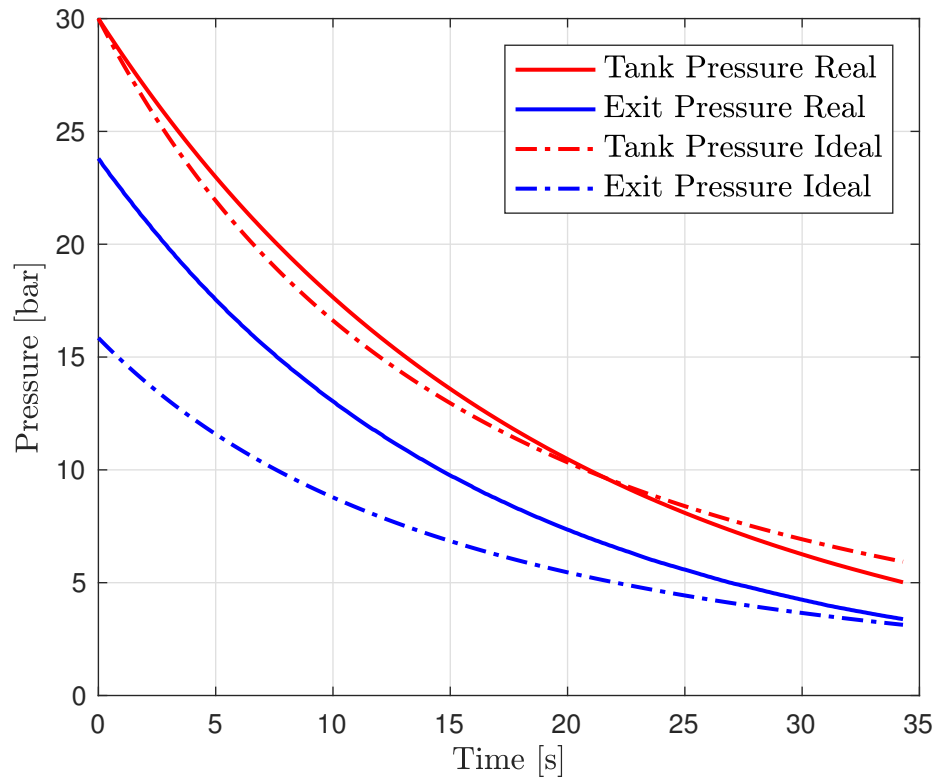
Figure 4.1: Ideal-Real Pressure Comparison

N_2O has to be considered a real gas during the outflow from tank and even further through the injector.

4.1.1 Tank & Injector Simulation

Pressure variation in time for tank ($V = 6\,\text{L}$, $p_{tank_0} = 30\,\text{bar}$, $T_{tank_0} = 25°\text{C}$) and injector are presented in Figure 4.4 in order to assess which is the pressure loss connected with the injection.

Injector actually represents a small head losses for the flow exiting the tank: at $t = 0\text{s}$ pressure loss due to injection amounts to 2.5% of the exit pressure ($p_{exit} = 23.8\,\text{bar}$ and $p_{inj} = 23.2\,\text{bar}$).

Such pressure loss is almost constant through all the discharge of the tank.
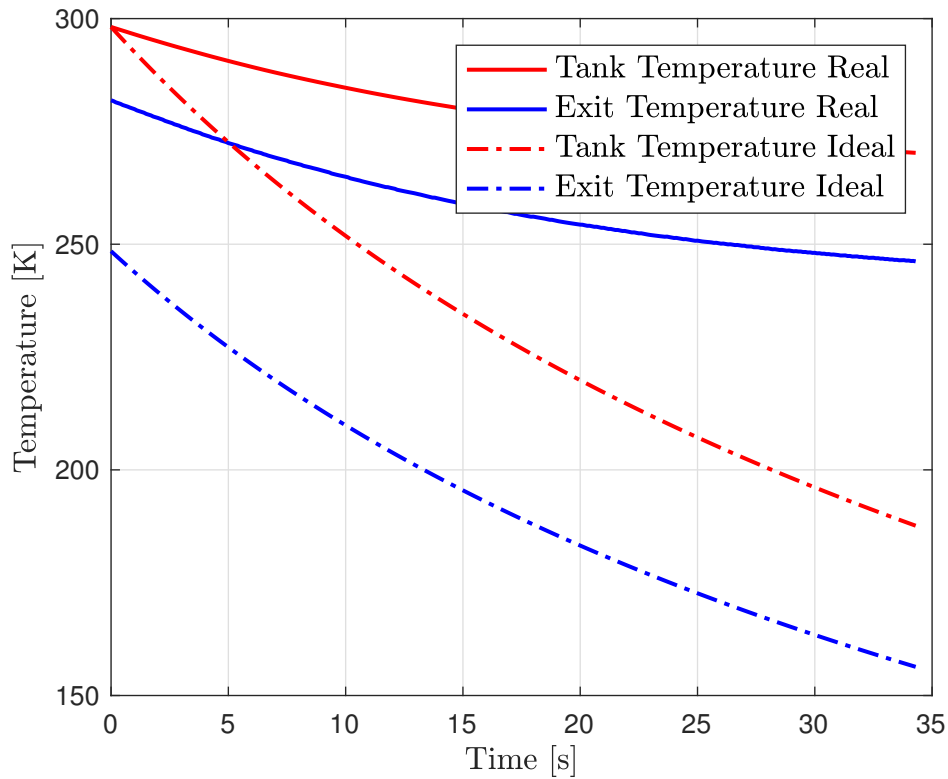
Figure 4.2: Ideal-Real Temperature Comparison

4.1.2   Parametric Simulation

Parametric simulations are performed in order to check consistence of the employed code: results are interpreted and explained even to justify possible design choices for the tank.

Parametric analysis is performed with respect to one among exit section diameter d_{exit}, total pressure p_{tank}, total temperature T_{tank} and tank volume V_{tank}.

Profile for Pressure, Temperature (for both of which solid line stands for tank property, while dashed line for exit property) and mass flow rate in time are presented.

In Figure 4.5 it can be clearly seen that exit diameter is critical for tank discharge dynamics, greatly affecting mass flow rate and discharge time. Numerical results are reported in Table 4.1.

An exit diameter of 1.5 mm has been selected in order to assure the best compro-
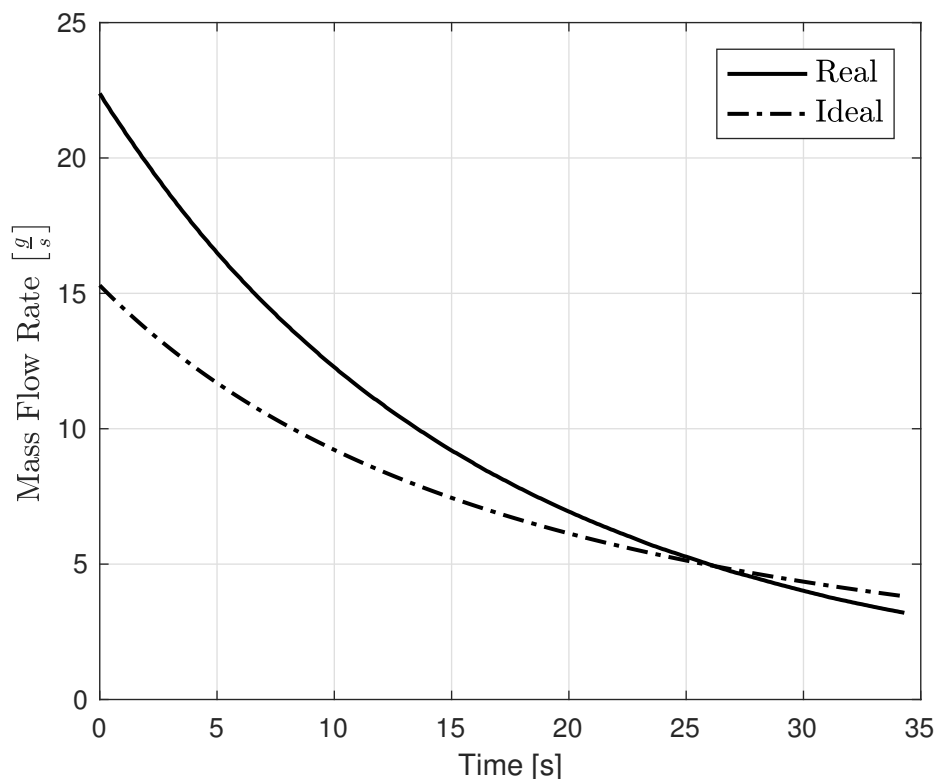
Figure 4.3: Ideal-Real Mass Flow Rate Comparison

mise in terms of consistent mass flow rate entering the catalyst to sustain a complete decomposition and a long enough emptying time, to allow for a reasonable residence time inside the catalyst. Both considerations are taken in lights of literature reviews [25], [31].

Figure 4.6 presents a parametric result with respect to starting tank pressure p_{tank}. The effect connected to an increase in tank pressure is recognized with a mass flow rate increment and a decreased final outgassing temperature (passing from a 30 to 40 bar as p_{tank_0}, N_2O reaches respectively 246 and 231 K).
p_{tank_0} has been set at 30 bar for two reasons:

– An higher pressure would be dangerously close to N_2O critical point, at ambient temperature. As a consequence, storage temperature oscillation will not therefore affect nitrous oxide.

– The increment in mass flow rate, connected with increased storage pressure, is
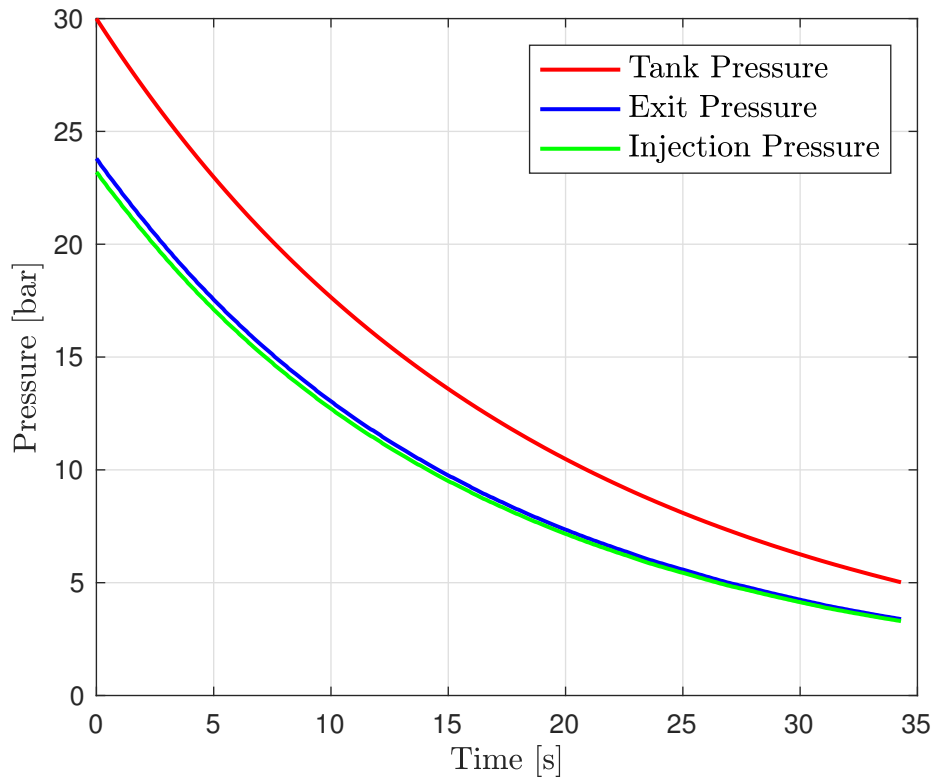
Figure 4.4: Tank & Injector Simulation

as well connected with a lower discharge temperature. This asks for a more efficient pre-heating system.

While Figure 4.7 shows that starting tank temperature T_0 has very little effect on tank outflow dynamics (308.15 K is selected as upper boundary, very close to the critical point temperature, 309.52 K), Figure 4.8 proves that a volume increment affects only the time duration of the discharge phenomenon in a non linear way.

As a matter of facts, a 2 L tank volume empties in more than twice the time of a 1 L tank (11.3 s with respect to 5.4 s). On the wake of this considerations, in order to extend the experiment to 34.2 s, a 6 L tank is selected and sized, as reported in Section 4.1.3.
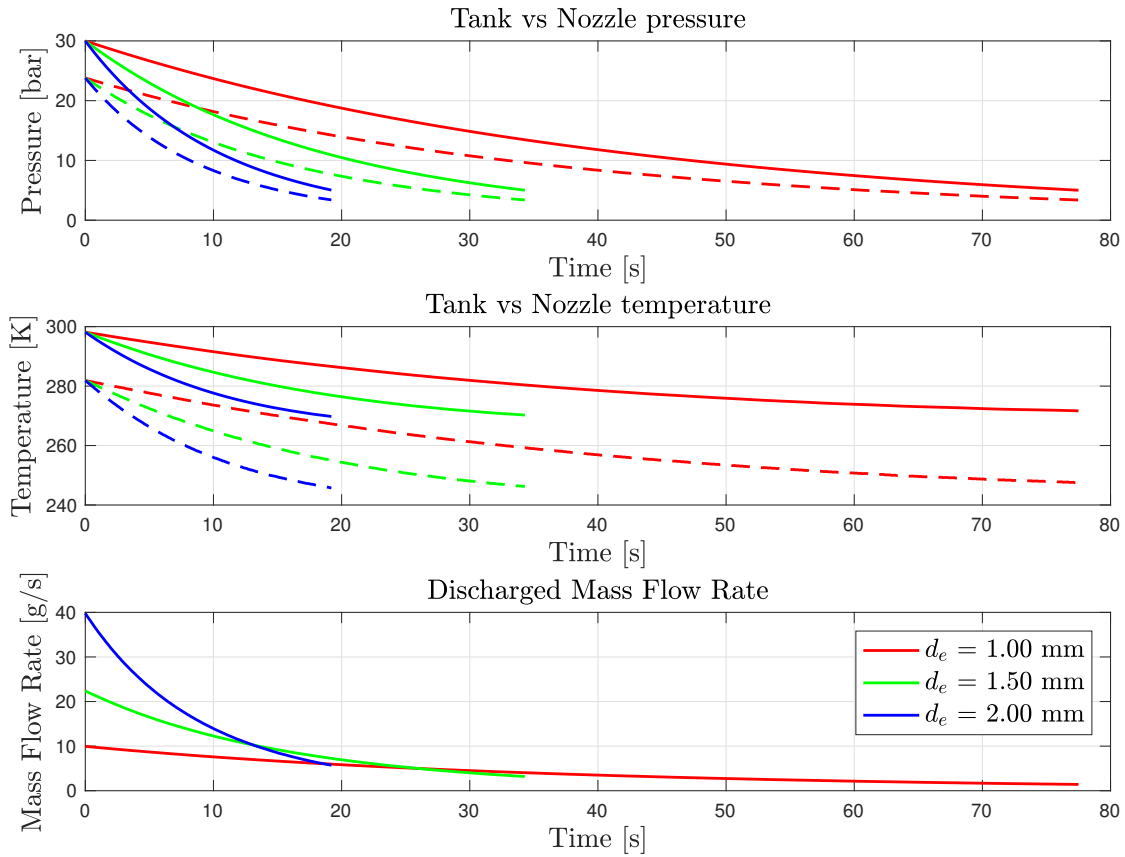
Figure 4.5: Results for Different Exit Diameters

4.1.3 Tank Sizing Results

Tank sizing aims at selecting the best geometry and therefore the ullage volume for storage.

A 1 L spherical tank is 12.4 cm in diameter, which is comparable with the system dimension scale of [25]. A similar 2 L sphere would size 15.6 cm in diameter, while a 3 L one 18 cm.

Considering the long discharge time for a 6 L tank, the problem of large space occupied can be easily managed with the alternative geometry proposed in Section 3.3.1 and illustrated in Figure 4.9: putting a 12-cm-long cylinder in between the two hemispheres of 18 cm in diameter, a compact 6 L tank is obtained.

Sizing an aluminum tank ($\sigma_y^{Al} = 278$ MPa, $r_{tank} = 8.945$ cm) at 50 bar with re-

d_{exit} [mm]	Emptying Time [s]	Start - End $\dot{m}$ [g/s]
1.0	12.8	10 - 2.5
1.5	5.6	22.4 - 3.3
2.0	3.1	39.8 - 5.8
2.5	1.9	62.2 - 9.4

Table 4.1: Results for Different Exit Diameters
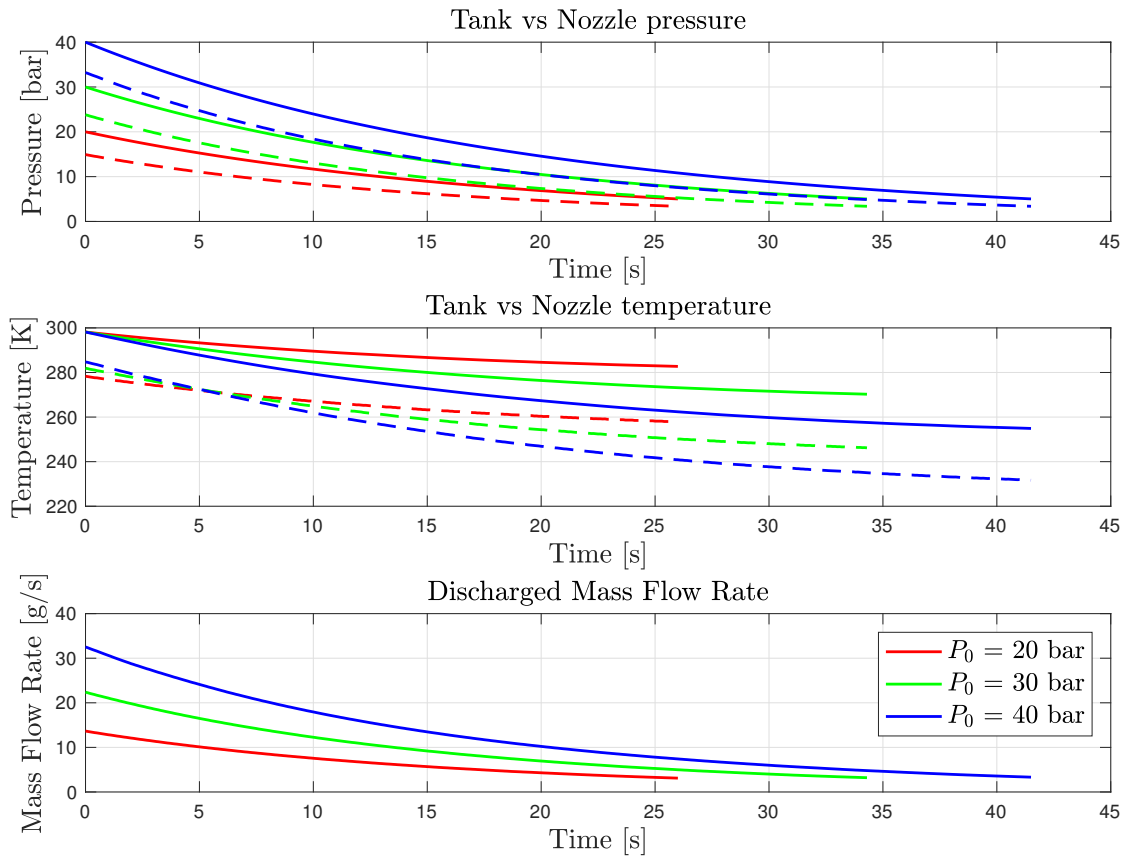
Figure 4.6: Results for Different Initial Tank Pressure

spect to the hoop stress in the cylindrical part of the tank, the results is:

$$th_{tank} = \frac{p_{design}^{tank}\, r_{tank}}{\sigma_y^{Al}} = 1.1 \cdot 10^{-3} \text{ m} = 1.1 \text{ mm} \qquad (4.1)$$
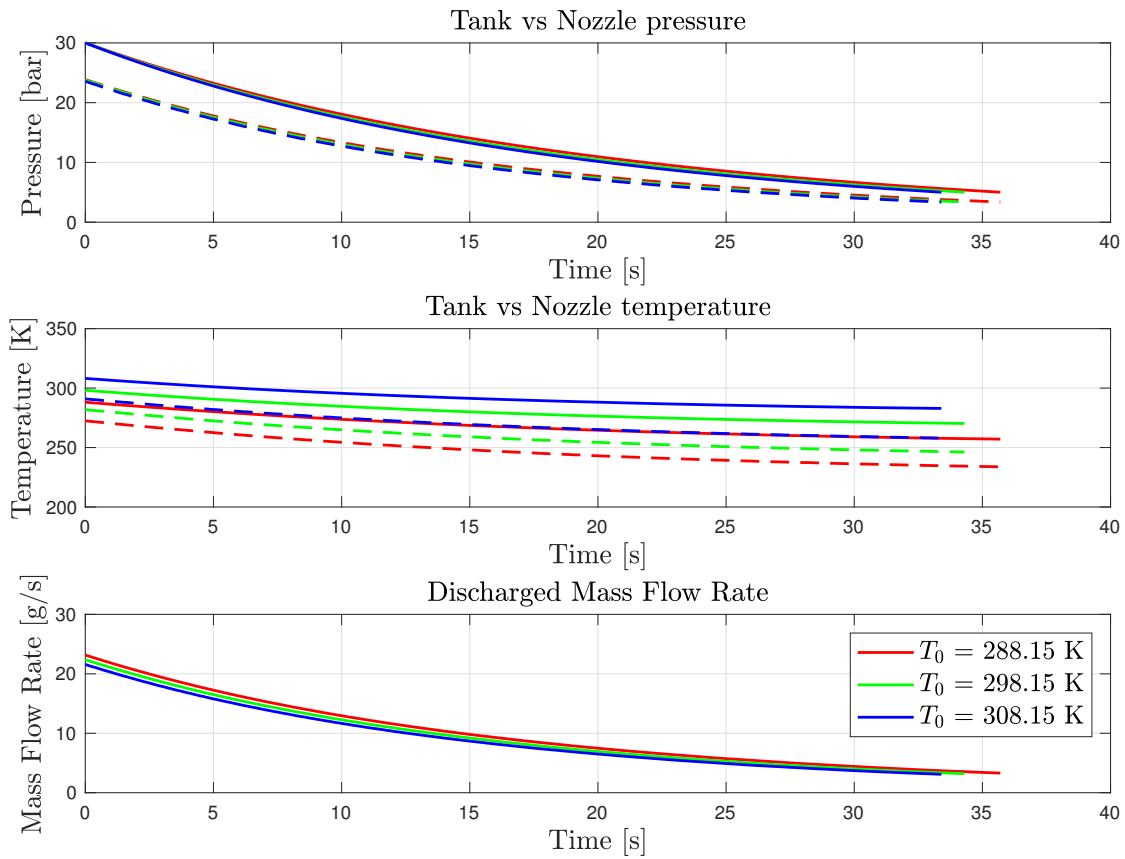
Figure 4.7: Results for Different Initial Tank Temperature

Aluminum thickness for the tank is set at 3 mm, an enlargement of 63 % with respect to the theoretical value for safety reasons.
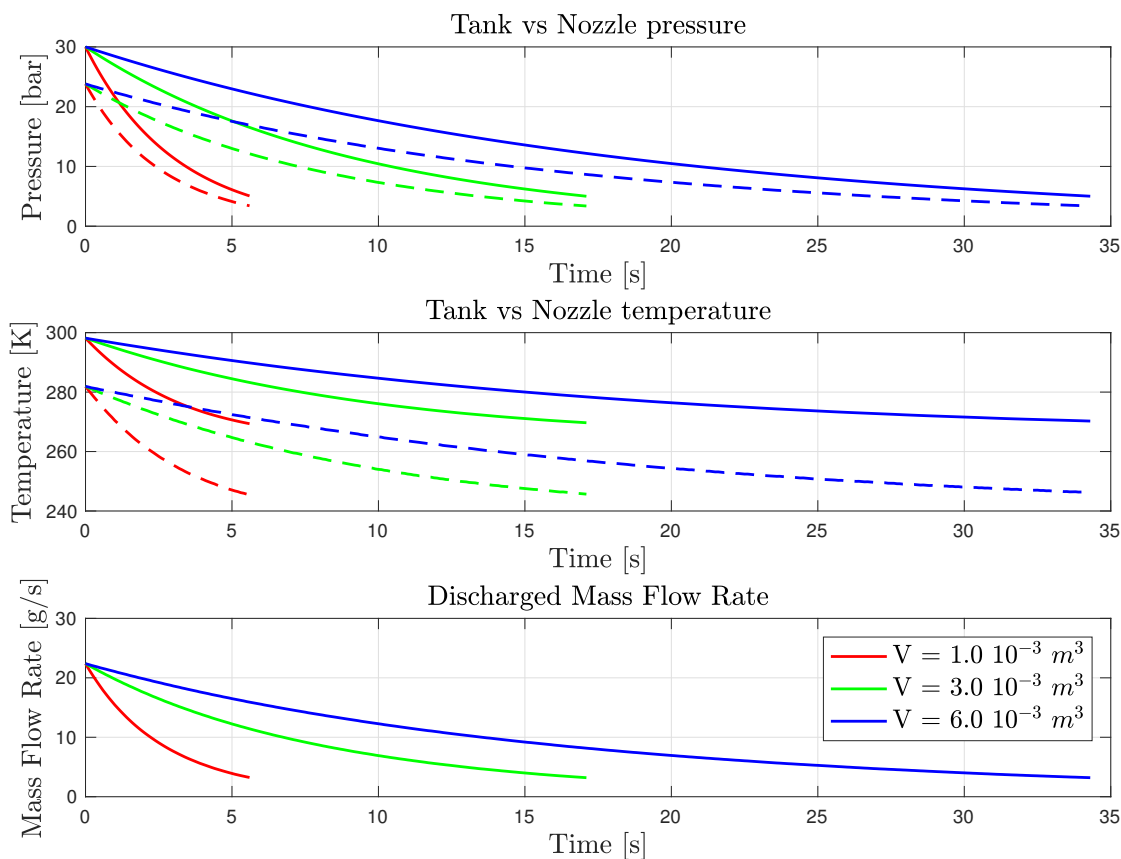
Figure 4.8: Results for Different Tank Volume

4.2 Catalyst

Results of the simulation of N_2O decomposition inside the catalyst are presented in Figure 4.10. For all the catalyst-related results presented inside this Section, the three most important parameters to map mixture evolution along the catalyst are presented: p, T and molar fractions y_{N_2O}, y_{N_2} and y_{O_2}. For the simulation case reported in Figure 4.10, and in general as a standard set of conditions, input properties are:

– $p_0 = 20$ bar, according to the research for similar-class hydrazine rocket, presented in Chapter 1.

– $T_0 = 550$ K, in order to have a fast enough decomposition reaction to be com-
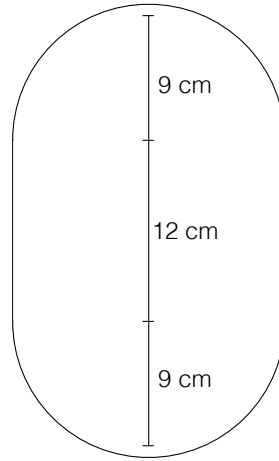
Figure 4.9: Scheme of the Selected Tank Geometry with Dimensions

pleted inside a reasonable long catalyst.
From the literature evidences, ([23], [25]) the catalyst should not exceed a length of 5 cm. Therefore the selected starting temperature is the lower threshold to speed up decomposition along a catalyst of the such a length.

– $\dot{m} = 25$ g/s, reasonable value according to the similar-class hydrazine rocket of Chapter 1.

While other important design parameters, for the standard simulation case are:

– A catalytic bed diameter of 3.5 cm is selected, according again to [23], [25].

– Recalling what has been presented in Section 3.3.3 from [57], in order to contain at the maximum properties variation in radial direction, a diameter ratio of 10 is selected, resulting in a 3.5 mm diameter pellet employed as catalytic support.

– Void fraction, computed with the formula in Equation 3.12, is $\epsilon = 0.3952$.

– In order to guess which is the Hastelloy X layer thickness required to sustain stress due to internal pressure, Equation 3.35 is employed to size the catalyst case. Sizing is performed at a limit temperature of 1273 K (1000 °C) at which yield stress for Hastelloy X is estimated in about $\sigma_y^{hx} = 43$ MPa ([49]), with a margined catalyst pressure of $p_{design}^{cat} = 30$ bar.
With a catalyst 3.5 cm in diameter, the thickness needed to sustain such thermomechanical loads is results to be 1.22 mm.
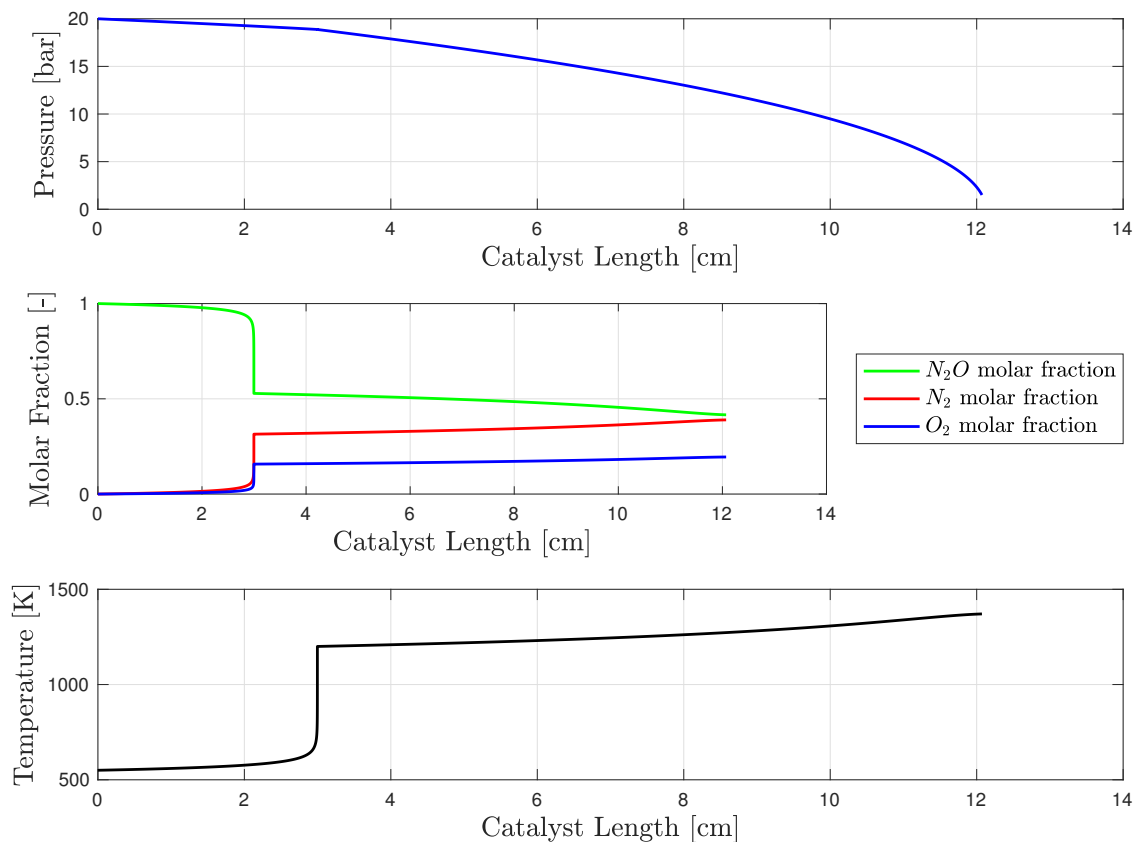
Figure 4.10: N_2O Decomposition Profile along a 20-cm-long Catalyst

The selected thickness for the catalyst case has been widely margined reaching the value of $th_{hx} = 3$ mm, which is capable of sustaining hoop stresses due to internal pressure up to 74cbar in the same conditions explained previously.

– Insulation YSZ layer is sized as well in the worst-case condition possible of a maximum theoretical internal temperature ($T_{ad} = 1932.5$ K with $T_0 = 550$ K and $p_0 = 20$ bar). Thickness of the YSZ insulation layer needed to protect the metallic case down to a temperature of 1273 K is computed with Equation 3.40. A 0.09-mm-thick layer is sufficient to accomplish that insulation, thanks to YSZ outstanding insulation properties, but layer thickness $th_{YSZ} = 0.25$ mm is adopted to account for uncertainties in YSZ properties.

An overlook of the most important parameter for the catalyst design are reported in Table 4.2. The results shown in Figure 4.10 can be used to introduce some peculiar

p_{cat}	T_{cat}	$\dot{m}$	d_{bed}	d_p	ϵ	T_{sw}
20 bar	550 K	25 g/s	3.5 cm	3.5 mm	0.3956	1200 K

Table 4.2: Parameters for the Catalyst Model

considerations on the catalyst model exploited in this thesis:

– The most notable feature of the presented trends consists in a sharp slope discontinuity at 1200 K, representing the very first attempt to simulate the shift from catalytic to thermal decomposition, as predicted from [46], due to a solid phase change in the supports material (hexa-aluminate) which leads to a reduction in surface area and therefore in a reduced exposition of the active phase deposited on the support (events predicted to occur in around $1200 - 1300$ K).
Since no numerical model is available in the literature to predict how this shift in decomposition happen, this phenomenon is simply simulated leading to zero the catalytic reaction rate: the slope discontinuity is therefore explicable with the huge difference, two orders of magnitude, in decomposition rate.

– Just for this case, simulation runs up to a fictitious 20 cm length in order to show another important fact.
Once the decomposition is over ($y_{N_2O} = 0$) and temperature has reached its maximum value the mixture of N_2 and O_2 starts flowing without further reactions along the catalyst: this gives the chance to point out some important considerations.
Pressure starts dropping steadily (4.2 bar pressure loss is experienced in the non-reacting portion of the catalyst, while it is just limited to 0.34 bar on the reactive portion), reason for which is fundamental to select the proper pattern of input properties for N_2O in the catalyst in order to have a decomposition that ends near the end of the catalytic bed.
On the other end temperature is almost steady along the catalyst (only 63 K temperature decrement) which is explicable with the presence of the YSZ insulation layer needed to protect the external metallic case.
For this reason, temperature drop is not a big point of concern in the eventuality that decomposition ends short from the catalyst end.

– Temperature at the end of the decomposition reaches the value of $T_{end} = 2233.08$ K, which is different of 6.5 % from the predicted value with NASA

CEA code, as presented in Section 2.4. Error now is even larger than the 3.1 % error for $p_0 = 20$ bar and $T_0 = 550$ K, as reported in Section 2.5.2.

This can be explained recalling a concept explained in Section 2.5.2: from the procedure followed to create interpolation functions usable inside the plug flow reactor simulator, it has already been shown that $c_{p_{N_2O}}$ data are considered as the one mostly affected by numerical approximation errors (due to Shomate equations).

This greatly reflects on the result of the plug flow reactor simulation since, differently from the theoretical T_{ad} estimation for which c_p values of only N_2 and O_2 are used, in the plug flow reactor model also $c_{p_{N_2O}}$ values are used, as shown in Section 3.3.3.

A complete parametric study will be presented in the following with the intention to show variability of simulation results with respect to initial thermodynamic properties, geometry of the catalyst and model characteristics.

Stopping Criteria

Simulations will always be stopped whenever N_2O molar fraction reaches zero (i.e. when decomposition is complete), reporting which is the position, along catalyst axis, where N_2O is completely dissociated.

Another abort condition for the simulation consists in a sharp pressure loss of the mixture, symptomatic of a non-reacting mixture that quickly lose pressure: minimum pressure the mixture can reach is 1.5 bar, below that value simulation is stopped.

4.2.1   Parametric Simulations

Parameter: p_0

Figure 4.11 shows a parametric study with respect to a variable inlet pressure p_0. The outcome of the simulations reveals that pressure has a non negligible effects on reaction kinetics. This is expected since pressure directly influences the catalytic reaction rate but also affects indirectly the simulation through the properties of the gas composing the mixture.

Higher initial pressure also corresponds to a low head loss through the packed bed. For $p_0 = 5$ bar and $p_0 = 7$ bar gas flow is low energetic and therefore head loss are prominent, leading simulation to be stopped since pressure reaches 1.5 bar.
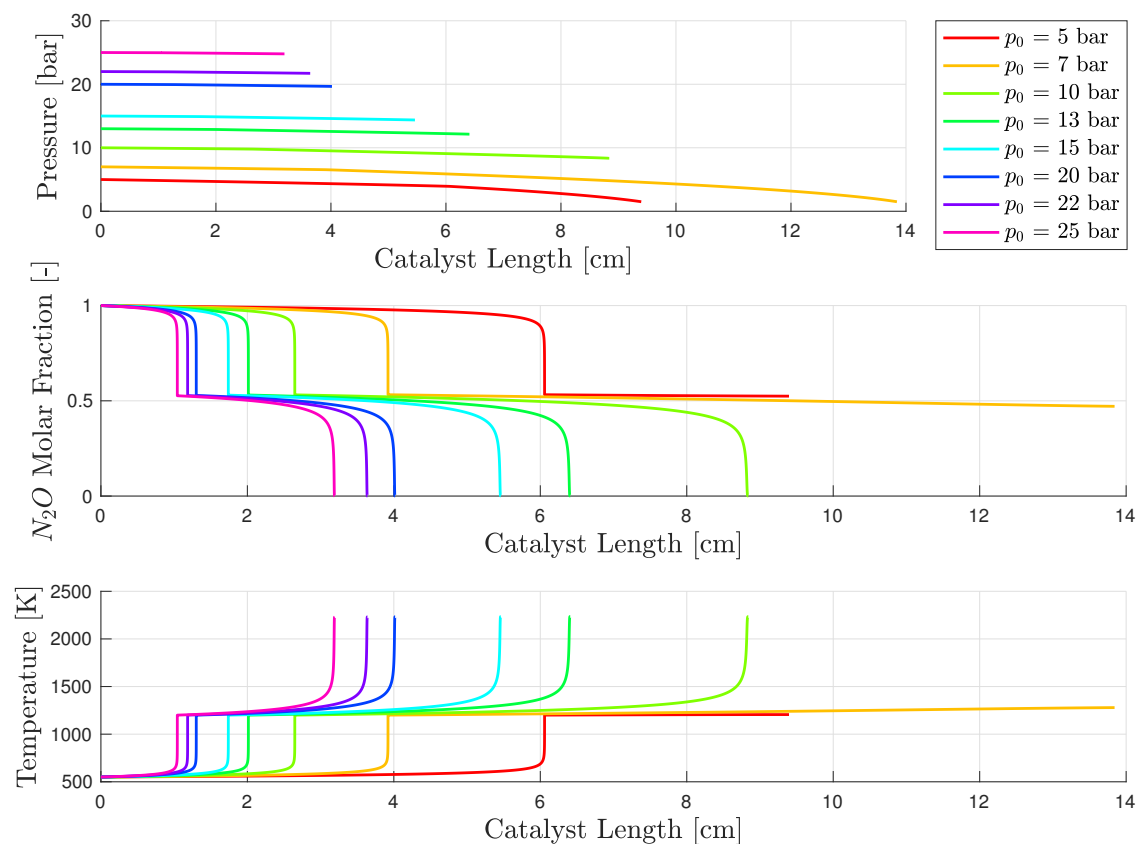
Figure 4.11: Pressure Parameterization

Parameter: T_0

Figure 4.12 reports the parametric study based on input temperature increment starting from $T_0 = 500$ K. Table 4.3 summarizes briefly the results of the simulation, comparing final temperature estimated against temperature estimation from the CEA code. Several important consideration can be pointed out looking at these results and will be listed afterwards.

– Trivially, a higher T_0 means a faster decomposition, in both its catalytic and thermal sector, with an increment in decomposition enthalpy and therefore in final decomposition temperature, as reported in Figure 4.12.

– From the aforementioned results table, it is clear that the error in the estimation of the complete decomposition temperature increase with increasing

temperature, a peculiarity already presented in Section 2.5.2. Error is now even larger then the one presented in Section 2.5.2 since in plug flow reactor model, $c_{p_{N_2O}}$ values are also employed. The reasoning is the same presented early in the current section.

– Catalytic decomposition proceeds faster with increasing T_0: at 700 K catalytic reaction ends in a 0.8 % length of the needed one for the standard case ($T_0 = 550$ K).
Since increasing inlet temperature corresponds to a higher enthalpy of decomposition, even thermal decomposition proceeds faster than in the standard case (slope is slightly greater with increasing T_0).
Looking at the N_2O molar fraction profile some interesting facts can be pointed out: for $T_0 = 700$ K, y_{N_2O} at the switch condition is 20 % smaller than the standard case. This is explicable noting two counteracting trends: a higher initial temperature speed up the decomposition but the quickness of the mixture to get to the switch temperature leaves reduced space for the mixture to decompose.

T_0 [K]	T_{end} [K]	T_{CEA} [K]	Error %
550	2233	2094	6.6
600	2314	2134	8.4
650	2400	2174	10.1
700	2481	2216	11.9

Table 4.3: Temperature Parameterization Results

Parameter: $\dot{m}$

Figure 4.13 presents a parametric simulation with respect to $\dot{m}$. As it is clear, the more mass enters the catalyst, the slower the reaction is and also the larger are head losses: passing from 5 g/s to 30 g/s, global head losses grows from 0.005 bar to 0.6 bar and position of complete decomposition from 0.8 cm to 4.85 cm.
Temperature at complete decomposition is the same for all the conditions, equal to the value of the standard case. (2233.05 K).
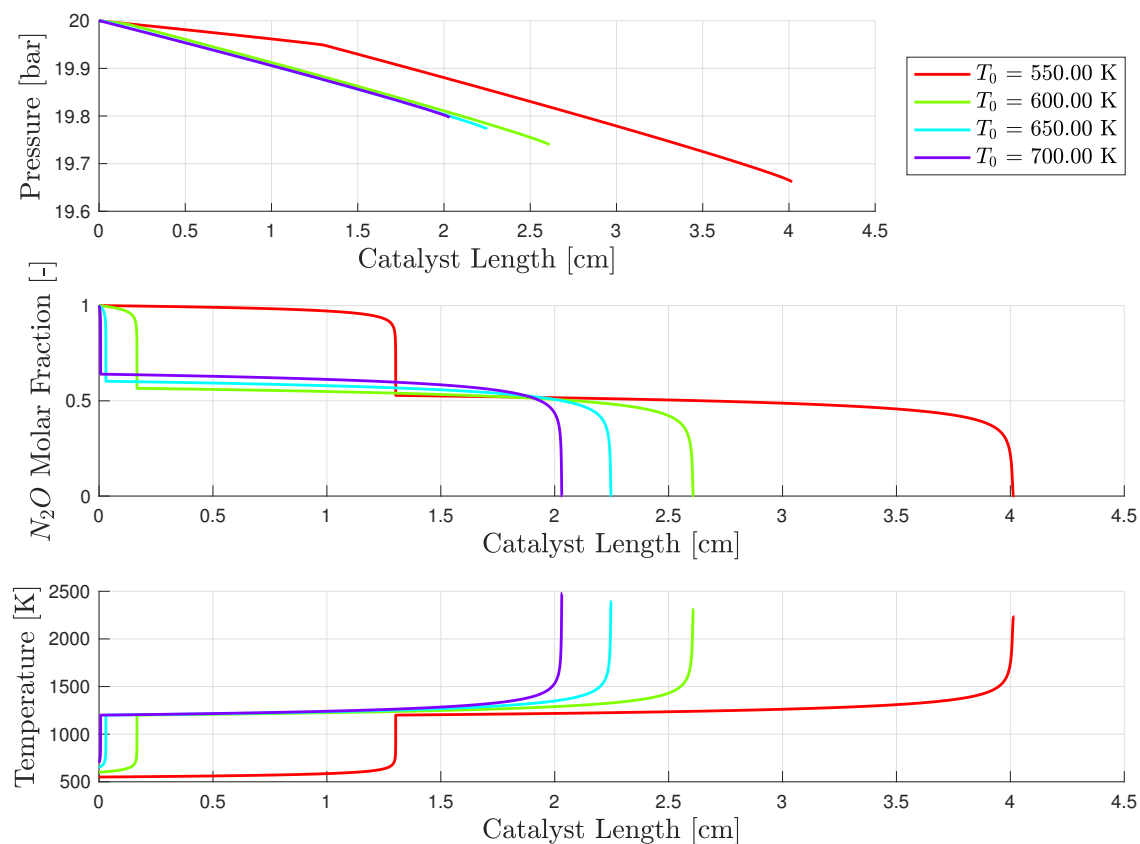
Figure 4.12: Temperature Parameterization

Parameter: d_{bed}

Figure 4.14 presents a successive scaling up of the bed diameter. As for mass flow rate analysis, no qualitative modification of the global shape of the curves is present. An increment in the bed diameter (from 2 to 5 cm) translates in smaller pressure loss (from 5 to 0.02 bar) since the larger the catalyst bed cross section, the smaller the superficial velocity.

Considering a constant diameter ratio $d_r = 10$, void fraction ϵ is unchanged and so it can be excluded as one of the reasons of reduced pressure loss.

With increasing bed diameter, length of complete decomposition gradually shrinks (from 10.3 to 1.4 cm) since superficial velocity reduces and therefore decomposition can complete early on in the catalyst.
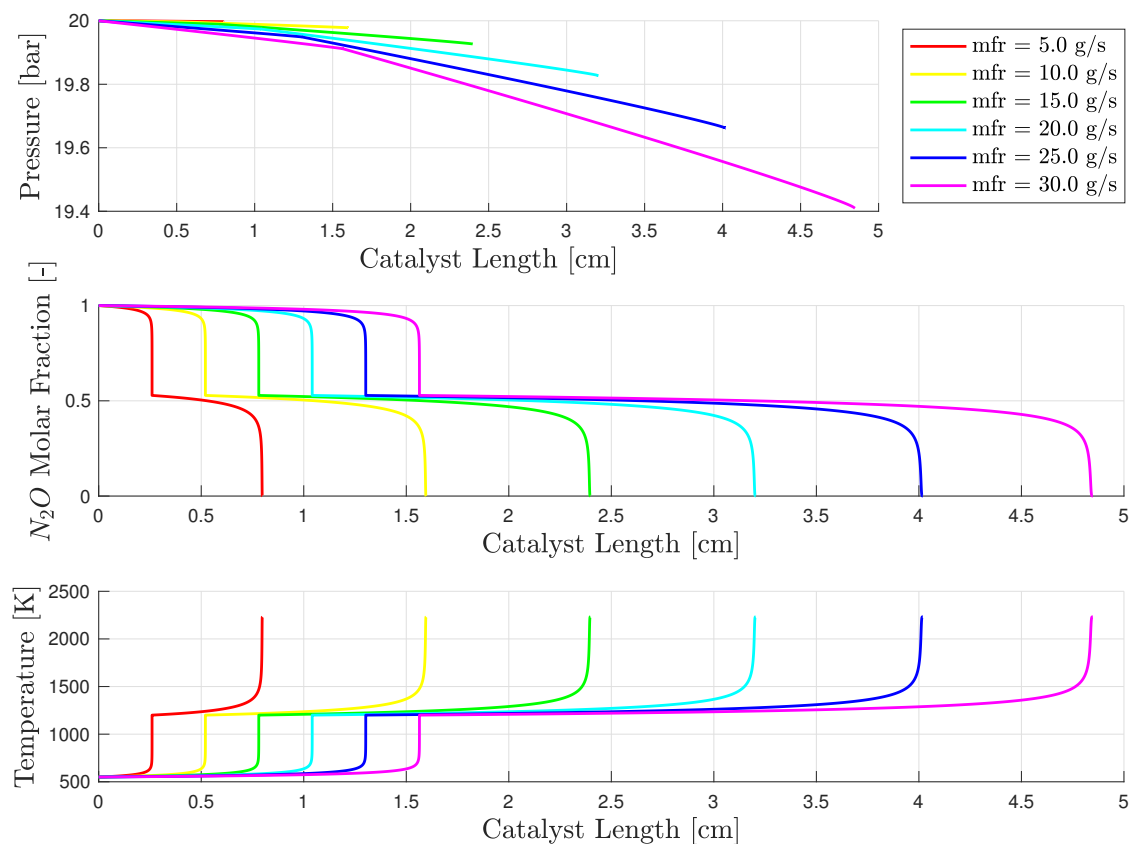
Figure 4.13: Mass Flow Rate Parameterization

Parameter: d_r

Figure 4.15 shows a parameterization with respect to diameter ratio d_r closely connected with void fraction ϵ (Equation 3.12): $d_r = 8$, 10, 12 corresponds respectively to $\epsilon = 0.4$, 0.3952, 0.3923.
Pure void fraction variations have effects only on pressure loss in the catalyst, though it is reduced (for $d_r = 8$ $\Delta P = 0.25$ bar while for $d_r = 12$ $\Delta P = 0.3$ bar).
No variation in distance or temperature of complete decomposition is observed.

Parameters: A_c, A_t, E_{a_c}, E_{a_t}

Figures 4.16, 4.17, 4.18 and 4.19 present studies aimed at testing simulator robustness to ariability of catalytic and thermal kinetic parameters (pre-exponential constant and activation energy).
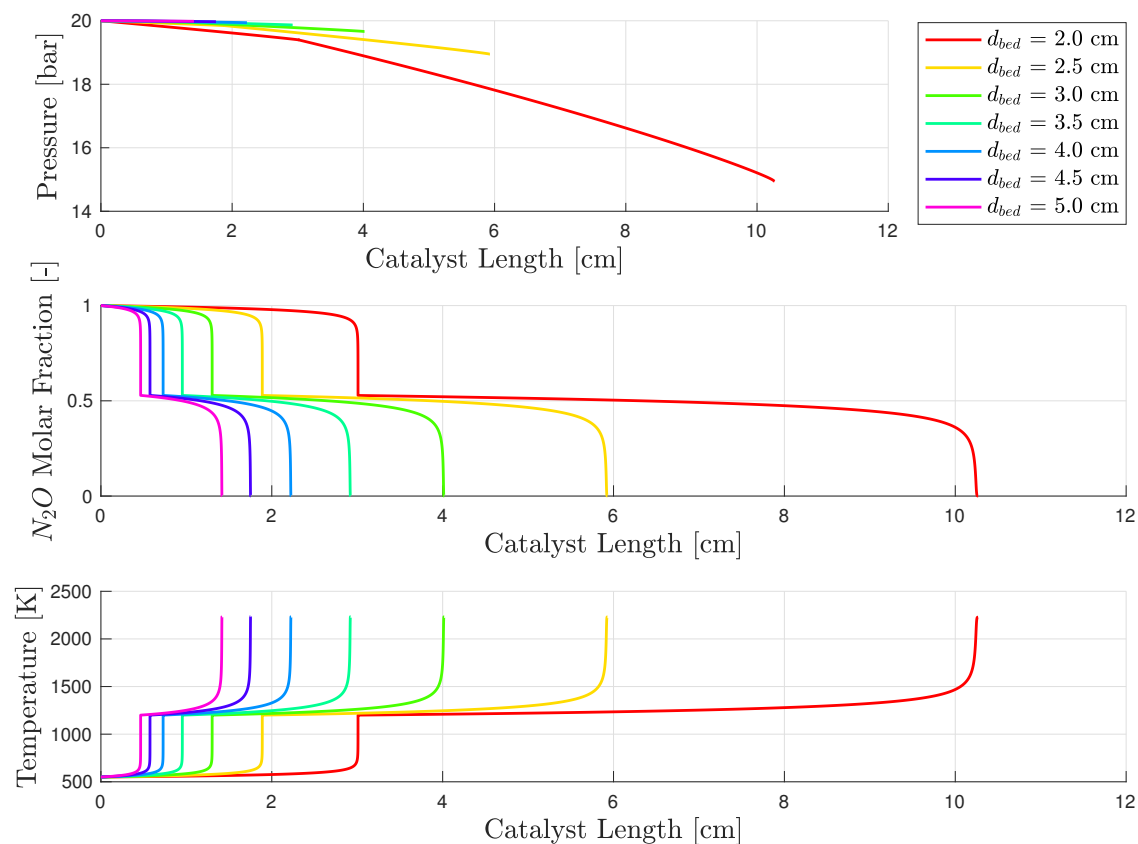
Figure 4.14: Bed Diameter Parameterization

For what concerns variation in pre-exponential constants, larger pre-exponential constants imply a faster reaction and this is clearly observable in Figures 4.16 and 4.17. Variability in A_c between $1.075 \cdot 10^8$ and $1.935 \cdot 10^8$ translates in practically no variation in complete decomposition temperature (5 K) while the location of the complete decomposition point oscillates from 3.7 and 5 cm. The same result, in terms of complete decomposition point, is obtained with oscillation of A_t between $6 \cdot 10^{11}$ and $9 \cdot 10^{11}$, without any practical variation in decomposition temperature (5 K). For too low value of both A_c and A_t, reaction is not completed along a 20 cm catalyst.

Passing now to activation energy values, similarly to what has been said for the pre-exponential constants, the smaller the activation energy the faster the reaction, catalytic or thermal. Differently from before, simulations are very sensitive to variation in the 10% order, while for pre-exponentials variations are in the order of $80 - 85\%$.
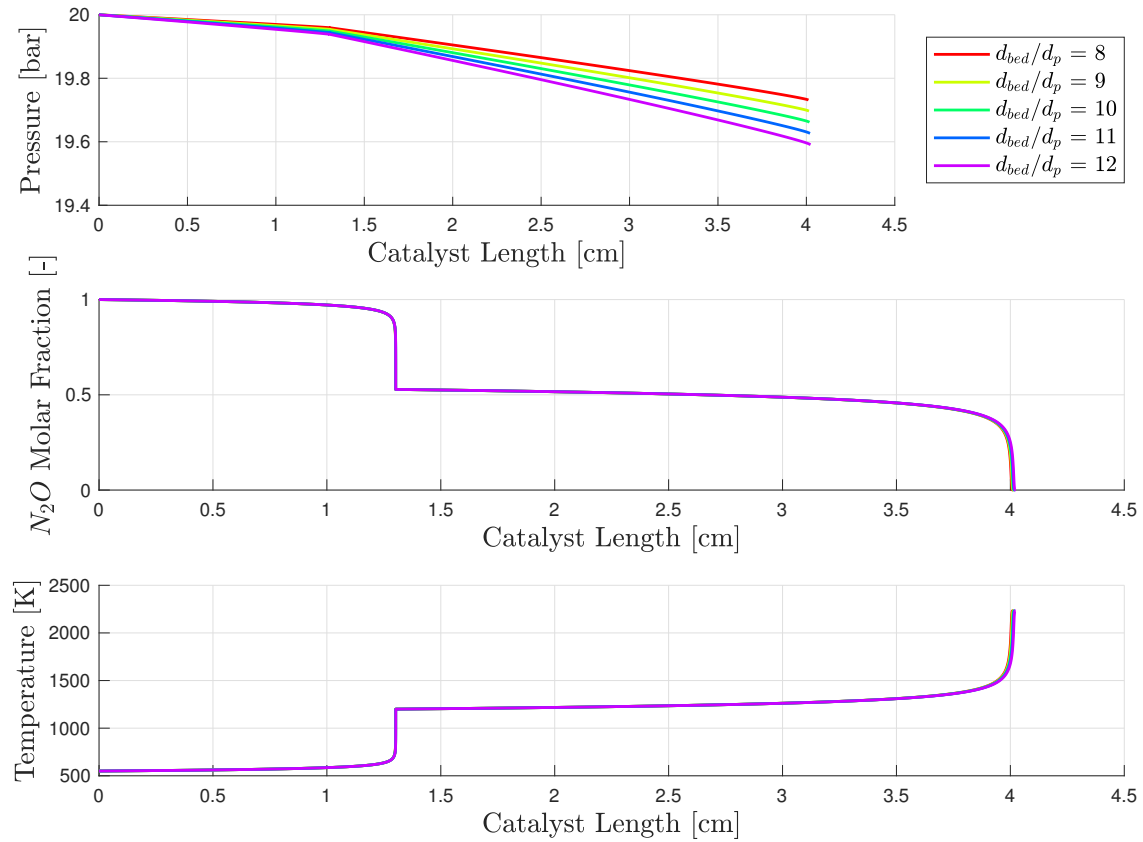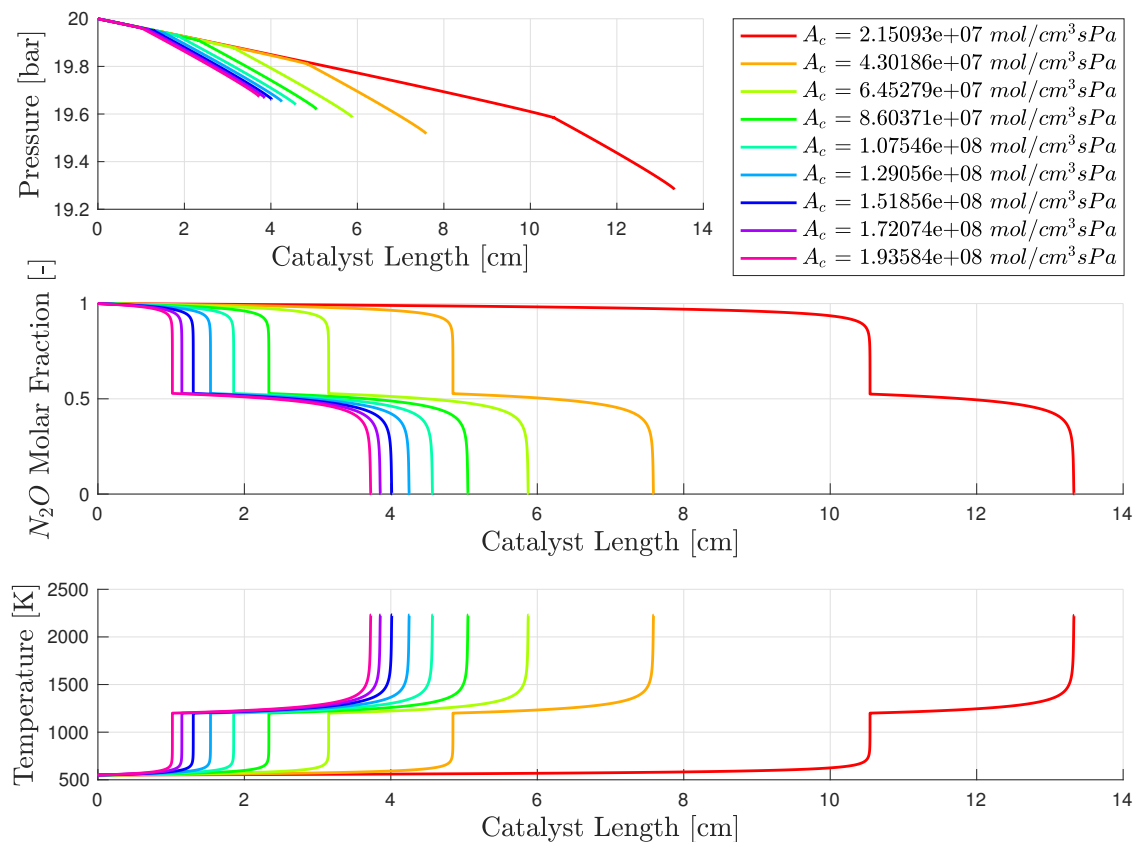
Figure 4.15: d_r Parameterization

4.3 Analysis of Catalytic-Thermal Decomposition Switch

One of the biggest point of concern in the simulation of the catalytic behavior is represented, as already mentioned, by the shift from catalytic to thermal decomposition.

No mathematical model can be employed to predict correctly where and how extended the shift region will be (remembering that during the whole temperature span, $550 - 2233$ K, catalytic decomposition is always faster than thermal decomposition, for the model employed here). The intention of this Section is to test code sensitivity to different mathematical simulation of the shift phenomenon.

Figure 4.20 shows how a variation of the switch temperature affects the outcome
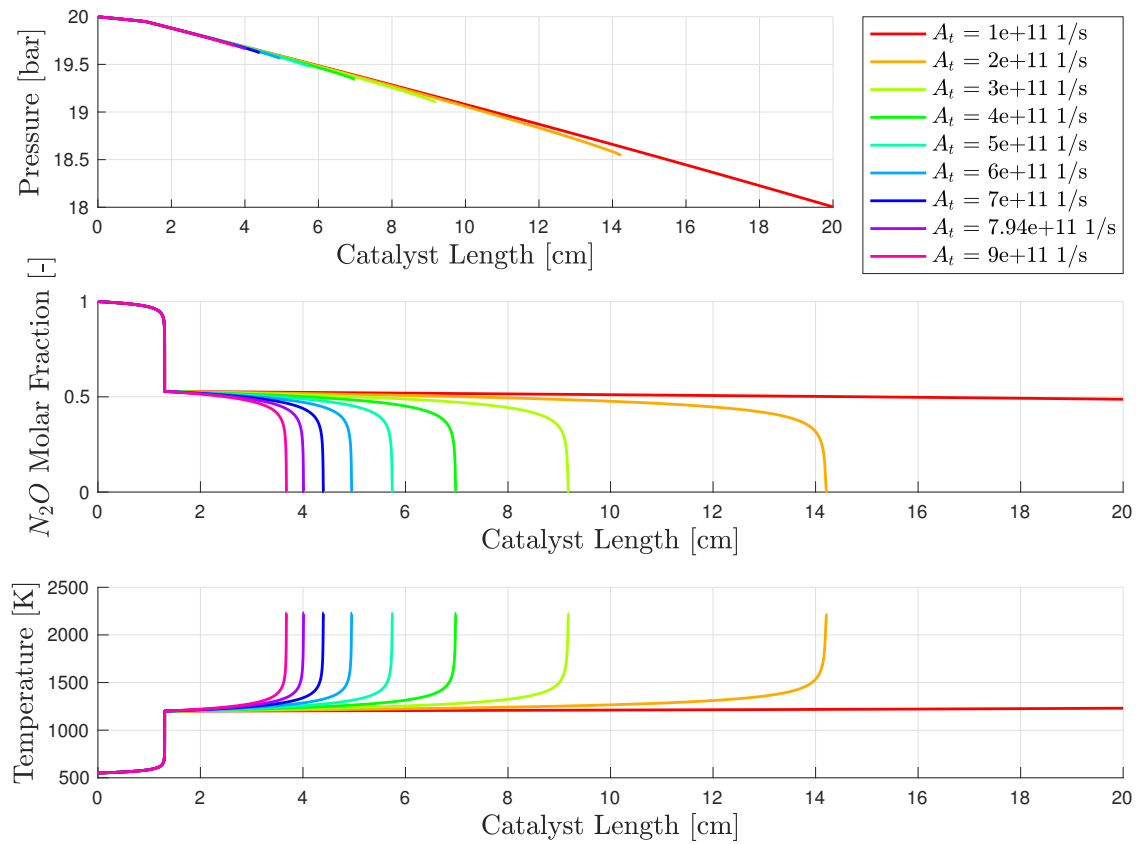
Figure 4.16: A_c Parameterization

of the simulation. Indeed the selected switch temperature of 1200 K is the lower boundary to have a complete N_2O decomposition in within a 20 cm catalyst, since with a $T_{sw} = 1100$ K decomposition is not completed.

Thermal reaction proceeds faster if switch condition is supposed at a higher temperature. For $T_{sw} = 1400$ K reaction ends just 1.5 mm after the switch from catalytic to thermal.

What is instead really important to note is that, changes in the switch temperature do not alter consistently the final decomposition temperature: for $T_{sw} = 1500$ K, T_{end} is just 5 K larger than the standard case (2238 K) meaning that switch temperature selection does not contributes to the T_{end} estimation error.

Figure 4.21 presents, together with Figure 4.22, an attempt to simulate a progres-

Figure 4.17: A_t Parameterization

sive switch from catalytic to thermal decomposition. Centering the switch interval around 1200 K, Figure 4.21 shows how the simulation changes with a catalytic losing effectiveness at lower temperature, while Figure 4.22 proposes results for the opposite case, catalyst is supposed to start losing effectiveness at 1200 K.

The sooner the catalyst lose its effectiveness the longer will take for a complete thermal decomposition, while on the other way round the longer the hexa-aluminate phase will survive at high temperature, the shorter will be the thermal decomposition.

Still it is interesting to note that, with different solution to the reaction switching problem, final decomposition temperature is unaltered.
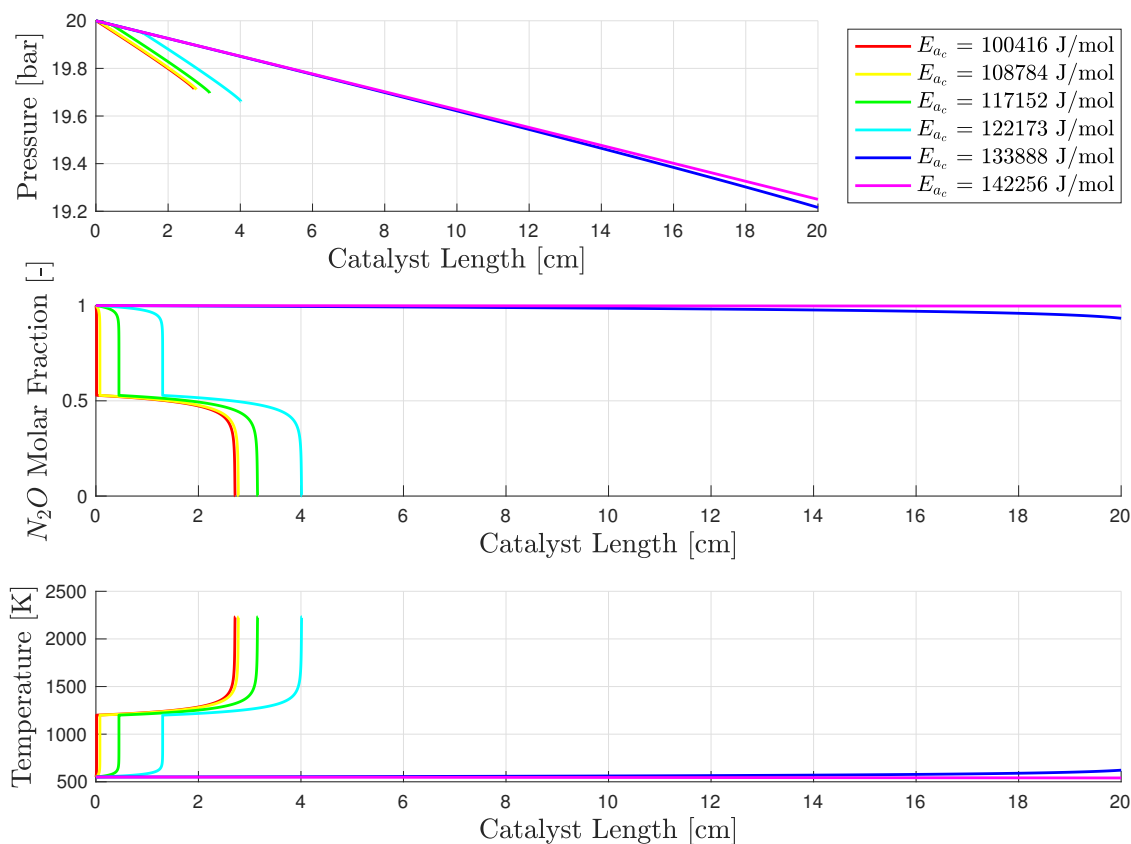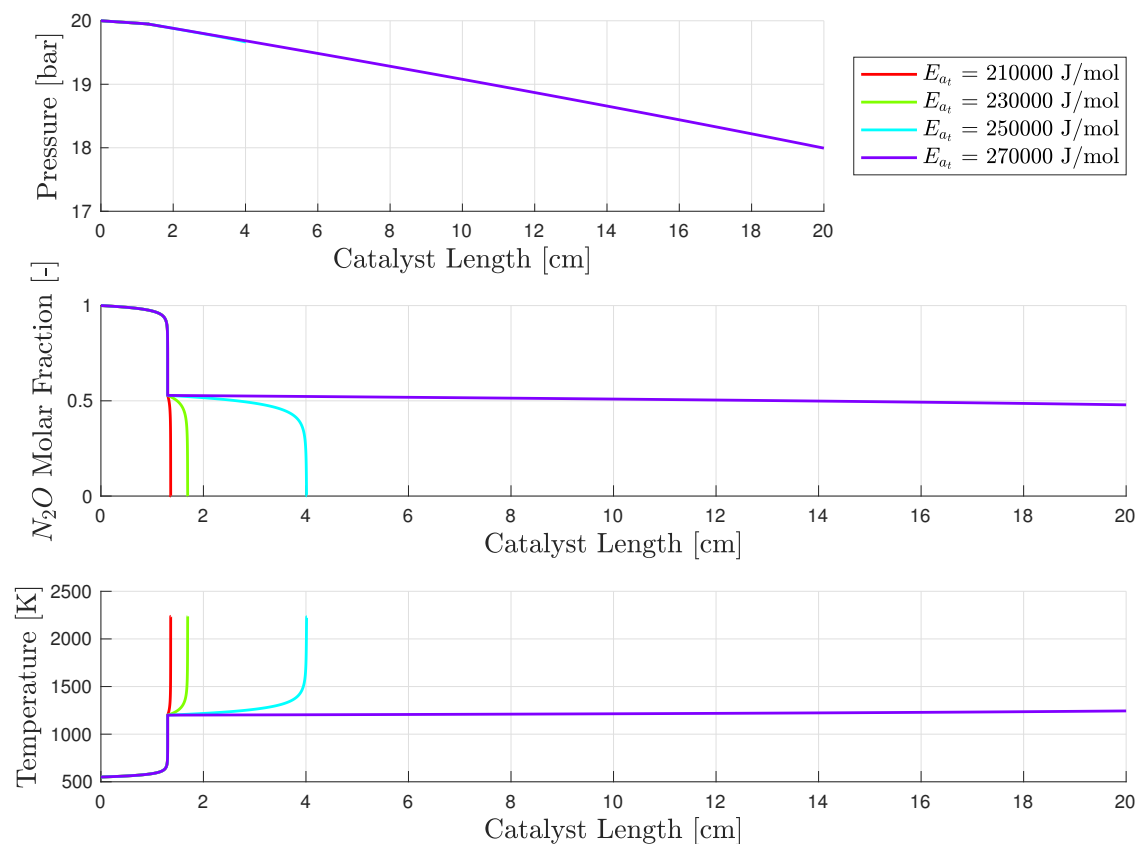
Figure 4.18: E_{a_c} Parameterization

4.4   Different Solvers

In the end a pure numerical analysis has been finally performed with the intention to test three different ODE solvers defining their impact on the results. Performances in terms of time and precision are reported and motivates the selection of the algorithm exploited for the solution of the plug flow reactor ODEs problem. The solver selected are: ODE23s, ODE45 and ODE113.

Figure 4.23 shows simulation results: precision of the integrating algorithms employed can be observer, together with Table 4.4, and helps in understanding performances of the solvers.

If on one hand precision of all algorithms is the almost the same with the decrease of tolerances, on the other integration time shows that, being a stiff integration scheme, ODE 23s is very slow in computing the solution with low tolerances imposed.

Figure 4.19: E_{a_t} Parameterization

Throughout the work, a tolerance of 10^{-8} has been set for the integration of the plug flow reactor equations, and with such tolerance ODE 23s integrates in 13.2 s. No important differences, as clear from Table 4.4, is present between ODE 45 and ODE 113.

Another important point to focus on is that decomposition trend, position and temperature of final decomposition are all results that are independent from the particular integration scheme adopted.

4.5 Overall Simulation

All the components, described and analyzed in the previous sections, are now assembled in a unique cluster. The blowdown system is simulated with the integration of
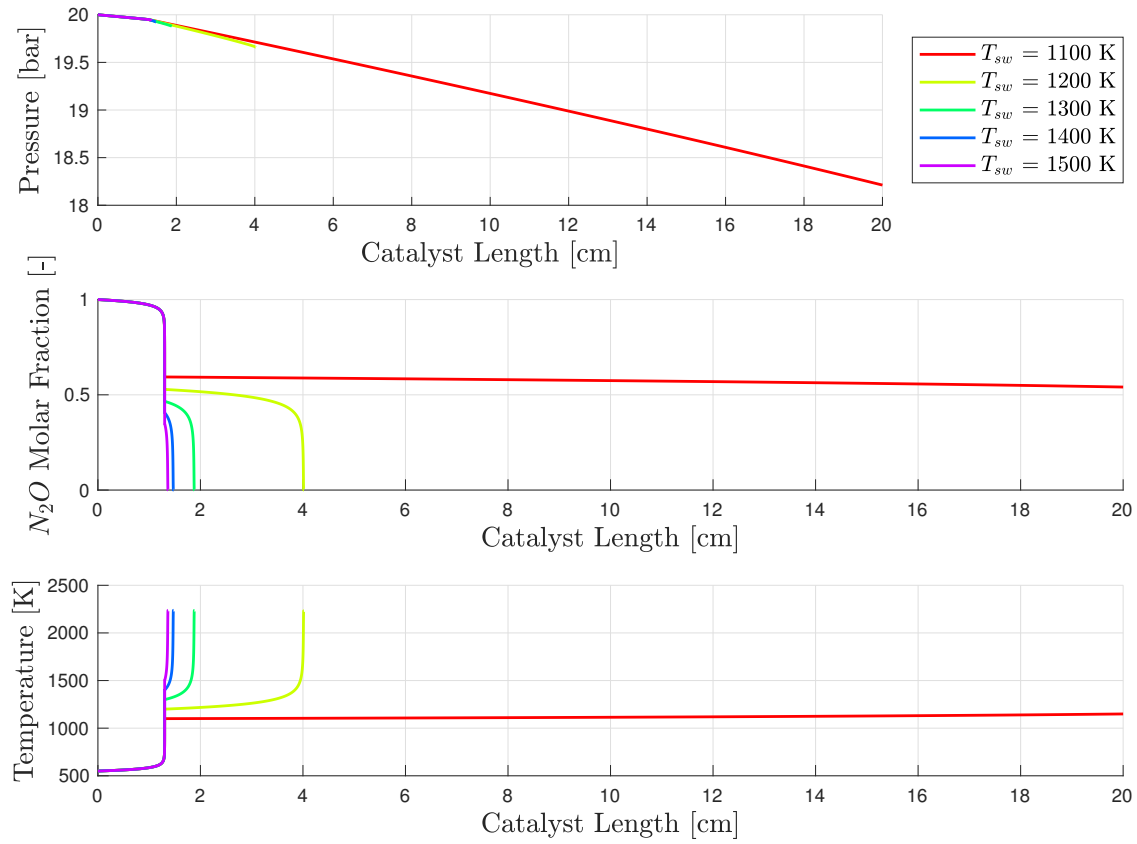
Figure 4.20: Different Switch Temperature

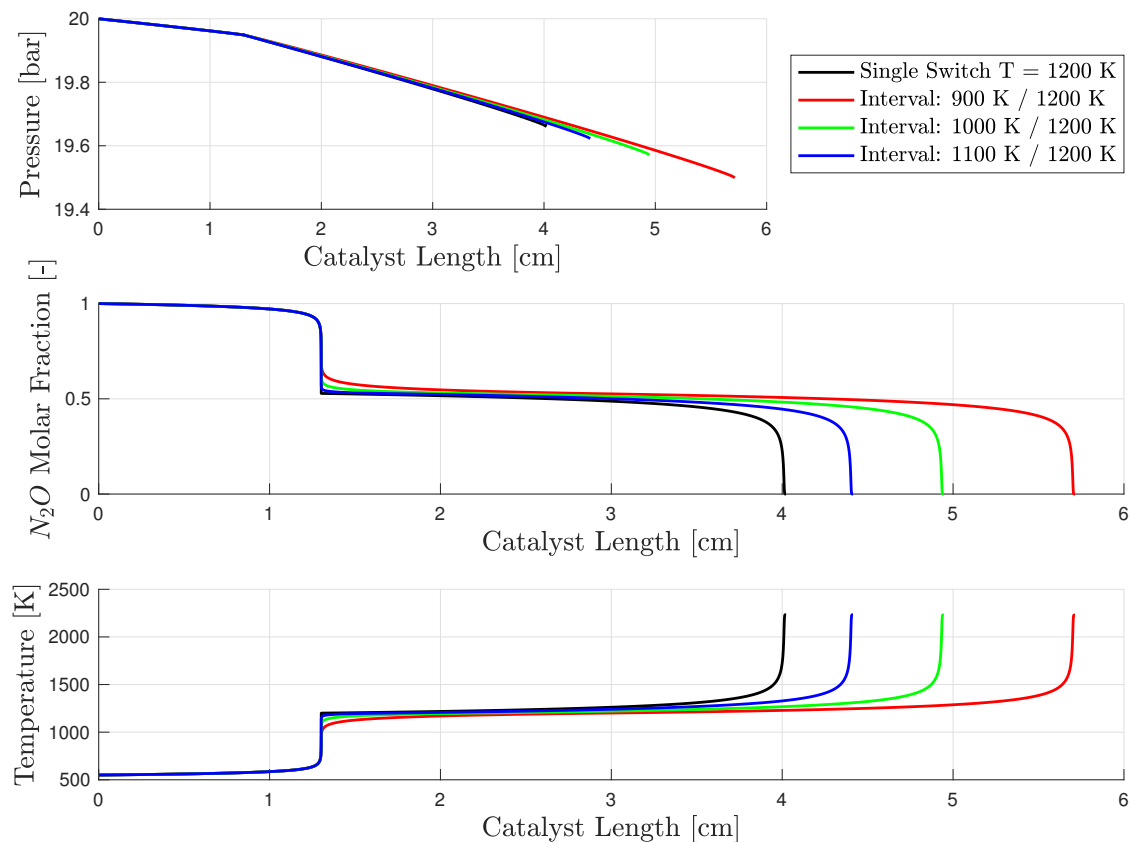| ODE 23s		ODE 45		ODE 113	
Tol	Time [s]	Tol	Time [s]	Tol	Time [s]
10^{-6}	2.9	10^{-6}	1.6	10^{-6}	0.8
10^{-7}	6.4	10^{-7}	1.7	10^{-7}	1.0
10^{-8}	13.0	10^{-8}	2.0	10^{-8}	1.7
10^{-9}	32.4	10^{-9}	2.8	10^{-9}	2.5
10^{-10}	70.5	10^{-10}	4.2	10^{-10}	2.8

Table 4.4: Integration Times

Figure 4.21: Lower Switch Interval

a nozzle.

In order to couple a time-fixed space-varying simulation of the catalyst time-varying simulation for the tank outflow dynamics, catalyst simulation will be performed at precise moment in time, in order to simulate assembly behavior in the nominal or design condition ($t = 0$ s) and different off-nominal situations. In Figures 4.24 and 4.25 it is possible to detect the selected time instant at which simulation of the catalyst is run, with respectively initial pressure and mass flow rate.

Figures 4.26 and 4.27 present respectively pressure loss and temperature profile inside the catalyst in the four time instant selected.

Looking at Table 4.5, a wrap-up of the results, and at all the Figures presented, some important considerations can be drawn:

- Final decomposition temperature reaches in time almost the same value, in accordance to what already stated in the parametric study of the catalyst.
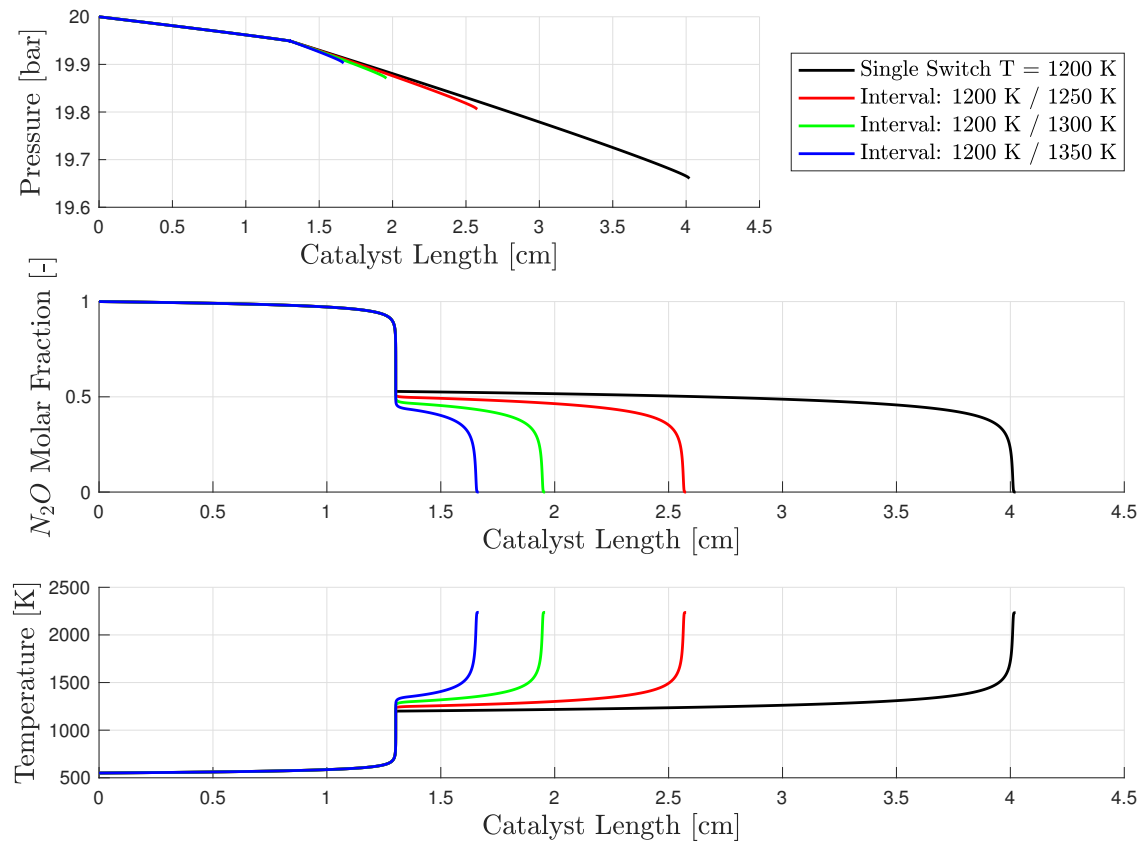
Figure 4.22: Higher Switch interval

Length of complete decomposition is slight shorter than the usual one presented in the catalyst standard simulation case since input mass flow rate is slightly smaller than 25 g/s (22.4 g/s).

– An interesting feature recognized from the different catalyst simulations is that, despite input conditions are variable (e.g. mass flow rate and pressure), they are counter-balancing each other in order to keep decomposition profile almost uniform in time.

Reaction slows down slightly with the emptying of the tank, as shown in the results of Table 4.5.

From the view point of geometric design of the catalyst, a length of 4.5 cm for the catalytic bed perfectly suits at any time the trend of the decomposition reaction: a completely non-reactive mixture ($N_2 + \frac{1}{2}O_2$) travels the packed bed
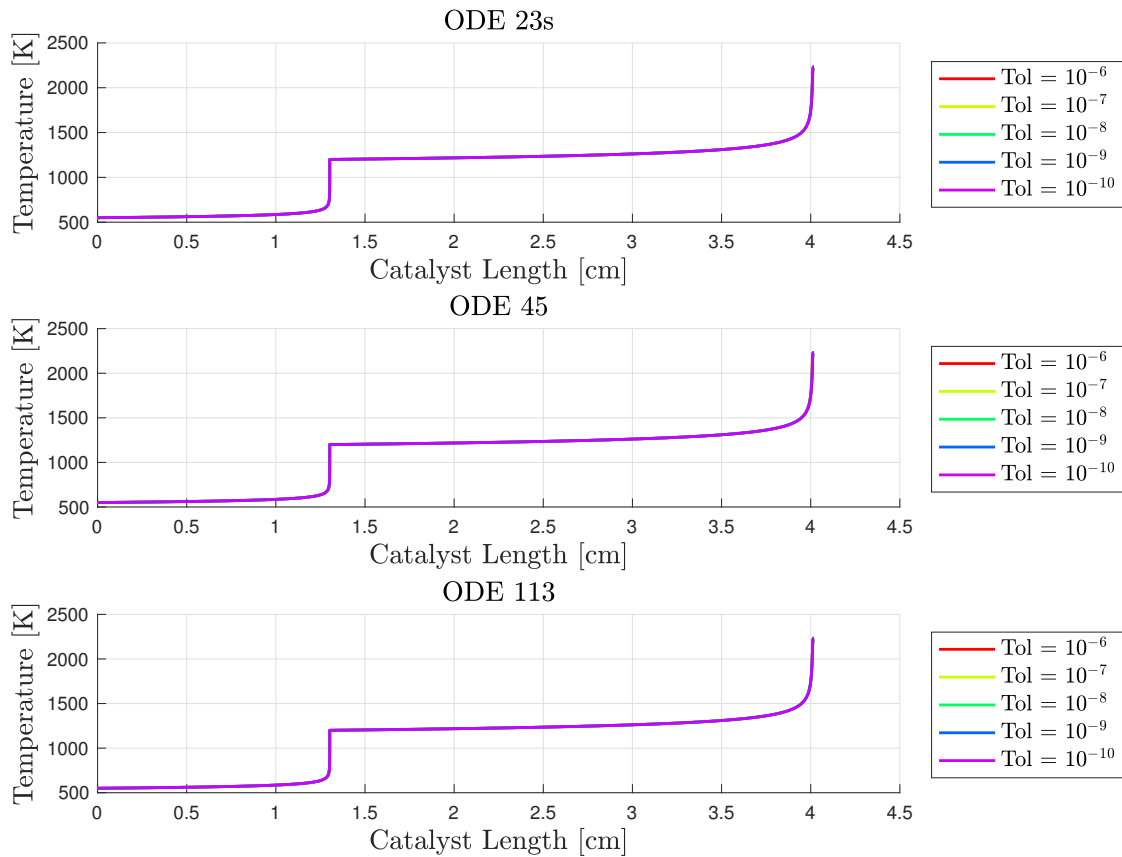
Figure 4.23: Different Solvers

reactor only for a short length-span, with negligible pressure loss.

– Pressure losses shrinks in time since input pressure is decreasing together with mass flow rate.

– A nozzle is used to evaluate the propulsive performances of the assembly, as presented in Section 3.3.4. Selecting an adapted nozzle in the design condition, therefore expanding in optimality just at the beginning of the simulation, predicted specific impulse for the assembly is about 171.7 s with a developed thrust of 37.7 N, in accordance with theoretical results obtained in Chapter 1 and the literature reviews presented in the same Chapter.

Time t [s]	0.0	3.7	7.5	14.9
Tank Pressure p_{tank} [bar]	30.0	24.6	20.1	13.6
Exit Tank Pressure p_{exit} [bar]	23.8	19.0	15.1	9.8
Catalyst Inlet Pressure p_0 [bar]	23.2	18.4	14.6	9.5
Final Decomposition Temperature T_{end} [K]	2231.3	2234.1	2235.6	2235.5
Mass Flow Rate $\dot{m}$ [g/s]	22.4	17.8	14.2	9.2
Complete Decomposition [cm]	3.07	3.08	3.11	3.19
Thrust [N]	37.7	29.3	22.7	13.8
Specific Impulse [s]	171.7	167.4	162.6	152.1

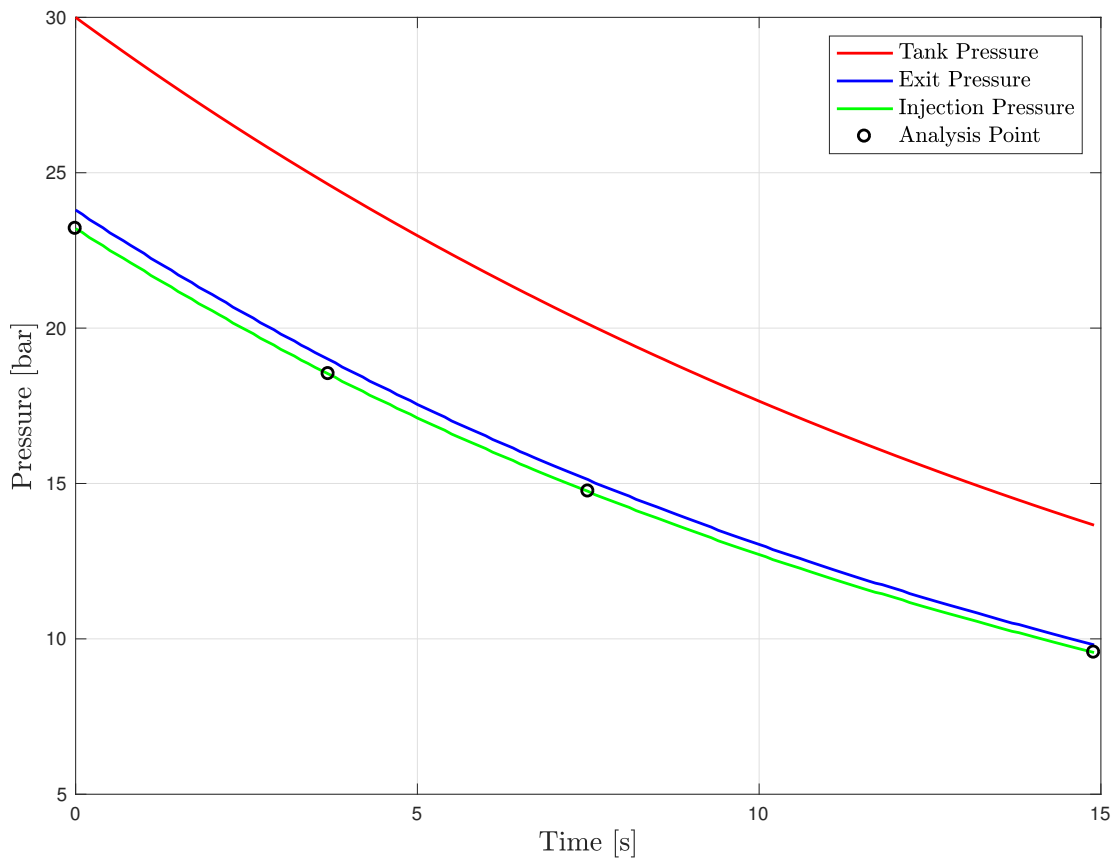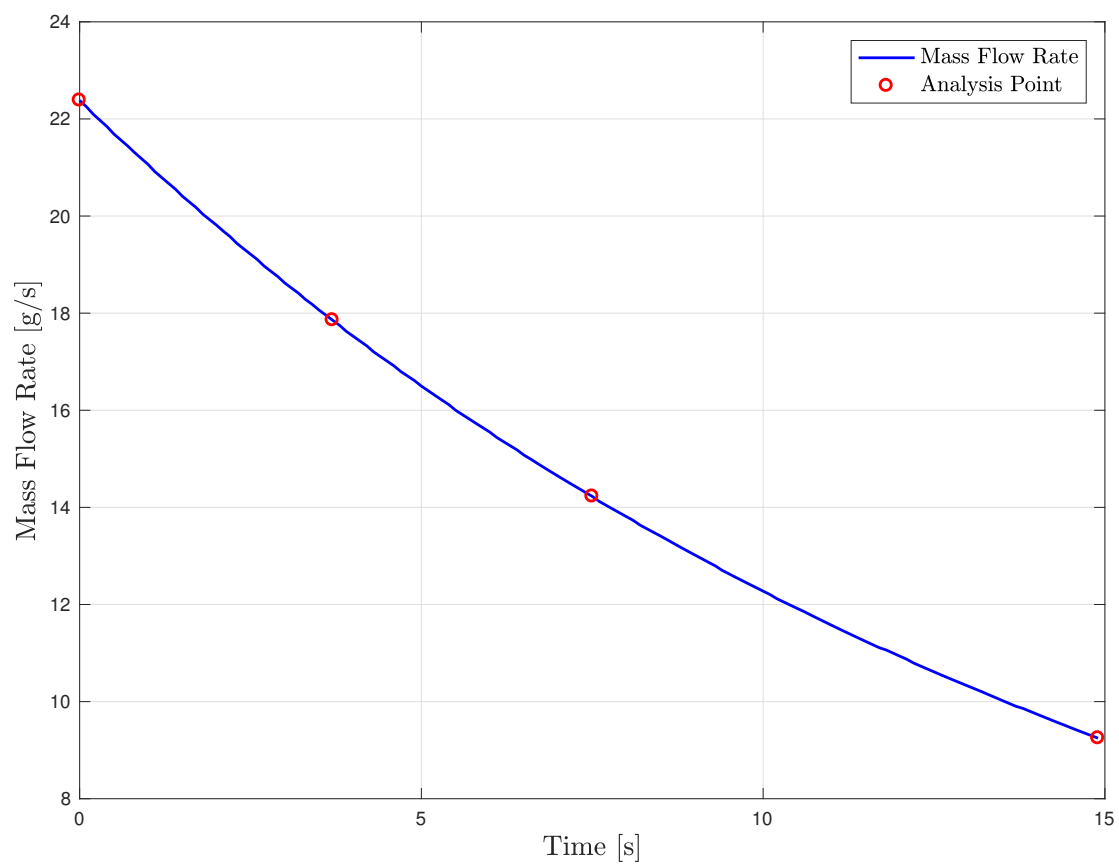Table 4.5: Overall Simulation Results

Figure 4.24: Outflow Pressure

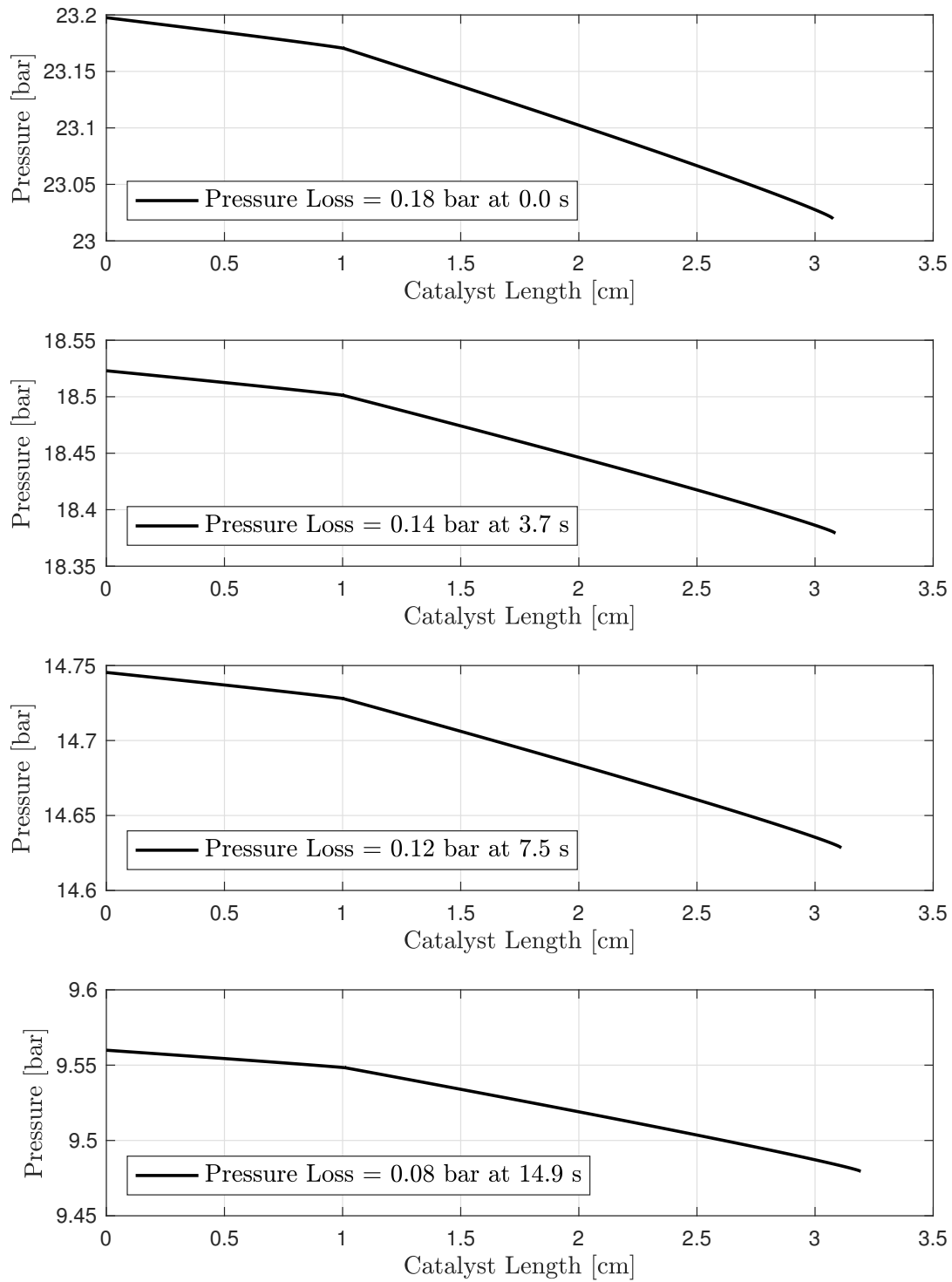Figure 4.25: Outflow Mass Flow Rate
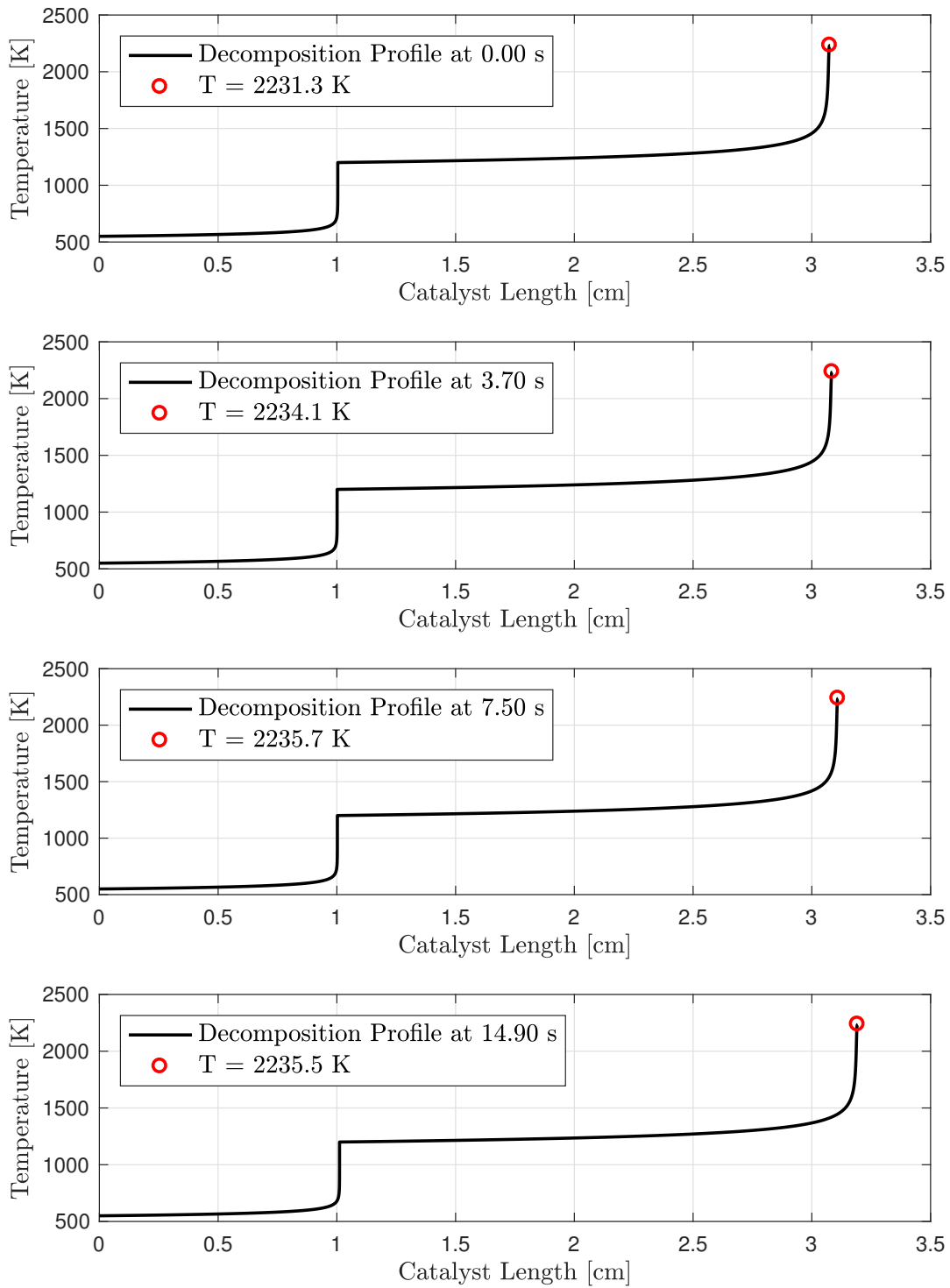
Figure 4.26: Catalyst Pressure Loss in Time

Figure 4.27: Catalyst Temperature Evolution in Time

Chapter 5

Discussion of Meaningful Results

The following Chapter focuses on some important aspects arisen from the results presented in Chapter 4.
All important aspects are analyzed separately and literature, quoted in Chapter 1, 2 is recalled and used to evaluate results.

5.1   Final Decomposition Temperature

Estimation of the final decomposition temperature is one of the fundamental information available to assess goodness of the simulation.
Final decomposition temperature has been computed with a variety of tools (CEA code, theoretical computation, catalyst simulator): taking the CEA code as a reference, error in the estimation of the decomposition temperature arises due to incorrect estimation of the c_p values for the three species involved in the analysis, and in particular due to lack of reliable data at high temperature for N_2O specific heat as reported and motivated in Chapter 2 and 4.

From the quoted experimental works concerning N_2O decomposition, Lohner et al. [62] analyze the effectiveness of several catalysts, reaching a maximum temperature of 1225 °C. As the authors explain, the catalyst is design to be radiation-cooled to prevent yielding of the case (which is not internally insulated): this turns out to reduced the final decomposition temperature. Differently from their work, the scope of the presented design is to insulate the internal surface of the case, with a YSZ layer commonly used in aerospace industry [60], to prevent both heat loss (and temperature reduction, with the consequence of higher performances, as suggested by

Karabeyoglu et al. in [25]) and external case yielding.

Importance of case insulation is also remarked by Zakirov in [21] in order to maximize propulsive performances and protect catalyst case.

5.2 Switch between Catalytic and Thermal Decomposition

This an important point of the work. Simulating numerical the switching from catalytic to thermal decomposition is actually impossible: experimental activity is strictly required to understand this type of phenomenon.

From similar works concerning decomposition of N_2H_4 [8] and H_2O_2 [20], this problem is not a point of concern: reaction rates for catalytic and thermal decompositions invert their leading role with increasing temperature.

This is due to the fact that thermal decomposition has low activation energy for both compounds (152.4 kJ/mol for N_2H_4 [8] and 200 kJ/mol for H_2O_2 [20]) meaning that at a certain temperature thermal decomposition becomes predominant with respect to the catalytic one.

The higher activation energy for N_2O thermal decomposition (250 kJ/mol, connected with its larger decomposition temperature with respect to H_2O_2 and N_2H_4) translates in a lower reaction rate with respect to the catalytic one: as a result thermal decomposition is never faster than catalytic one.

To simulate the phase change of the hexa-aluminate support and sequential active phase sublimation an abrupt shift is introduced in the code.

Lack of available experimental data has shifted the attention on how different models of this phenomenon alters the results.

Despite the obvious consequence of an increase in switch temperature (faster thermal decomposition and shorter catalyst), there is no significant variation in decomposition temperature, meaning that the phenomenon described in this Section 4.3 does not alter the performance of the catalyst.

5.3 Trends for Mixture Properties in the Catalyst

Makled and Belal exploit, in [8], a plug flow reactor model to simulate N_2H_4 decomposition with good agreement with experimental data. A plug flow reactor model is

therefore a suitable choice to model decomposition inside a catalyst.
Besides the decomposition temperature discussed above, several other quantities can be observed to assess goodness of the results through a comparison with literature.

First of all, for the boundary condition selected, catalyst length obtained are absolutely comparable with the ones reported by Lohner et al. in [62]. The parametric analysis with respect to increasing input mass flow rate reveals a phenomenon known as **quencing**, reported in [62], and common to all catalytic decomposition (evidence are reported by Koopmans also for H_2O_2, in [20]): the simulator correctly predicts a shifting of the decomposition front towards the end of the catalyst case, as shown in Chapter 4.

Wood et al. report in [44] a decomposition profile in terms of molar flow rate very similar to the one obtained for the predicted decompositions of this work. Finally, a parametric analysis with respect to increasing inlet temperature is reported by Karabeyoglu et al. in [25] showing a very similar trend to the one obtained in Section 4.2.1 when dealing with similar parametric studies.

5.4 Simulation Time and Performances

Generally, all experiments involving decomposition inside a catalyst of a certain mixture last for hours, in order to assess durability in time of the decomposition. Repeatability is also tested in the same environment. [31] [62] [20]
What is presented in the framework of this thesis consists in a steady-state simulation of the decomposition inside the catalyst during the tank discharge. Length of the phenomenon is therefore considerably shorter (around 30 seconds).
The coupling of the catalyst with a tank does not preclude in any way the applicability of the aforementioned catalyst simulator to long-lasting experiments. In the framework of a pure numerical simulation, a tank allows to simulate a time varying flow injected in the catalyst so as to simulate a pattern of different initial conditions.

Lastly, propulsive performance evaluated during the Overall Simulation in Section 4.5 are pretty close to the theoretical computations, reported in Chapter 1, with theoretical evidence also in [31] [21].
With respect to the only system that actually has flown, the Mark-III resistojet in 1998, estimations gives a more efficient decomposition event for N_2O: I_{sp} has increased from 148 s (Mark-III) to 171 s (this thesis).

Chapter 6

Conclusions

A model for N_2O decomposition inside a catalyst has been defined and numerically tested in the presented thesis. The numerical steady-state simulator has been tested in a wide variety of different boundary conditions and parametric study have been also performed in order to assess model sensibility to design parameters.

The outcome of the simulations have been critically analyzed to validate the code with the help of theoretical notions, simulation codes (NASA CEA) and literature survey.

In a numerical environment, the code has been coupled with a tank outflow simulator and a converging-diverging nozzle.

Respectively, the coupling with the tank helps in assess variability of catalyst working condition during the discharge, with a different pattern of inlet N_2O properties. a converging-diverging nozzle expansion of the decomposed mixture helps in evaluating propulsive parameters of the overall assembly, which results to be quite adherent to theoretical evaluations.

The proposed N_2O seems to give better decomposition than the one obtained with the Mark-III resistojet in 1998.

Simulation of the overall coupled system gives also a first sizing of the overall apparatus needed to test N_2O decomposition. Tank geometry has been selected and sized according to mechanical stresses expected. Catalyst case material has been chosen and the geometry sized according to the mechanical performance requested.

A possible solution to the high decomposition temperature problem is proposed: an insulation material (YSZ) has been selected. Its deposition technique chosen and the amount of material to be deposited on the internal surface of the catalyst case has been selected.

The catalyst simulator gives results in good agreement with the ones found in the proposed literature. A small error (5%) in estimating the final decomposition temperature with respect to the correct value, computed with the CEA code, is committed due to an erroneous extrapolation of thermodynamic properties.

NIST database gives a large spectrum of properties up to a given temperature (limited by dissociation of the compound). Ideal gas assumptions is used at higher temperatures.

It has been found out that these errors are ascribable to the Shomate prediction at high temperature. These predictions are the foundation exploited to built a database of thermodynamic quantities: compared to this, extrapolation errors are actually a small percentage of the global estimation error. The recognized trend for the error is: the larger is the initial temperature of N_2O, the bigger is the error. For $550\,K$, estimation errors are below 5%.

The shift between catalytic to thermal decomposition is modeled as an abrupt phenomenon: catalyst losses suudenly all its effectiveness.

Further analysis has tested a progressive model of this shift: catalyst gradually loses its effectivness.

In both situations, simulation of the decomposition dynamics is not upset.

Points of Concern & Future Works

Some open points are left open by this thesis and shall be investigated in the future.

Numerical simulation of shift from catalytic to thermal decomposition is not possible for N_2O. Experiments have to be carried out in order to assess at which temperature hexa-aluminate catalyst starts to lose its effectiveness. What is proposed in the thesis is an abrupt shift in decomposition (at a certain temperature the catalyst loses complete its effectivenes) with parametric study with the only goal of defining the impact of this phenomenon.

The plug flow model of the catalyst does not leave room to the evaluation of convective heat exchange between mixture and pellets. Further investigation are required to assess how large is this heat exchange and its effect on the overall decomposition. In particular, this thesis accounts only for kinetic limitation for the decomposition (low initial temperature). Particular geometry or material of the catalytic pellets can lead to diffusion or convection limitation of the reaction. Evidence of these phe-

nomena are reported in Section 2.2.2.

In conclusion, a simulation of the pre-heating mechanism after injection of N_2O into the catalyst has not been considered by the thesis. The state-of-the-art technology for pre-heating devices, a known technology for catalyst, allows a high fidelity simulation to be run without such a component.

If a constant heat input is given to the nitrous oxide injected into the catalyst, as soon as the tank empties (and tank exit temperature decrease), the initial decomposition temperature lowers.

It is therefore important to tune correctly the amount of heat provided by the pre-heater: in such a way decomposition can be therefore completed.

Acknowledgements

I would like to thank Technische Universität München, the Lehrstuhl für Turbo-maschinen und Flugantriebe and Prof. Dr.-Ing. Oskar J. Haidn. for the possibility gave me in developing this work during my six months in Munich; in particular my advisor Ph.D. student Chiara Boffa for the precise, professional and competent help given during the evolution of the work; in particular my advisor at Politecnico di Milano prof. Filippo Maggi for his precious and determinant contribution to the presentation of my work.

I would like to express all my love to the boys and girls of "La P.M.", my dear-est friends, with who I lived and I'm still living incredible and priceless moments; all my colleagues and friends met during the B.Sc. and M.Sc. at PoliMi; my friends in Munich companions for the best life experience of my life; my newest friends from team ECLIPSIS for the stressful and ultimately funny work done for the project. Thank you all.
Ultimately, I thanks my sister and the two persons the thesis is dedicated to, without you nothing of this would have been possible. My struggle has been so far even your struggle, I know, and for any congratulation I receive for my achievements you must know that you are a huge part of it.

Vorrei esprimere tutto il mio amore e il mio affetto per le ragazze e i ragazzi della "P.M.", i miei amici più cari, con cui ho vissuto e continuo a vivere momenti incred-ibili ed inestimabili; per i miei colleghi di studi nella Laurea Triennale e Magistrale al Polimi; i miei amici di Monaco di Baviera compagni nella migliore esperienza della mia vita; i miei nuovi amici del team ECLIPSIS per lo stressante, ma alla fine divertente, lavoro svolto per il progetto (anzi il PROGETTO cit.). Grazie a tutti voi. Infine vorrei ringraziare la mia sorellina e le due persone a cui il lavoro é dedicato, senza di voi nulla di tutto ció sarebbe stato possibile. La mia fatica, di cui siete stati i più vicini testimoni, é stata anche la vostra fatica, lo so, e per ogni congratulazione che ricevo per i miei risultati, sappiate che ne siete una parte enorme.

A Loca piace correre tra i prati...

Bibliography

[1] G. P. Sutton and O. Biblarz. *Rocket Propulsion Elements*. John Wiley and Sons Inc., 7th edition, 2001.

[2] *Airbus Thruster Class*. http://www.space-propulsion.com/spacecraft-propulsion/hydrazine-thrusters/index.html. Last visited: December 2016

[3] *Moog-ISP thrusters*. http://www.moog.com/literature/Space_Defense/Spacecraft/Propulsion/Monopropellant_Thrusters_Rev_0613.pdf. Last visited: December 2016

[4] *AeroJet RocketDyne thrusters*. https://www.rocket.com/propulsion-systems/monopropellant-rockets. Last visited: December 2016

[5] *Northrop Grumman Thrusters*. http://www.northropgrumman.com/Capabilities/PropulsionProductsandServices/Pages/MonopropellantThrusters.aspx. Last visited: December 2016

[6] T.W. Price and D. D. Evans. The status of monopropellant hydrazine technology. Technical Report 32-1227, Jet Propulsion Laboratory, California Institute of Technology, Pasadena, California, Febraury 1968.

[7] A. F. Grant Jr. Basic factors involved in the design and operation of catalystic monopropellant-hydrazine reaction chambers. Technical Report 20-77, Jet Propulsion Laboratory, Pasadena, California, March 1953.

[8] A. E. Makled and H. Belal. Modeling of hydrazine decomposition for monopropellant thrusters. In *13th International Conference on Aerospace Sciences and Aviation Technology*, number ASAT-13-PP-22, pages 1–17, Cairo, Egypt, May 2009.

[9] S. G. Pakdehi, M. Salimi, and M. Rasoolzadeh. A review on decomposition of hydrazine and its kinetics as a novel approach for CO-Free H2 production. *Researches and Applications in Mechanical Engineerin*, 3:21–22, 2014.

[10] MIT OpenCourseWare. Space propulsion, session 12: Monopropellant thruster. https://ocw.mit.edu/courses/aeronautics-and-astronautics/16-522-space-propulsion-spring-2015/lecture-notes/MIT16_522S15_Lecture12.pdf, 2016.

[11] M. J. Russi. A survey of monopropellant hydrazine thruster technology. In *9th AIAA/SAE Propulsion Conference*, number AIAA-73-1263, pages 1–2, Las Vegas, NV, USA, November 1973.

[12] E. J. Wucherer, T. Cook, M. Stiefel, R. Humphries, and J. Parker. Hydrazine catalyst production - sustaining s-405 technology. Technical Report 2003-5079, AIAA.

[13] E. J. Wernimont. System trade parameter comparison of monopropellants: Hydrogen peroxide vs hydrazine and others. In *42nd AIAA/ASME/SAE/ASEE Joint Propulsion Conference and Exhibit*, number AIAA-2006-5235, pages 3–4, Sacramento, CA, USA, July 2006.

[14] W. M. Marshall and M. C. Deans. Recommended figures of merits for green monopropellants. Technical Report 2013-216560, National Aeronautics and Space Administration Glenn Research Center, Cleveland, OH, USA, 2013.

[15] *Defense Logistic Agency Standard Price*. http://www.dla.mil/Energy/Business-/StandardPrices.aspx. Last visited: December 2016

[16] A. Cervone, L. Torre, L. d'Agostino, A. J. Musker, G. T. Roberts, C. Bramanti, and G. Saccoccia. Development of hydrogen peroxide monopropellant rockets. Technical Report 2006-5239, ALTA S.p.A and DELTACAT Ltd. and ESA-ESTEC, July 2006.

[17] J. C. Whitehead. Hydrogen peroxide propulsion for smaller satellites. In *12th AIAA/USU Conference on Small Satellite*, number SSC98-VIII-1, page 6, Logan, UT, USA, August 1998.

[18] E. J. Wernimont and P. Mullens. Recent developments in hydrogen peroxide monopropellant rockets. Technical Report 99-2741, General Kinetics, LLC, Aliso Viejo, CA, USA, June 1999.

[19] Anon. *Occupational health guidelines for hydrogen peroxide.* U.S. Department of Health and Human Service, September 1978.

[20] R. J. Koopmans. Modeling of multiphase multicomponent chemically reacting flows through packed beds. Master's thesis, University of Southampton, 2013.

[21] V. Zakirov, M. Sweeting, V. Goeman, and T. Lawrence. Surrey research on nitrous oxide catalytic decomposition for space applications. In *14th AIAA/USU Conference on Small Satellite*, number SSC00-XI-1, Logan, UT, USA, September 2000.

[22] Y. Scherson, K. Lohner, B. Lariviere, B. Cantwell, and T. W. Kenny. A monopropellant gas generator based on N2O decomposition for "green" propulsion and power applications. In *45th AIAA/ASME/SAE/ASEE Joint Propulsion Conference and Exhibit*, number AIAA-2009-4875, pages 1–9, Denver, CO, USA, August 2009.

[23] G. Cai, S. Wei, J. Fang, M. Li, Y. Cong, and Z. Yang. Design and performance characterization of a sub-newton N2O monopropellant thruster. *Aerospace Science and Technology*, 23(1):439–451, December 2012.

[24] F. Kapteijn, G. Marbàn, J. Rodriguez-Mirasol, and J. A. Moulijn. Kinetic analysis of the decomposition of nitrous oxide over ZSM-5 catalysts. *Journal of Catalysis*, (CA 971581):256–257, December 1996.

[25] A. Karabeyoglu, J. Dyer, J. Stevens, and B. J. Cantwell. Modeling of N2O decomposition event. In *44th AIAA/ASME/SAE/ASEE Joint Propulsion Conference and Exhibit*, number AIAA-2008-4933, pages 9–14, Hartford, CT, USA, July 2008.

[26] *EPA: Green House Gas Emission - Nitrous Oxide Emission.* https://www.epa.gov/ghgemissions/overview-greenhouse-gases-nitrous-oxide. Last visited: December 2016

[27] *Nitrous Oxide Emission.* https://data.worldbank.org/indicator/EN.ATM.NOX-E.KT.CE?view=chart. Last visited: December 2016

[28] M. Persson, K. Anflo, A. Dinardi, and J. M. Bahu. A family of thruster for ADN-based monopropellant LMP-103s. In *48th AIAA/ASME/SAE/ASEE Joint Propulsion Conference and Exhibit*, number AIAA-2012-3815, Atlanta, GA, USA, July - August 2012.

[29] K. Anflo and B. Crowe. In-space demonstration of high performance green propulsion and its impact on small satellites in-space demonstration of high performance green propulsion and its impact on small satellites. In *25th Annual AIAA/USU Conference on Small Satellites*, number SSC11-IX-2, Logan, UT, USA, August 2011.

[30] L. J. Wiley and J. R. Werts. *Space Mission Analysis and Design.* Space Technology Library, 3rd edition, 1999.

[31] V. A. Zakirov. *Investigation into Nitrous Oxide Propulsion Option for Small Satellite Applications.* PhD thesis, Centre for Satellite Engineering Research, University of Surrey, August 2001.

[32] C. Merrill. Nitrous oxide explosive hazards. Technical Report 2008-184, Air Force Research Laboratory, 2008.

[33] R. Newlands. Modelling the nitrous run tank emptying. Technical Report 002, Aspire Space, 2011.

[34] L. D. Schmidt. *The Engineering of Chemical Reactions.* New York: Oxford University, 1998.

[35] S. S. Zumdahl and S. A. Zumdahl. *Chemistry.* Houghton Mifflin Company, seventh edition, 2007.

[36] M. E. Davis and R. J. Davis. *Fundamentals of Chemical Reaction Engineering.* McGraw-Hill, 2003.

[37] L. Hennemann, J. C. de Andrade, and F. de Souza Costa. Experimental investigation of a monopropellant thruster using nitrous oxide. *J. Aerosp. Technol. Manag.*, 6(4):363–372, October 2014.

[38] W. M. Kalback. *The Thermal Decomposition of Nitrous Oxide on Gold at Elevated Pressure.* PhD thesis, The University of Oklahoma Graduate School, Norman, Oklahoma, 1973.

[39] L. Jones and P. Atkins. *Chemistry: Moleculs, Matter and Change.* J. Chem. Educ., 4th edition, 2001.

[40] D. L. Baulch, C. T. Bowman, C. J. Cobos, R. A. Cox, Th. Just, J. A. Kerr, M. J. Pilling, D. Stocker, J. Troe, W. Tsang, R. W. Walker, and J. Warnatz.

Evaluated kinetic data for combustion modeling: Supplement II. *The Journal of Physical Chemistry*, 34(3):1143–1144, 2005.

[41] F. Kapteijn, J. Rodriguez-Mirasol, and J. A. Moulijn. Heterogeneous catalytic decomposition of nitrous oxide. *Applied Catalysis B: Environmental*, (9):29–40, 1996.

[42] F. Pinna, M. Scarpa, G. Strukul, E. Guglielminotti, F. Boccuzzi, and M. Manzoli. Ru/ZrO2 catalysts. *Journal of Catalysis*, (192):158–162, 2000.

[43] *Encyclopedia of Science and Technology*. McGraw-Hill, 2008.

[44] B. R. Wood, J. A. Reimer, M. T. Janicke, and K. C. Ott. Nitrous oxide decomposition and surface oxygen formation on Fe-ZSM-5. *Journal of Catalysis*, (224):148–155, 2004.

[45] D. T. Wickham, B. D. Hitch, and B. W. Logsdon. Development and testing of a high temperature N2O decomposition catalyst. In *46th AIAA/ASME/SAE/ASEE Joint Propulsion Conference and Exhibit*, number AIAA 2010-7128, Nashville, TN, USA, July 2010.

[46] J. M. Andersson. Controlling the formation and stability of alumina phases controlling the formation and stability of alumina phases. Technical Report 987, Plasma and Coatings Physics Division, Linköping University, Linköping, Sweden, 2005.

[47] Y. S. Toulouklan and C. Y. Ho. *Thermophysical Properties of Matter: The TPRC Data Series; a Comprehensive Compilation of Data*. Purdue University.

[48] F. J. Urige, E. A. Mason, and J. Kestin Thermal conductivity of nine polyatomic gases at low density. Technical report, Brown University, 1990.

[49] Hastelloy X alloy. Haynes, High Temperatue Alloys, 1997. *http://www.haynes.ch/doc/HASTELLOY_X.pdf* Last visited: December 2016

[50] O. Zihao. Deposition of yttria-stabilized zirconia thermal barrier coatings by laser-assisted plasma coating at atmospheric pressure. Master's thesis, University of Illinois, Urbana-Champaign, IL, USA, 2011.

[51] H. Zhao, F. Yu, T. D. Bennett, and H. N. G. Wadley. Morphology and thermal conductivity of yttria-stabilized zirconia coatings. *Acta Materialia Journal*, (54):5195–5207, 2006.

[52] C. Astarita and G. Cardone. *Svuotamento di un serbatoio mediante ugello convergente.* http://wpage.unina.it/astarita/Gasdinamica/2008/slides

[53] Internation Standard. *Measurement of fluid flow by means of pressure differential devices inserted in circular cross-section conduits running full*, ISO 5167-1 edition, 2003.

[54] *Packed Bed Reactor.* http://mdx2.plm.automation.siemens.com/case-studies/packed-bed-reactor.

[55] S. Ergun. Fluid flow through packed columns. *Chemical Engineering Progress*, 48:89–94, 1952.

[56] E. A. Foumeny and F. Benyahia. Predictive characterization of mean voidage in packed beds. *Heat Recovery Systems and CHP*, 11(2/3):127–130, 1991.

[57] C. F. Chu and K. M. Ng. Flow in packed tubes with a small tube to particle diameter ratio. *American Insititude of Chemical Engineers*, 35(1):148–158, 1989.

[58] E. J. Hearn. *Mechanics of Materials 1: An Introduction to the Mechanics of Elastic and Plastic Deformation of Solids and Structural Materials.* Butterworth Heinemann, third edition, 1997.

[59] C. Wan, Y. Motohashi, T. Shibata, and S. Baba. Thermal conductivity of superplastically deformed 3Y-TZP. *Materials Transactions*, 43(10):2473 – 2479, 2002.

[60] CrysTec GmbH, Berlin, Germany. *Y:ZrO2 - YSZ for Research and Development.* http://www.crystec.de/daten/ysz.pdf. Last visited: December 2016

[61] S. K. S. Boetcher. *Natural Convection from Circular Cylinders.* SpringerBriefs in Thermal Engineering and Applied Science, 2014.

[62] K. A. Lohner, Y. D. Scherson, B. W. Lariviere, B. J. Cantwell, and T. W. Kenny. *Nitrous Oxide Monopropellant Gas Generator Development.* https://web.stanford.edu/ cantwell/Recent_publications/Lohner_Scherson_JANNAF_2008.pdf. Last visited: December 2016